Universidade de Lisboa
Faculdade de Ciências
Departamento de Química e Bioquímica

DEVELOPMENT OF NANOMATERIALS FOR CULTURAL HERITAGE CONSERVATION. EVALUATION ON THE DEGRADATION STATE OF ANTIQUE COINS BY SPECTROSCOPIC TECHNIQUES

Maria Inês Baião Ramos de Oliveira

Dissertação
Mestrado em Química
Especialização em Química-Analítica

2014

Universidade de Lisboa
Faculdade de Ciências
Departamento de Química e Bioquímica

DEVELOPMENT OF NANOMATERIALS FOR CULTURAL HERITAGE CONSERVATION. EVALUATION ON THE DEGRADATION STATE OF ANTIQUE COINS BY SPECTROSCOPIC TECHNIQUES

Maria Inês Baião Ramos de Oliveira

Dissertação
Mestrado em Química
Especialização em Química-Analítica

Tese orientada por:
Professora Doutora Maria da Estrela Borges de Melo Jorge
Professora Doutora Maria Luisa de Carvalho Dias de Sousa Leonardo

2014

ACKNOWLEDGMENTS

First of all I would like to express my sincere gratitude to my supervisors Professors Maria Estrela Jorge (*Centro de Química e Bioquimica, Faculdade de Ciências da Universidade de Lisboa* (CQB-FCUL)) and Maria Luísa Carvalho (*Centro de Física Atómica, Universidade de Lisboa* (UL) and *Faculdade de Ciências e Tecnologias* da *Univerisade Nova de Lisboa* (FCT-UNL)) for the guidance, learning opportunities and the friendship.

To Drs. Sofia Pessanha and Marta Manso thank you so much for your generous help and for providing an amazing working environment.

I would like to thank to Mário Costa for providing the working material and for the numismatic support.

I also offer my appreciation to my Italian supervisors Professors Piero Baglioni and Rodorico Giorgi for the opportunity of working in the *Consorzio Interuniversitario per lo Sviluppo dei Sistemi a Grande Interfase* (*Università degli Studi di Firenze* (CSGI-UniFi)). I would like to thank Professor Giorgi for his, support and understanding.

I also would like to thank to Drs David Chelazzi and to Giovanna Poggi for their time and assistance.

I have learnt a great deal from those whom I had the pleasure of working with either in Portugal or in Italy and, for sure, I will take all off you in my heart and memory. ☺

ABSTRACT

This work is presented in two complementary parts covering the two main fields on the study of cultural heritage.

The first one is focussed on the analysis of a set of six *dinheiros* from the first Portuguese dynasty (13rd and 14th centuries). The coins were analyzed using μ-Energy Dispersive X-ray Fluorescence in order to evaluate their elemental composition, allowing to confirm in four of the coins a billon alloy (copper/silver) and in the remaining two a reduced content of silver. This fact is compatible with the social and economic Portuguese reality during D. Fernando I reign. The coins were further evaluated by means of X-ray Diffraction identifying natives copper and silver, as well as some of their degradation products, such as cuprite, tenorite, malachite, nantokite and atacamite and on the numisms with high silver content, chlorargyrite. By making use of Scanning Electron Microscopy/Energy Dispersive Spectroscopy the morphological analysis on the coins surface was performed evidencing the corroded surface and allowing to identify different morphologies corresponding to copper/copper oxides and silver/silver chloride phases.

On the second part, several calcium carbonate ($CaCO_3$) and calcium hydroxide functionalized nanoparticles were synthesized, purified and physicochemical characterized, in order to study their application by dispersion, on manuscripts and its similar for conservation purposes. The effect of different percentages of the functionalizing agent (dodecanoic acid) was investigated. Results from the visual and turbidimetry analyses showed that the dispersions were not stable for the proposed end. By making use of Attenuated Total Reflectance and X-ray Diffraction was possible to conclude that the acid is present on the final $CaCO_3$ product. Scanning Electron Microscopy allowed to prove the morphological changes on the powders particles and made clear the shortage of nano-objects. The followed route is not effective regarding the synthesis of nanoparticles which may justify the instability of the dispersions.

Key words: corrosion, coins, nanoparticles, XRF, XRD, SEM/EDS, turbidimetry, ATR

RESUMO

Este trabalho é composto por duas partes distintas mas complementares e que diferem apenas na base em estudo. Abrangem-se assim dois dos campos fundamentais no estudo do património cultural, nomeadamente, a avaliação do estado de conservação de um conjunto de moedas antigas, seguido pela proposta de um método para a preservação do papel e seus similares.

A primeira parte da investigação foca-se na análise de um conjunto de seis *dinheiros* datados da primeira dinastia Portuguesa (séculos XIII e XIV), particularmente dos reinados de D. Sancho II (1223-1248); D. Afonso III (1248-1279); D. Dinis (1279-1325); D. Pedro I (1357-1367) e D. Fernando I (1367-1383). Este trabalho baseia-se na avaliação do estado de conservação dos numismas, por meio da identificação e caracterização dos produtos que constituem a sua patina bem como as alterações morfológicas a que a sua superfície esteve sujeita devido à sua interação com o ambiente circundante. Tenta-se ainda propor um mecanismo de corrosão porém devido à falta de informação sobre o local da descoberta, o estado do enterro/desenterro ou mesmo das datas relacionadas com qualquer um destes processos, esta investigação é um desafio tanto a nível do estudo da sua camada de corrosão como a nível do património cultural.

De salientar que os *dinheiros* foram as primeiras moedas portuguesas, cunhadas em liga de bolhão (maioritariamente constituída por cobre, seguido de prata e alguns elementos químicos minoritários). Estas moedas estiveram em circulação, em Portugal, desde meados do século XII até, aproximadamente, 1502. Mais ainda, patina é a camada que reveste a superfície do metal, no seu estado puro ou em liga, sendo constituída por todos os compostos químicos, nomeadamente produtos de corrosão e outros elementos exógenos formados e mantidos na superfície do objeto, alterando a sua cor e textura. Urge considerar o sistema liga/patina/ambiente como um sistema global, em que a patina resulta das interações físico-químicas entre a liga e o ambiente, ao longo do tempo.

A ação combinada de técnicas analíticas não destrutivas como a espectrometria de micro-Fluorescência de raios-X de Energia Dispersiva (μ-EDXRF), a Difração de raios-X (XRD) e a Microscopia Eletrónica de Varrimento acoplada com a técnica de Espectroscopia Dispersiva de raios-X (SEM/EDS) permitem identificar a natureza dos produtos da patina formados no conjunto de moedas estudadas, contribuindo para compreender e preservar a história das sociedades e ajudar à preservação dos mesmos. Do ponto de vista macroscópico e por meio de análise visual pôde concluir-se que, de um modo geral, as superfícies das moedas se encontravam bem definidas e preservadas, dado o seu período de origem. Todas as moedas apresentavam uma coloração preta-acastanhada e, em alguns casos, uma coloração acobreada nas zonas de alto-relevo. Exceção feita à face de uma das moedas que apresentou, pontualmente, sinais típicos de corrosão do tipo "couve-flor". Vários tipos de patinas foram identificados, a saber uma camada amarelo-acastanhado nas áreas de baixo-relevo e, localmente, colorações verde (baixo-relevo) e vermelho-acastanhado (cobrindo a superfície) em todas e/ou alguns dos numismas.

As moedas foram analisadas usando μ-EDXRF de modo a quantificar a sua composição elementar. Com recurso a esta técnica foi possível proceder à confirmação da liga de bolhão em todas as moedas notando-se porém uma redução do teor de prata

nas duas moedas datadas do reinado de D. Fernando I. Este facto é comprovado pela realidade social e económica à época, onde era já conhecida a depreciação do metal. Por meio da técnica de XRD foi possível identificar cobre (Cu), prata (Ag) e chumbo (Pb) nativos bem como alguns dos seus produtos de degradação, nomeadamente cuprite (Cu_2O), tenorite (CuO), malaquite ($Cu_2CO_3(OH)_2$), nantoquite (CuCl) e atacamite ($Cu_2Cl(OH)_3$) e, nos *dinheiros* com teor de prata mais elevado, cloroargirite (AgCl). As moedas foram ainda analisadas com recurso à técnica SEM/EDS tendo sido possível observar a morfologia das suas superfícies. Estas apresentavão sinais característicos de corrosão tendo sido identificadas, maioritariamente, fases ricas em cobre/óxidos de cobre e prata/cloreto de prata.

A interação ente o ambiente e o material metálico tornou-se assim evidente permitindo assinalar a presença de elementos exógenos à liga, tais como silício, cloro, cálcio, fósforo, potássio, e, possivelmente, ferro e mercúrio. Os resultados de μ-EDXRF permitiriam ainda avançar para a possível constituição da liga através da identificação de cobre e prata, bismuto, ouro e, provavelmente, antimónio, chumbo e ferro como parte do minério. A evolução da camada de corrosão pode ser assumida como tendo início aquando da formação da cuprite e, em concordância com a interface metal/meio, a sua consequente conversão noutros compostos químicos. O significativo teor de ião cloreto (Cl^-) registado, quer através das técnicas de análise elementar quer pela identificação dos seus produtos de degradação (CuCl, AgCl e $Cu_2Cl(OH)_3$), pode indicar a exposição a um ambiente marinho (rico em iões Cl^-). Estes resultados são compatíveis com a geografia costeira de Portugal. Mais ainda, os iões Cl^- induzem geralmente um processo de corrosão autocatalítica em artefactos ricos em cobre, o que pode explicar o facto de duas das moedas com teores de Cl^- mais elevados, serem aquelas que apresentam maiores sinais de corrosão. Finalmente é importante notar que outros produtos de patina, como por exemplo compostos amorfos, nomeadamente, outros óxidos, fosfatos ou sulfatos, poderão também estar presentes na superfície das moedas.

A segunda parte do presente trabalho tem como base a síntese, purificação e caracterização físico-química de várias nanopartículas de carbonato de cálcio ($CaCO_3$) e hidróxido de cálcio ($Ca(OH)_2$) funcionalizadas com ácido dodecanoíco (DA), com o objetivo de estudar a sua aplicação, por dispersão, em manuscritos e seus similares com o propósito da sua conservação.

O efeito de diferentes percentagens de agente funcionalizante bem como diversos solventes orgânicos apolares e as condições de realização das dispersões foram estudados; tendo-se concluído que o solvente que apresentou os resultados mais satisfatórios foi o ciclohexano, quando sujeito ao maior número de ciclos ultrassónicos aplicados. Por outro lado os resultados da análise visual e da turbidimetria, técnicas usadas para avaliar a estabilidade das dispersões, mostraram que estas não são estáveis para o fim proposto uma vez que as dispersões obtidas se demonstraram instáveis por um período de tempo estipulado de 18 h a 24 h. Embora o ciclohexano tenha sido o solvente que apresentou os resultados mais promissores outros solvents, além dos estudados, deveriam ser testados. Com base nestes resultados, os estudos seguintes foram realizados apenas para os pós de $CaCO_3$ compostos por percentagens de 0.0% e 5.0% de DA.

Com recurso às técnicas de Refletânica Total Atenuada (ATR) e XRD verificou-se a presença do ácido no produto final de $CaCO_3$ funcionalizado com 5.0% de DA. Mais ainda, por combinação dos resultados de ambas as práticas foi possível identificar calcite e aragonite no produto sem funcionalização (0.0% DA), ao passo que, no produto hidrofóbico (5.0% DA) foram identificadas fases relativas à calcite, vaterite

e aragonite bem como do sal do ácido carboxílico ($Ca(C_{12}H_{23}O_2)_2$). Finalmente, o SEM permitiu observar alterações morfológicas resultantes da introdução do agente funcionalizante bem como provar a não existência de nanopartículas. Em qualquer um dos pós obtidos a carência de nanomateriais tornou-se evidente tendo sido possível identificar aquilo que parecem ser *clusters* de nano-objectos.

A reduzida quantidade de nanopartículas provocou uma redução drástica no número de partículas passíveis de dispersão pois devido ao seu tamanho, estas não têm capacidade de penetrar (tão) profundamente no interior da superfície do papel tornando-se pouco eficazes contra a acidez interna da base. Pode assim concluir-se que a reação, segundo as condições específicas aplicadas, embora eficaz na produção dos pós sintetizados se mostrou pouco eficiente para produzir nanopartículas, justificando assim a instabilidade das dispersões obtidas.

Palavras chave: corrosão, moedas, nanopartículas, XRF, XRD, SEM/EDS, turbidimetria, ATR

INDEX

Evaluation on the degradation state of antique coins by spectroscopic techniques

FIGURE INDEX

TABLE INDEX

ACRONYMS AND ABBREVIATIONS LIST

APT - 5-(3-aminophenyl)-tetrazole

BTAH – Benzotriazole

DA – Dodecanoic acid

DMTD - 2,5-Dimercapto-1,3,4-thiadiazole

EDS – Energy Dispersive Spectroscopy

LOD – Limit of Detection

MMPB - 3-((2-mercaptophenyl)imino)butanoate

RH - Relative Humidity

RSD - Relative Standard Deviation

SEM – Scanning Electron Microscopy

XR – X-ray(s)

XRD – X-ray Diffraction

XRF – X-ray Fluorescence

μ-EDXRF – micro-Energy Dispersive X-ray Fluorescence

XRD Crystal systems abbreviations:

A - aragonite (orthorhombic structure of $CaCO_3$)

AT – atacamite ($Cu_2Cl(OH)_3$)

C – calcite (rhombohedral structure of $CaCO_3$)

CL – calcium laurate ($Ca(C_{12}H_{23}O_2)_2$)

CP – cuprite (Cu_2O)

M – malachite ($Cu_2CO_3(OH)_2$)

N – nantokite (CuCl)

Q – quartz (SiO_2)

SC – chlorargyrite (AgCl)

T – tenorite (CuO)

V - vaterite (hexagonal structure of $CaCO_3$)

1 INTRODUCTION

The thorough knowledge of an archaeological object with its various aspects is a precondition to any applied research. Investigations involving chemical and physical non-destructive instrumental methods contribute greatly to understand and preserve the history of societies.

The present work will be presented in two separate but complementary parts. The first approach (*Evaluation on the degradation state of antique coins by spectroscopic techniques*) is based on the assessment on the conservation state of antique Portuguese coins by identification and understanding of its corrosion products and surface morphologic changes. While the second part (*Development of nanomaterials for Cultural Heritage Conservation*) is result of the synthesis, purification and physical-chemistry characterization of several calcium carbonate ($CaCO_3$) and calcium hydroxide ($Ca(OH)_2$) nanoparticles hydrophobically functionalized with dodecanoic acid (DA), to application on manuscripts for conservation purpose.

In consequence the two main fields on the study of cultural heritage are covered: the investigation on the state of conservation of an object and a proposal to a conservation mode. In this particular case the studied objects are different but the approach is highlighted.

Annexe I presents a list of important definitions and concepts that are going to be use on this work.

1.1 COINS

Coins are particular and important findings during archaeological investigations as source of documentation, understanding and knowledge of people and their societies.

Once these objects play an important role in any national cultural heritage, this study represents a very important step in the first Portuguese dynasty *billon* coins characterization. It is focus on a set of six *dinheiros* dated from the 13rd and 14th centuries, namely from D. Sancho II (1223-1248); D. Afonso III (1248-1279); D. Dinis (1279-1325); D. Pedro I (1357-1367) and D. Fernando I (1367-1383). Due to the limited knowledge, in particular the lack of information about the place of find, state of burial/dig up or even its related dates (the numisms could have been buried, submerged or even exposed to other kind of environments) this investigation is a challenge on both corrosion science and cultural heritage. Is thus

justified the importance of a detailed analysis in order to gain intensive information about chemical composition, nature of the patina and corrosion features on the coins.

1.1.1 Coin history and social impact

The invention of coins resumes to the 650/700 b.C. and since that time they have been used as a medium of exchange. These metal objects are standardized in weight and produced in large quantities at a mint (coinage house).

Numismatics[1] and the study of the coins´ chemical composition (surface and bulk) give important information about the culture, economy and science of a society [1, 2, 3]. For example, the study on the coin depreciation (by reducing the precious metal content) can be correlated to the economic decline as evidence on periods of economic difficulties [4, 5].

Portuguese *dinheiros*

Portugal's independence was proclaimed by D. Afonso Henriques on 25 July 1139, being the first Portuguese coins (*dinheiros*) issued by him. *Dinheiros* (minted in billon alloy) were the currency of Portugal from the late 12nd century until, approximately, 1502.

Various kinds of coins were introduced in the Portuguese culture during the first dynasty. Around 1200, a gold currency was produced and a century later a silver coin was introduced [6].

The set of the studied *dinheiros*, their respective kingdom, date, schematic figures and the mint houses are presented on **Table 1.1**.

Table 1.1 - Set of the studied *dinheiros* and its respective kingdom and date, schematic figures and mint houses [1, 7].

#	King	Date	*Dinheiro*	Legend	Mint
4th	D. Sancho II	1223-1248		SANCIVS REX PORTVGAL	Braga and Lisbon
5th	D. Afonso III	1248-1279		ALFONSVS REX/PORTVGAL	Coimbra and Lisbon
6th	D. Dinis	1279-1325		D.REX PORTVGL/ALGARBII	Lisbon *Casa da Moeda*
8th	D. Pedro I	1357-1367		P.REX PORTVGL/ALGARBII	Lisbon
9th	D. Fernando I	1367-1383		FERNANDVS REX PORTVGALI ET ALGARBI	Portugal and Spain

[1] The definition is presented on **Annexe I**.

D. Sancho II known as the "Cowled One" was born in Coimbra, in 1209, and his death is reported to 1248 in exile (Toledo). He ascended to the throne in 1223 and was deposed by the Holy See due his political and personal ideas, in 1245. Sancho II introduced a great development in minting once the coinage necessity grew due the increasing of the commercial transactions [1].

The "Bolognese" or D. Afonso III became king of Portugal in 1248. He was born in Coimbra (1212) and died in Lisbon (1279). Afonso III extended his domain conquering the southward to Algarve and gave Portugal its definitive boundaries. This king produced several legislation regulating minting alloys, weights and alterations in coins [1].

D. Dinis, the "Husbandman", was born in Lisbon in 1261, ascended to the throne in 1279, and died in Santarém in 1325. During his time, the land was colonized and cultivated; industry grew stronger and the external commerce expanded protected by an organized navy and defended by treaties and protective laws [1]. With D. Dinis the first Portuguese university ("*Estudo Geral"*) was established in Lisbon (1290) being later transferred to Coimbra (1308) [8]. As a consequence, Latin gave way to Portuguese language and started to be used on official documents and diplomas.

D. Pedro I known as the "Just" or the "Cruel" was born in 1320 (Coimbra), died in 1367 (Estremoz) and acceded to the throne by death of his father (D. Afonso IV) in 1357. During his reign the economic situation of the country improved and prospered. Despite its political internal instability, trade was carried on the most important ports of Europe [1].

D. Fernando I known as the "Handsome" (Coimbra, 1345 – Lisbon, 1383) ascended to the throne in 1367 being the last king of the first Portuguese dynasty. Fernando I was involved in unending and unprofitable wars against the Castile which created enormous economic and financial difficulties. In fact, the coinage reflected his irregular and dissolvent administration. He changed and created new types and denominations to mask the weakening and debasement of the alloy (impoverishing in metal) in relation to the inflated nominal values it represented [1].

After the death of D. Fernando I, Portuguese people reacted against his Castilian succession and required the protection of the "Master of the Order of Avis", who acceded to the throne in 1385, founding the second Portuguese dynasty.

1.1.2 Chemical composition of coins

Compositional information constitutes a fundamental tool in the study of antique coins. Studying the elemental composition pattern of the alloy, its fineness and debasement, can

provide valuable information either to provenance studies or for investigations of manufacturing processes, as well as identification of authenticity [4, 5, 9-11].

Billon was one of the most important and common alloys used for minted coins since the ancient Greece. However, only a few studies were made on Portuguese antique coins (Guerra *et al.* [10, 12], Martins *et al.* [13-15] and Mata *et al.* [16, 17]) being the most notorious conclusion that these coins were mostly constituted by copper (approximately 90.0%), silver (around 8.0%) and some minor elements.

(i) Copper

Copper (Cu) occurs naturally as native Cu or alloyed with other elements. In both states it forms a large group of industrially important materials owing to its appealing visual appearance, excellent electrical and thermal conductivities, mechanical workability and resistance [18-20].

Native copper identification with silver and locally arsenic as major impurities is highly desirable in artefacts because it is generally held that the working metals began with the use of pure copper [21]. According to Pernicka [21] the presence of volatile metals such as mercury (Hg) could provide chemical evidence for the presence of native copper; however this element can also be absorbed on copper from groundwater during the burial, inducing inaccurate conclusions.

Historically, the main working processes on this element were the cold working process[2]; annealing[3], smelting[4] and re-melting[5]. It is important to retain that the ores were generally inhomogeneous showing zoning effects, and some elements could be lost during any of these processes. Even more, after the smelting process finding alloying copper with other metals was very common. Numerous copper alloys exist, many with important uses. Apart from billon; brass is a copper-zinc alloy and bronze usually denotes copper-tin alloys yet can refer to any alloy of copper (e.g. aluminium bronze). The metal composition of bronze alloys and its deterioration processes has been examined numerous times [2, 5, 9, 17, 21-30].

(ii) Silver

Silver (Ag) and its alloys have been used in many objects of cultural heritage due to its luxuriousness, luster and intrinsic value. Even more, the surface enrichment of archaeological copper alloys, either intentional or due to corrosion processes, has been known for many years and it is of main interest for a chronological assignment [31, 32].

[2-5] The definitions are presented on **Annexe I**.

The application of a layer of silver onto the surface of a low noble metal (silver surface enrichment) was possible by using chemical, mechanical, thermo-mechanical or physical treatments [5, 33]. All of this processes varied greatly from time to time and place to place. Particularly the presence of areas in the coin with higher content of silver is a normal behaviour in billon alloys due to the low solubility of silver in copper, and vice versa, at room temperature. Based on Martins and Martins [15] the solubility of Cu in Ag is of 8.0% at 780° C, and practically zero at room temperature. During cooling, the system separates each component in the pure state with the same reticular structure as the one in the supersaturated solid solution; so the formation of rich areas of silver dispersed in copper matrix depends on the rate of cooling and thickness of the sample.

Silver was not the only metal applied to the surface of the coins in order to give them a rich and shine appearance. Other intentional plating elements were carried out with antimony or arsenic, for example.

(iii) Minor elements

There are a number of factors which can give rise to systematic variations in the concentration levels of minor elements in antique copper alloys, including, for example, the mineralogy of the copper ore source; partition, volatilisation and contamination of trace elements (from various sources) during the smelt between metal and slag phases; the deliberate addition of other metals (e.g. tin or lead) to the finished metal; co-smelting of different ores to produce alloys directly; the poly-metallic ore sources that would naturally create alloys in the smelt; and changes in chemistry through melting, re-melting and working of the metal [25].

Elements such as lead, tin, antimony or zinc, nickel and cobalt, gold or even silver can be present on the surface of copper alloy coins [5, 10, 21, 23, 28, 34]. Lead (Pb) due to its compact structure and large atoms forms a good alloy with other elements in particular with copper [23]. Concerning the presence of this element on the coin surface, it is related to its very low solubility in copper and its low melting temperature with respect to that of the copper matrix, which causes the formation of fine particles dispersed throughout the copper [5]. Generally, less amount of lead is an effective evidence for a good refining process [21, 34]. Ingo *et al.* [5] put forward the hypothesis that the presence of antimony (Sb) could have been enhanced by the craftsmen, firstly during the blank production thus inducing the occurrence of the inverse segregation phenomenon on the outermost region.

The hypothesis that minor elements concentrations should be a guide to the provenance of antique metals has been around for more than a hundred years and explored for decades [10, 21]. The content of these elements can be governed by ore composition or related to the smelting process. In fact changes on minor elements levels give important information about the ore provenance [12].

1.1.2.1 Provenance

The most difficult question in numismatics is the attribution of provenance [10]. Either the mine is known and the goal is to correlate the objects to it, or the mine is unknown and the target it to determine which mine was exploited to make the objects. However, the place of origin/burial is of great importance to understand the mechanism of the phenomena responsible for the deterioration.

Based on literature [15, 21, 25] it is possible to elaborate **Table 1.2** which presents a list of elements that were deliberately alloyed with copper as well as those stemming from the ore extraction. Only a very limited range of trace elements are directly related to the provenance of the ore. Even more, in earlier times it cannot be assumed that deliberate alloying occur.

Table 1.2 – List of reported elements in antique and native copper and their potential uses in achaeometallurgy.

Technology	Provenance and/or technology	Provenance
B, Ba, Be, Cr, Cs, Ga, Ge, Hf, Li, Mn, Mo, Na, Nb, Rb, S, Sc, REE[c], Sr, Ta, Ti, Th, U, V, W, Y, Zr	Al[b], As, Ca[b], Cd[a], Cl[b], Co, Fe[b], In, Hg[a,b], K[b], Mg[b], P[b], Re, Si[b], Sb, Se, Te, Tl[a]	Au, Ag, Bi, Ir, Ni, Os, Pd, Pt, Rh, Ru
Sn > ca. 1%	Sn < ca. 1%	
Zn and Pb> ca. 5%	Zn and Pb< ca. 5%	

[a] Only applicable with native copper. [b] Soil contamination. [c] Rare Earth Elements.

1.1.2.2 Manufacturing

Coin minting obeys to several laws of the monetary system (national and/or worldwide) and its values are linked to a monetary standard. Moreover, there is the intent to produce objects that will last and can be easily distinguished from one another.

Ferraro Vaz [1] presents a resume about the antique Portuguese coins manufacturing process. According to this author, when a coin is hammered or milled the metal is prepared in disks and then submitted to the minting by manual pressure, marking them with the letters and figures (usually different) in both faces (obverse and reverse).

Studies presented by Guerra [10] show that varying the ratio of some minor elements with respect to the major ones (usually silver, copper or gold) may indicate a deliberate addition of a specific element to the alloy, meaning a change in the manufacture technology.

1.1.3 Coin deterioration

Studies on corroded metallic archaeological artefacts are of great importance since they can improve knowledge in the field of the long-term corrosion phenomena providing help, to scientists and conservators, in order to control and stop the process of deterioration of historic metals in museums and in selecting their ideal storage conditions; or even on its historical and archaeological classification [11, 17, 28]. However metals are generally difficult materials to analyze once they might have been re-melted and reused in new minting or for producing other objects [10].

Coins are very sensitive samples to the effect of deterioration processes. Their state of conservation depend on normal wearing processes before and after burial, being the extent and depth of the corrosion phenomena closely dependent on the corrosive environment (chemical composition, pH, resistivity, etc) and other non-negligible parameters, such as the type of electrolyte and the alloy microstructure, historical periods, metallurgical techniques or even the kind and size of the artefact [2, 15, 28, 29].

Based on these assumptions the interaction of archaeological artefacts with the neighbouring environment becomes very important in the field of preservation and corrosion. Most studies of different environmental conditions (soils [28, 35, 36], atmosphere [37- 43] and marine exposure [18, 28, 44, 45]) tried to establish the correlation between the artefacts chemical composition, its surroundings and their patinas structures.

Apart from corrosion occurring in air and wet soil it has to be considered that such leaching phenomena can also be caused by chemical treatments of the objects. In organic or inorganic acidic solutions the less noble constituents of the alloy are dissolved, while the nobler components, e.g. silver or gold, are enriched at the surface [32].

1.1.3.1 Coin patina

Patina is a coating of all chemical compounds such as corrosion products (namely, oxides, carbonates, sulphides and sulphates, nitrites and nitrates, phosphates, etc.) and other exogenous elements (silicon, calcium, etc.) formed and retained on the surface of the pure or alloyed metal, changing its surface texture and colour [6, 40, 46]. It can be produced and changed by chemical processes, wear, polishing, age, or, principally, due exposure to

atmospheric elements (air, rain, soil, etc.). As that it is important to consider the alloy/patina/environment as a global system in which the patina must be regarded as the result of the physicochemical interactions between the alloy and the environment, with time [29].

Patinas are built up during relatively short periods of time (6-50 years) with respect to the total conservation environment duration (hundreds to thousands of years). Once formed, patina layer is relatively stable and it becomes a permanent part of the object acting as a protective barrier, attenuating or eliminating the corrosive phenomena [13, 40, 41]. Copper patinas are generally regarded as aesthetically pleasing to the point of being purposely deposited on the metal surface by artists and metalworkers.

1.1.3.2 Usually compounds and their formation reactions

Corrosion of archaeological artefacts is studied through the analyses of its patina products. The knowledge of its constituents is the first step to understand the corrosion mechanism. Since the morphology of the patinas, their adhesion and degree of porosity are dependent on the climatologically conditions, nature and level of pollutants, each metal behaves in a different way and forms specific compounds that reflect the chemical properties of the metal and the environment to which it is exposed.

Initially the interface metal/medium is formed by cuprite (Cu_2O) (**Reaction 1.1**) [13, 15, 27, 40, 41, 46]. This compound is also the dominating phase that constitutes about half of the total patina mass [40] and it growths proceeds for years, centuries, or millennia, and may reach thicknesses of the order of several tens of micrometers [13].

$$4Cu + O_2 \rightleftharpoons 2Cu_2O \qquad \textbf{Reaction 1.1}$$

Since Cu_2O suffers an increasing rate of nucleation with increasing the relative humidity (RH), due the higher quantity of adsorbed water clusters that acts as nucleation sites, its reaction formation is RH dependent [43]. **Reaction 1.2** shows the cuprite oxidation, noticing that it does not take place any further in the later stage of the corrosion [39, 46]. Moreover, oxidation of cuprite under atmospheric conditions must be slower than that of copper otherwise the intermediate cuprite would not exist. **Reaction 1.4** represents the balanced redox reaction for the anodic and cathodic reactions in oxygen presence (**Reactions 1.2** and **1.3**, respectively):

$$Cu_2O + 2H^+ \rightarrow 2Cu^{2+} + H_2O + 2e^- \qquad \textbf{Reaction 1.2}$$

$$2H_2O + O_2 + 4e^- \rightarrow 4OH^- \qquad \textbf{Reaction 1.3}$$

$$2Cu_2O + 4H^+ + O_2 \rightarrow 4Cu^{2+} + 4OH^- \qquad \textbf{Reaction 1.4}$$

Cuprite is formed on the surface and later converted into other chemical compounds in agreement with the environment. Hydroxides and hydrated compounds of Cu (II) could be formed after the long-term (<1000 years) due the interaction between the coins, its first patina layer and the corrosion environment [27].

Table 1.3 presents a resume on the most commonly crystalline copper compounds found and studied over different patinas on copper and copper alloys artefacts.

Table 1.3 – Most commonly crystalline copper compounds found in patina of Cu/Cu-alloys artefacts.

Name	Formula	Colour	Reference
Cuprite	Cu_2O	Red-brownish. Becomes black over time.	[13, 15, 27, 40, 41, 46]
Tenorite	CuO	Steel-grey, black	[13]
Malachite	$Cu_2CO_3(OH)_2$	Green	[13, 15, 27]
Atacamite	$Cu_2Cl(OH)_3$	Green	[15, 27, 41, 46]
Brochantite	$Cu_4SO_4(OH)_6$	Green	[15, 41, 46]
Azurite	$Cu_3(CO_3)_2(OH)_2$	Blue	[27]
Nantokite	CuCl	Colourless, greyish to green	[13]
Paratacamite	$Cu_4Cl_2(OH)_6$	Green	[13, 41]
Antlerite	$Cu_3SO_4(OH)_4$	Green	[40]
Posnjakite	$Cu_4SO_4(OH)_6.H_2O$	Blue	[41, 46]
Langite	$Cu_4SO_4(OH)_6.2H_2O$	Blue	[40]
Gerhardtite	$Cu_2NO_3(OH)_3$	Green	[40]
Chalcopyrite	$CuFeS_2$	Yellow	[30]
Chalcocite	Cu_2S	Black	[15]

Patina colours are directly connected to the nature of the corrosive environment and not to the composition of the alloy. However, they cannot be considered as a valid criterion for providing a quick identification of typical corrosion products.

Depending on the environment, tenorite (CuO) (**Reaction 1.5**), malachite ($Cu_2CO_3(OH)_2$) (**Reaction 1.6**), atacamite ($Cu_2Cl(OH)_3$) (**Reaction 1.7**) and brochantite ($Cu_4SO_4(OH)_6$) (**Reaction 1.8**) are the principal patina constituents on copper-silver alloys, being the three last ones only compatible with oxidizing conditions; while compounds as cuprite (Cu_2O), chalcocite (Cu_2S) and nantokite (CuCl) (**Reaction 1.9**) are formed under typical reducing conditions, unless the conditions varies imposed by organic and/or inorganic matter in the medium.

$$2Cu + O_2 \rightleftharpoons 2CuO \qquad \textbf{Reaction 1.5}$$

$$Cu_2O + H_2O + CO_2 + ½O_2 \rightarrow Cu_2CO_3(OH)_2 \qquad \textbf{Reaction 1.6}$$

$$2Cu_2O + 2Cl^- + O_2 + 4H_2O \rightleftharpoons 2Cu_2Cl(OH)_3 + 2OH^- \qquad \textbf{Reaction 1.7}$$

$$2Cu_2O + SO_4^{2-} + O_2 + 4H_2O \rightleftharpoons Cu_4SO_4(OH)_6 + 2OH^- \qquad \textbf{Reaction 1.8}$$

$$Cu_2O + 2Cl^- + 2H^+ \rightarrow 2CuCl + H_2O$$ **Reaction 1.9**

In fact what usually happens is the inter-conversion of cuprite, generally by its oxidation, into several different compounds according to the different environmental conditions. Beyond those exposed above, for example, azurite ($Cu_3(CO_3)_2(OH)_2$) (**Reaction 1.10**) or paratacamite ($Cu_4Cl_2(OH)_6$) (**Reaction 1.11**) formation reactions:

$$3Cu_2O + 2H_2O + 4CO_2 + {}^3/_2\, O_2 \rightarrow 2Cu_3(CO_3)_2(OH)_2$$ **Reaction 1.10**

$$2Cu_2O + 2H_2O + 2HCl + O_2 \rightarrow Cu_4Cl_2(OH)_6$$ **Reaction 1.11**

Due Cu_2O oxidation, pH of the aqueous layer increases, while the formation of copper sulphates (e.g. brochantite or posnjakite) and the presence of weak atmospherics acids (e.g. formic, acetic, oxalic and/or carboxylic acids) act as buffers making the pH reaming at its equilibrium for the sulphates formation, increasing the time of reaction [46]. **Reaction 1.12** shows the reaction on brochantite stability domain. Even more, posnjakite is a hydrated form of brochantite and could be formed as a precursor of it. Studies made by Fitzgerald *et al.* [46] show that pH increases until tenorite is formed on the surface of cuprite and stifled further oxidation. Brochantite dissolution and the formation of tenorite under these conditions are given by **Reaction 1.13**.

$$4Cu^{2+} + SO_4^{2-} + 6H_2O \rightarrow Cu_4SO_4(OH)_6 + 6H^+$$ **Reaction 1.12**

$$Cu_4SO_4(OH)_6 \rightarrow 4CuO + SO_4^{2-} + 2H_2O + 2H^+$$ **Reaction 1.13**

There exists a critical SO_2 deposition rate above which brochantite does not form and existing patinated surfaces will dissolve [46].

Some of these compounds can be used at screening for the coins "survival" for so many years. Even more, they can be associated with particular environments. Generally, malachite presence suggests that the object could be buried (in soil); brochantite has normally origin in the atmosphere contact; atacamite and paratacamite suggest the presence of chlorides in the place of burial (maybe near seawater) and chalcocite the presence of anaerobic reducing environments [15, 26].

Finally, is important to notice that noble metals (e.g. Ag) accelerate corrosion, while the most catholically active ones (e.g. Pb, Sn) protect it during a certain period [13]. Silver does not react readily with the oxygen at room temperature. However, as shown before, adsorbed water layers into the oxide structure promotes irregularities that allow the penetration of corrosive ions. In consequence silver may suffer corrosion due to local action cells according to the **Reactions 1.14 to 1.16** [14, 15]:

$$4Ag + 4NaCl + O_2 + 2H_2O \rightleftharpoons 4AgCl + 4NaOH$$ **Reaction 1.14**

$$4Ag + 2H_2S + O_2 \rightleftharpoons 2Ag_2S + 2H_2O$$ **Reaction 1.15**

$$4Ag + O_2 \rightleftharpoons 2Ag_2O$$ **Reaction 1.16**

Moreover, silver can also suffer attack by Cu (II) ions in the presence of chloride ions [15] as **Reaction 1.17** shows:

$$Cu^{2+} + 2Cl^- + Ag \rightleftharpoons AgCl + CuCl$$ **Reaction 1.17**

The silver chloride, although insoluble in water, does not grow as a protective coating on the surface, so this reaction is rendered decisively corrosive in the copper enriched areas being induced by oxygen and humidity [15].

1.1.3.3 Patina structural aspects

Divalent metal ions such as Cu^{2+} commonly form compounds with layered structures. Copper patina, typically, consists of two distinct layers: a 5-15 μm inner layer of essentially continuous cuprite and an external, porous layer, about 5-40 μm of basic copper sulphates, chlorides and carbonates [14, 17, 39, 40, 46]. However, it can continue to grow during many years or even decades of exposure and may reach a thickness of the order of several tens of micrometers [10, 40]. These layers are held together by sulphate groups, hydrogen bonds and weak Cu-O bonds and, in spite of the structural resemblance between the compounds, the fact is that the phases have different cell symmetry [40]. For example, native silver and native copper, cuprite, nantokite and chlorargyrite present a cubic crystal system; atacamite is orthorhombic; and malachite, tenorite, brochantite and azurite present a monoclinic cell symmetry. This structural resemblance suggests that one phase can act as seed crystal for the formation of a subsequent phase.

Figure 1.1 shows a scheme for the general patina evolution on copper artefacts, displaying the formation of different compounds as a function of exposure time in different environments. One consequence of the gradual evolution of patina is that it gradually becomes less soluble and, hence more resistant to atmospheric corrosion [40].

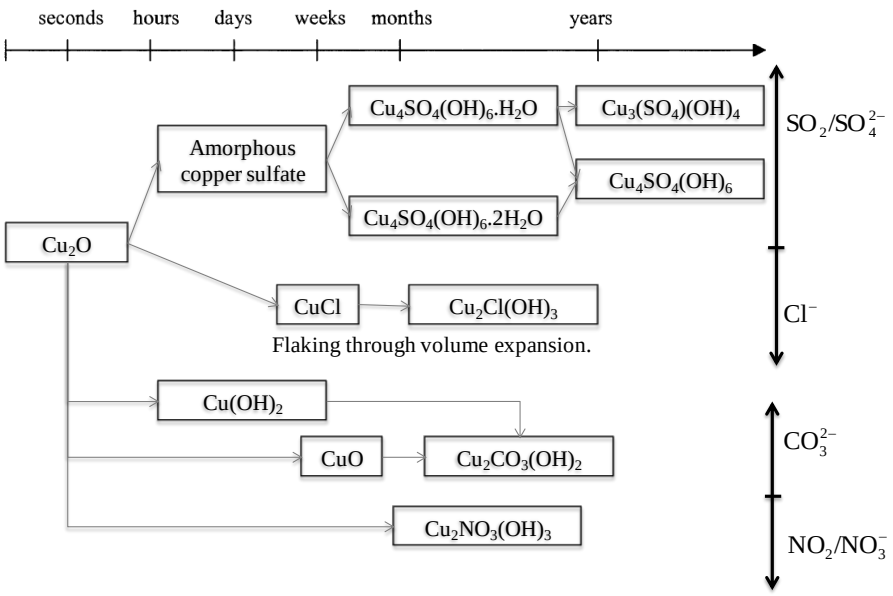

Figure 1.1 – Patina evolution scheme on copper artefacts along time and environment of exposure.

Robiola *et al.* [28] established a new structure patina classification of copper based alloys (particularly, Cu-Sn alloys), when exposed to an oxygenated corrosive medium. In resume, they assert that the corrosion patterns can be differentiated into two categories, according to patina colours, aspects and state of preservation of the original size of the object (i.e. the original surface limit) and based on its microstructures identification and characterization. Both categories can be observed on one and the same artefact. He *et al.* [27] later added that this double-structured deposit consist of an inner layer of Cu (I) salts and an external layer of Cu (II) compounds, which are depended on the history and the elemental composition of the object. Basically, Type I or "even" surface patinas build up under a mild corrosion condition and in a relatively short period of time being very protective and strongly influenced by the presence of incorporated soil components. While Type II or "coarse" surface patinas are thicker patinas formed when the original surface has been destroyed or deformed by severe corrosive attacks during the early stage of exposure.

As the bronze corrosion process leads to a preferential dissolution of copper ions into the environment, exogenous elements (textiles or leather, insects, woods or even pure organic matters) can be entrapped in the corrosion layers or mineralised [29].

1.1.3.4 Patina and the corrosive environment

The importance of exploring the influence of environmental conditions on atmospheric corrosion rates of metals is justified by prediction of future corrosion rates as well as to control its degradation. Changes in land use, new large industries, afforestation, highway

engineering or lowering the groundwater table are some human factors which contribute for a change in the different environments.

(i) Exposure to humidity and air pollutants

Exposures to humidity or air pollutants create difficult multiphase systems to study. Several corrosive species and corrosion products that interact with each other are present and all of them vary in amount and time. Even more, humidity, precipitation and wind play an important role on the atmospheric pollutants transportation and deposition on the object.

Electrochemical corrosion of copper is dependent on the type of metal as well as the pollutants present in the system. Once the metal dissolution occurs in presence of an electrolyte provided by atmospheric precipitation or by adsorption of water molecules on the surface of the corrosion layer, relative humidity plays a central role among the climatic factors. Especially since the presence of corrosive species which attract water vapour become soluble above a critical RH, lead to a sharp increase in the corrosion rate [39].

Among the most abundant contaminants are sulphates, nitrates and nitrites, ozone, chlorides, carbonates, hydrogen ions, ammonium, metal ions, atmospheric particles and also organic compounds.

Generally and based on literature [39, 42, 43] ozone (O_3) has the strongest effect on the corrosion of copper followed by nitrogen dioxide and sulphur dioxide (NO_2 and SO_2, respectively). Even more, O_3 and NO_2 led to a uniform corrosion attack while in the presence of SO_2 a locally attack can be observed [39].

Ozone is recognised to be a potential corrosion accelerator in corrosion research originating metal loss and hindering the passivation layer formation. This occurs possibly due O_3 strong oxidative power and because it can produce hydroxyl radical, which is balanced by the metal dissolution [39]. Moreover, the exposure to ozone led to the formation of a considerable amount of water-soluble nitrites and to copper sulphite species oxidation, forming copper sulphates ($CuSO_4.xH_2O$) and increasing the Cu_2O formation [39, 43].

When exposed to NO_2 the major species formed on the copper surface are: Cu_2O and gerhardtite; moreover, when copper sulphide species are present this pollutant is able to oxidize them to $CuSO_4.xH_2O$ [13, 38, 39, 42, 43]. In water rinses nitrate dominates over nitrite [43]. Formation of gerhardtite can be a result of nitric acid (HNO_3) and dinitrogen pentoxide reactions [38, 39]. Due to the high water solubility of HNO_3 this pollutant dissolves easily in the adlayer and the chemical reaction on the metal surface is enhanced leading to a decreased surface resistance.

Sulphates can be supplied directly from rain water; via adsorption and oxidation of sulphur dioxide within the aqueous layer; or from aerosols [46]. However, deposition rates depend greatly on the nature and geometry of the surface. Adsorption of SO_2 on copper surfaces is strongly influenced by RH [46]. The interaction between a water covered metal surface and SO_2 can be described by **Reactions 1.18** to **1.21** sequence:

$$SO_{2(g)} \rightarrow SO_{2(aq)} \quad \textbf{Reaction 1.18}$$

$$SO_{2(aq)} \rightarrow HSO_3^- + H^+ \quad \textbf{Reaction 1.19}$$

$$\equiv M - OH + HSO_3^- \rightarrow \equiv M - SO_3^- + H_2O \quad \textbf{Reaction 1.20}$$

$$\equiv M - SO_3^- \rightarrow MSO_3^- \quad \textbf{Reaction 1.21}$$

After deposition and dissolution of SO_2 into the water layer (**Reaction 1.18**), a bisulphite ion (HSO_3^-) is formed by hydrolysis of sulphur dioxide (**Reaction 1.19**) producing a metal-sulphito surface complex ($\equiv M - SO_3^-$), through an exchange mechanism with the hydroxylated metal oxide surface ($\equiv M - OH$) (**Reaction 1.20**). Liquid metal-sulphito complexes (MSO_3^-) subsequently detach from the metal-surface (M) and precipitate as solid corrosion products (**Reaction 1.21**) [42].

The principal compounds found in copper patinas when exposed to SO_2 rich environments are cuprite, basic copper sulphates and sulphites [13, 39, 40, 43].

When sulphur- or chlorine-containing atmospheric species are more dominant, the patina formation reaction sequence becomes more complex and involves more copper patina constituents [40].

Conventional atmospheric parameters that affect copper generally affects silver too comprising weathering factors (temperature, moisture, radiation, wind velocity, etc.), air pollutants and aerosols. In presence of a strong oxidizer, silver rate corrosion increases [37].

(ii) Exposure to marine environments

Marine environments, such as coastal or near-coastal countries as Portugal, are chloride (Cl^-) rich environments.

Urban atmosphere patinas are, in general, more adherent and uniform, than the ones exposed to chloride-rich environments. These last patinas are generally heterogeneous and present flaking and scaling, which allows localized corrosion; however, in the marine atmosphere patinas the degree of adhesion increases with time [18, 41, 44]. Zhang *et al.* [44] concluded that flaking mechanism associated to these loosely adherent patina layers is connected with the formation of nantokite.

In chlorine-polluted environments a general stratification of corrosion products for a mature film is mainly composed of cuprite, as the initial phase in the evolution of the copper patina (inner layer), followed by the interfacial region in-between of CuCl which commonly transforms into the more voluminous corrosion product of atacamite or the isomorphous phase paratacamite, which correspond to the outer layer [6, 18, 40, 41, 44, 45]. According to Wallinder *et al.* [18] the composition of the outer part of the patina layer and its solubility properties are major factors that influence the extent of released metals, originating an increase of corrosion rates and the consequent metal loss. Even more, due paratacamite is most voluminous than nantokite, it induces internal physical stresses that leads to a separation between the inner patina layer and the outer deposit which induces the flaking process on copper [44]. This process is facilitated by the porous nature of the patina that allows penetration of moisture (water) and oxygen inducing an autocatalytic corrosion of copper [15, 18, 44] according to **Reactions 1.22** and **1.23**. Moreover, He *et al.* [27] claim that on the archaeological copper alloys the chloride anion was one of the major causes for bronze corrosion in soil.

$$O_2 + 4H_2O + 4CuCl \rightarrow 2Cu_2Cl(OH)_3 + 2HCl \qquad \textbf{Reaction 1.22}$$

$$2HCl + 2Cu \rightarrow 2CuCl + H_2 \qquad \textbf{Reaction 1.23}$$

The method of cuprite production in the presence of the Cl^- ion is a precipitation reaction. The equilibrium in **Reaction 1.24** is shifted to the right as the local concentration of, e.g. $CuCl_2^-$ (**Reaction 1.25**) complex increases and Cu_2O is deposited in response [45]:

$$Cu^+ + 2Cl^- \rightleftharpoons CuCl_2^- + Cl^- \rightleftharpoons CuCl_3^{2-} + Cl^- \rightleftharpoons CuCl_4^{3-} \qquad \textbf{Reaction 1.24}$$

$$2CuCl_2^- + 2OH^- \rightleftharpoons Cu_2O + 4Cl^- + H_2O \qquad \textbf{Reaction 1.25}$$

The stability of Cu_2O is inversely dependent on the concentration of chloride ions. Thus the rate of re-dissolution of the protective cuprite is much higher than that observed in neutral/alkaline solution. An increasing pH resulting from the oxygen reduction reaction will favour the consumption of CuCl complex to form cuprous oxide [45]. According to Kear *et al.* [45] the buffering properties of seawater (due to the presence of carbonate/bicarbonate and borate ions) will act to limit any change in pH of the electrolyte adjacent to the active surface.

(iii) Soil exposure

Metal corrosion in soil media varies according the supply of an oxidizing agent (usually oxygen from the air) and the presence of an electrolyte (a water solution).

The extension of the corrosive phenomena is dependent of several soil parameters, namely soil texture and grain size, soil acidity (pH, buffer capacity) and the amount of soluble salts, as well as their richness in chloride or phosphate and presence of soot, which affects the capillary of the soil giving more, or less, access to water and air [35, 36, 28]. Moderately aerated and moist soil above the ground water table (e.g. sand) generally promotes corrosion of metals giving access for O_2 at the same time as the pores are partly filled with H_2O. On the other hand a fine-grained soil or a coarse-grained soil (e.g. clay and gravel or pebble, respectively) should be less harmful. In fact, the aggressiveness of different soil types toward buried metal structures is a more important factor than the total age in years [35, 36].

It must be noticed that the chemical composition and properties of archaeological soils change over time as well as climate and activity on the site. In fact deterioration of buried metallic objects sensibly accelerated during the last 50-100 years, as a result of the technological progress and new agricultural practices [2, 28, 36].

Especially well preserved metal objects are usually found in calcareous regions, or in peat or bogs due to the absence of oxygen. Copper phosphates are not generally found as corrosion products except in characteristic environments in association with decomposing buried bones and in arid climate [30]. In the presence of sulphur or sulphate-rich soils, generally produced by the decomposition of organic matter in an almost oxygen-free environments, posnjakite, brochantite and antlerite are the most common find compounds [13, 30]. Finally, compounds formed from elements in the soil (Si and Al) and Pb may have resulted from corrosion of metallic objects associated with the use of weapons [16].

1.1.3.5 Corrosion inhibitors

To improve the protective efficiency of copper corrosion great efforts have been put into investigation and lots of technologies have been used [20; 47, 48, 49]. One of the most studied and *avant-garde* method for preventing the atmospheric corrosion of copper is the use of an appropriate inhibitor. Generally film assembling inhibitors based on green chemicals are preferred for this purpose [47]. However volatile corrosion inhibitors are the most effective and affordable for industrial use [48].

The use organic molecules containing O, N, S and polar functional groups as corrosion inhibitors for copper and copper alloys have been widely investigated, in order to understand their strong adsorption on the metal surface by plugging the active sites and forming protective films on it, being its efficiency dependent on the film characteristics, namely the nature and the surface charge of the metal, the adsorption mode, its chemical structure and the

type of the electrolyte solution formed [19, 20, 47-49]. Specially, amines and azole derivatives have been reported to be very effective inhibitors in acidic and neutral corrosion media [49] due their polar hydrophobic end groups which stabilizes the adsorption process [19, 47, 49].

In the other hand, the main advantage of volatile corrosion inhibitors compared with conventional corrosion control methods, are their gas-phase transport that enables metallic surfaces to be reached. Even more, this films are very thin and do not interfere with subsequent use or treatment of the surface [48].

In resume and based on literature, some examples on new corrosion inhibitors, are described in **Table 1.4**.

Table 1.4 – Examples of some recent copper corrosion inhibitors.

Compound	Chemical structure	Reference
3-((2-mercaptophenyl)imino)butanoate (MMPB)	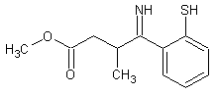	[47]
Benzotriazole (BTAH)	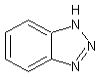	[48]
2,5-Dimercapto-1,3,4-thiadiazole (DMTD)	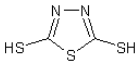	[20]
5-(3-aminophenyl)-tetrazole (APT)	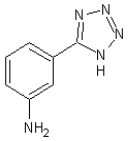	[49]

Tansug *et al.* [47] examined MMPB inhibition ability in acidic chloride media concluding that the high efficiency of it was related with its ability to complex with Cu (I) at the surface. Once the adsorbed molecules interact with each other along the carboxylate tails a film-like adsorption layer is formed on the surface [47]. BTAH and its derivatives can be used specifically for atmospheric Cu corrosion protection according to Chen *et al.* [48]. This compound acts as a mixed corrosion inhibitor interacting, via N atom, with the Cu (0) to form a thin protective film in non-corroded areas and with Cu (I) to outline a thick polymeric complex on the Cu_2O substrate on the defect sites [48]. Qin *et al.* [20] studied the DMTD and Sherif *et al.* [49] used APT. In both cases a protective monolayer film against copper corrosion in acidic solution is formed. They are good inhibitors due their strong adsorption on the copper surface, increasing surface and polarization resistances.

1.2 PAPER

The word "paper" is etymologically derived from *papyrus*, the word for the *Cyperus papyrus* plant and which was used to produce a thick, paper-like material by the ancient Egyptians, Greeks and Romans [50]. However papyrus and paper are different materials. The first one is a "lamination" of the natural plant, while paper is manufactured from fibres whose properties have been changed by maceration or disintegration.

Due to its historical, scientific and social importance is easily understood the importance of paper conservation once it is one of the most fragile guardians of people cultural heritage.

1.2.1 Paper history and social impact

Papermaking has traditionally been traced to China, about 105 a.C., when T´sai Lun, an official attached to the Imperial court, created a sheet of paper using rags (textile waste) as the raw material. The earliest piece of paper found was discovered at Fangmatan (Gansu, China) inscribed with a map.

Paper spread from China, through the Middle East to medieval Europe in the 13rd century and since that time, paper was the main material for recording cultural achievements all over the world [51]. Although the notion of paper being used as a practical everyday item, did not occur until the 15th century, the advantages of mill-based papermaking spread throughout Europe in the 15th and 16th centuries [50, 52].

On the 18th and 19th centuries Industrial Revolutions gave rise to new papermaking machinery that severely macerated the pulp and fast heat-dried the paper. Even more, the use of sulphuric acid and chloride as bleaches and the replacement of gelatine by alum-rosin for internal sizing[6] made from this epoch one of the most important ones in paper history [53]. After the invention of printing, paper demand consistently increased and the methods of papermaking radically changed. In the middle of the 19th century papermaking from rags was replaced by the use of wood pulp [54].

Paper as a carrier for written information was introduced in Europe on the 20th century [55]. In the past 50 years the rate of innovation in papermaking has increased rapidly and nowadays paper can be impregnated, enamelled, creped, waterproofed, waxed, glazed, sensitized, bent, folded, twisted, crumpled, cut, torn, dissolved, moulded and embossed [50].

[6] The definition is presented on **Annexe I**.

1.2.2 Chemical composition of paper

Paper has several components which can be classified according to their origin; chemical structure and function, note that wood-derived fibres are mainly composed of cellulose but also of lignin, hemicelluloses and other minor components; mineral particles acting as fillers (e.g. talc, kaolin, calcium carbonate, etc.); natural sizing agents (starch or rosin) or synthetic ones (alkyl ketene dimer or alkenyl succinic anhydride) which are generally acidic; colorants; functional groups forming during papermaking (e.g. aldehydes, ketones, carboxylic groups); metal ion impurities (mainly iron and copper); and other substances which can improve the characteristics of the paper for printing or writing and may also contribute to its degradation phenomena [51, 55, 56].

Antique paper was made entirely from rags, i.e. from linear long cellulose fibres only with the addition of sizing compounds; whilst contemporary paper can be manufactured from short fibres and may contain non-fibrous components in order to improve its properties. However the change of fibre source from cotton and linen rags to wood fibres and the use of alum rosin sizes had significant adverse effects on the permanence and durability of paper materials. Nevertheless, the ageing behaviour of a paper is determined by its manufacture, not the original source of the fibres [52]. As that, both paper composition and environmental conditions are decisive factors for the stability and durability of paper.

1.2.2.1 Cellulose

Cellulose is a long chain carbohydrate, natural polymer that gives wood its strength. It is the main component of plant cell walls and the basic building block for many textiles and for paper (almost 90% of paper constitution) [57]. Chemically, pure cellulose is a very stable material at ambient temperature [58].

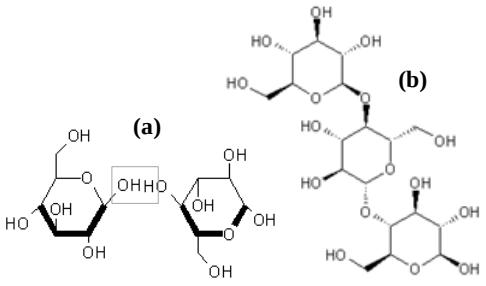

Figure 1.2 – Cellulose structure: **(a)** two unlinked molecules of ß-D-glucose and **(b)** cellobiose.

The links in the cellulose chain are a type of sugar. These sugar units are bonded when water is eliminated by combining the -OH group with the H atom (**Figure 1.2 (a)**). Linking just two of these sugars produce a disaccharide called cellobiose (**Figure 1.2 (b)**); here

glucose units are linked through a ß-(1,4)-glycosidic bond originating long chains that form crystallites. Hereupon cellulose is a polysaccharide produced by linking additional sugars in the exactly same way to form regular, hard and stable regions that give the bundled chains more stability and strength [55, 57]. The length of the chain varies greatly from a few hundred sugar units, in wood pulp, to over 6000 for cotton, the purest natural form of cellulose [57].

1.2.2.2 Lignin

Lignin is an amorphous, aromatic, water insoluble, heterogeneous, three dimensional (3D) and cross-linked polymer (**Figure 1.3**). This material is not composed of exactly repeating units and can be described better as a macromolecule than as a polymer.

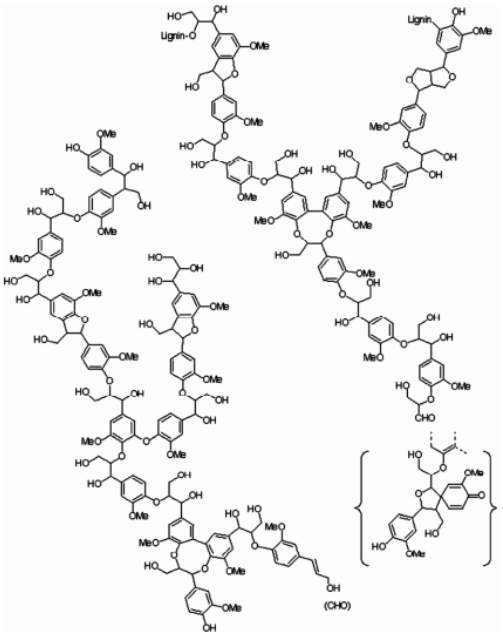

Figure 1.3 – Structural model of softwood lignin [59].

Lignin gives woody plants their physical strength however it reduces the strength of paper by interfering with the way that cellulose fibres assemble. Its function is to provide a mechanically strong composite material with cellulose [60]. Moreover this macromolecule is the main cause of photo-yellowing of paper. In its structure are present several chromophores with conjugated aromatic rings and carbonyl groups that absorb in the near UV spectrum (300–400 nm). When these chromophores absorb light they can decompose into yellow coloured ketones and quinones, turning the paper yellow. Since these molecules themselves absorb visible light, they act as secondary chromophores and can react further, exacerbating the yellowing and degradation processes, this is why paper yellows with age [55, 60].

1.2.3 Paper deterioration

Paper deterioration is a very slow and multi-parameter process. It is caused by endogenous (pH, metal ions, lignin, degradation products) and exogenous (RH, oxygen, light exposure, heat or pollutant gases) contributions. Paper chemical and mechanical properties, stability, degradation, etc. are strongly dependent upon the nature, origin and characteristics of cellulosic material as well as pulping and papermaking procedures, additives and its interactions, and storage conditions [55, 56].

Chemical, physical and biological processes may cause irreversible structural changes in the constituting fibres, resulting in discoloration and embrittlement. In fact, paper deterioration means the weakening of inter-fibre bonds which results in an intrinsic decreased of strength due to cellulose deterioration. The modes of cellulose degradation within paper include chemical, which could be acid (producing formic, acetic, lactic and oxalic acids) or enzymatic hydrolysis, alkaline and oxidative degradation (which is mainly followed by a radical mechanism and has an important role in the natural ageing of paper); thermal (different levels of temperature) and radiation (exposure to UV/Visible and/or high-energy radiation); and by the presence of microorganisms or even with ink or printing media that are used historically in writing and illustrating [53-55, 60]. In these modes of cellulose degradation, crystallinity or fibrillar morphology plays a decisive role in determining the rate and also the course of the degradation process. A high supramolecular order of the polymer chain generally prevents degradation [52, 55].

1.2.3.1 Manufacturing and storage

During manufacturing and since the latter half of the 17th century, hydrated aluminium sulphate was added as a sizing agent. At this time it was not yet known that this compound dissociates in water to form sulphate and hexaaquaaluminium(III) ions ($[Al(H_2O)_6]^{3+}$) that can undergo acid hydrolysis (**Reaction 1.26**):

$$[Al(H_2O)_6]^{3+} + H_2O \leftrightharpoons [Al(OH)(H_2O)_5]^{2+} + H_3O^+ \qquad \textbf{Reaction 1.26}$$

During storage air pollutants play an important role on paper deterioration. Nitrogen dioxide can both form nitric acid on reacting with the moisture in paper (**Reaction 1.27**) and/or oxidise the hydroxyl groups on cellulose fibres to carboxylic acids, increasing the acidity of the paper (**Reaction 1.28**):

$$3NO_2 + H_2O \rightarrow 2HNO_3 + NO \qquad \textbf{Reaction 1.27}$$

$$\text{Cellulose}-CH_2OH + 2NO_2 \rightarrow \text{Cellulose}-COOH + 2NO + H_2O \qquad \textbf{Reaction 1.28}$$

Sulphur dioxide can form sulphuric acid on reacting with the moisture in the paper. In oxygen presence, the oxidation of SO_2 followed by its hydration leads to acid production (redox **Reaction 1.31** result from **1.29+1.30** reactions). This reaction can be catalyzed by the presence of certain metals (e.g. manganese) introduced in the paper making process.

$$SO_2 + ½O_2 \rightarrow SO_3 \qquad \textbf{Reaction 1.29}$$

$$SO_3 + H_2O \rightarrow H_2SO_4 \qquad \textbf{Reaction 1.30}$$

$$SO_2 + H_2O + O_2 \rightarrow H_2SO_4 \qquad \textbf{Reaction 1.31}$$

1.2.3.2 Acid catalyzed degradation of cellulose

Acidic-catalyzed degradation of paper is the most common degradation reaction. It is initiated by the acidic species (especially alum) introduced into the cellulose fibres during papermaking, causing its hydrolysis and reducing its degree of polymerization, eventually degrading the fibres until the paper is disintegrated [55]. In addition, acid from polluted atmospheres can enter the low-density, open regions of the fibre and cut the polymer chain.

In general lignin, hemicellulose and hydrolyzed cellulose oxidize and produce substantial amounts of acidic products that breakdown the fibres. These acids further catalyze paper degradation and therefore this process is termed as "autocatalytic". **Reaction 1.32** [60] shows the acid-catalyzed hydrolysis of β-(1-4)-glycosidic bonds in cellulose. This reaction shortens the cellulose fibres lengths which lead to a loss of paper strength [54].

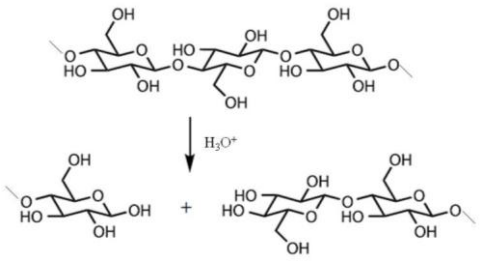

Reaction 1.32

The extend of depolymerization following the acid-catalyzed hydrolysis depends on the acid strength and concentration as well as on temperature and duration of the reaction [56].

1.2.3.3 Alkaline degradation of cellulose

When subjected to strong bases (such as $Ca(OH)_2$ or alcoholate) cellulose chain ends can react and undergo a depolymerization reaction. Its alkaline degradation mechanism involves various steps, e.g. β-alcoxy elimination ("peeling reaction" – **Reaction 1.33** [58]) which explains the detrimental effect on paper permanence of excessively strong bases (B). When B species are exposed to air, they are rapidly transformed into the corresponding carbonate [55].

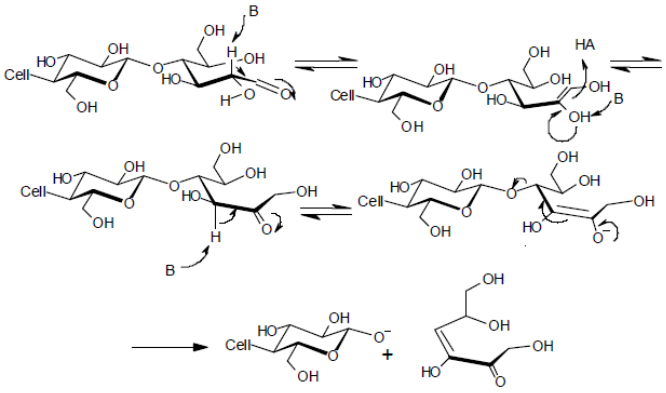

Reaction 1.33

These reactions must be considered when treating cellulose-based works of art with alkaline solutions for restoration purposes (e.g. deacidification processes) [56].

1.2.3.4 Oxidation of cellulose

The oxidative degradation of cellulose is primarily induced by the presence of oxygen which acts as a non-specific oxidizing agent via various complex mechanisms.

Oxidation of cellulose introduces side groups (namely aldehydes and ketones) that make the molecule more easily hydrolyzed. Indeed these oxidized cellulose groups are known as "potential" sites of degradation because oxidized cellulose chains are not "actually" broken but they can easily degraded in both acidic and alkaline medium, even at mild concentrations and room temperature [55, 56]. Even more free radicals, generated by oxidation or by light, can also cut the cellulose chain. Both cellulose (and its derivatives) and lignin within the paper can be oxidised leading to discolouration.

Reaction 1.34 shows the cellulose chain scission resulting from oxidation where **(a)** is the oxidation of the C3 hydroxyl to carbonyl originating a chain scission and **(b)** is the same process on the C2 hydroxyl resulting the keto-enol tautaumerization [58]. This process also contributes to raising the concentration of acid on paper.

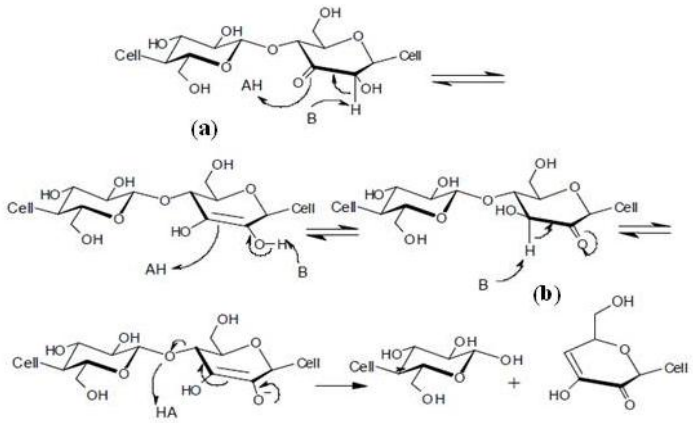

Reaction 1.34

1.2.3.5 Biological degradation of cellulose

Various biological contaminants are possible even in libraries and archives, and their effect can vary as a function of environmental situations and composition of the substrate. Insects and moulds are the most common cause of biological problems. However stopping this type of detrimental evolution is not easy because its origin is frequently due to improper storing conditions [55]. For example, moulds proliferate and reproduce themselves in organic substrates like cellulose which will provide feed for development. These fungi produce enzymes that will chemically attack fibres and cleave cellulose macromolecules. Moreover, their metabolism will produce acidic wastes, which contribute to paper degradation [55].

Gamma radiation eliminates insects and fungi in the paper, it has no residual toxicity or pollution and large volumes of material can be handled in short time [55].

1.2.3.6 Iron-gall ink corrosion

Ink-induced corrosion of cellulose is a primary threat for paper documents of all kinds. Prevention of further iron-gall ink corrosion is a crucial issue in conservation science [61].

Iron-gall inks were popular for several centuries until the mid-19th century. Metallo-gallate inks are typically composed by iron sulphate salt, ferrous sulphate and other sulphates in trace amounts; and a vegetable tanning agent, commonly gallotannin extracts from gall apples [61]. This constituent's act as powerful oxidation agents because large amounts of metals are present and these may lead to extensive localized degradation [55]. Depending on source and preparation, the iron sulphate also contains impurities, such as copper, zinc, aluminium and magnesium salts, establishing a complex system of different (de)stabilizing metal ions.

Their main reaction is accomplished in two different steps, as **Reaction 1.35** shows. First, gallic acid, formed by hydrolysis of the tannins extracts, reacts with ferrous cations from iron sulphate ($FeSO_4$), in water, to form ferrous (II) gallate and sulphuric acid **(a)**. After, in oxygen presence two molecules of this Fe (II) compound react, giving a ferric (III) pyrogallate and water **(b)**.

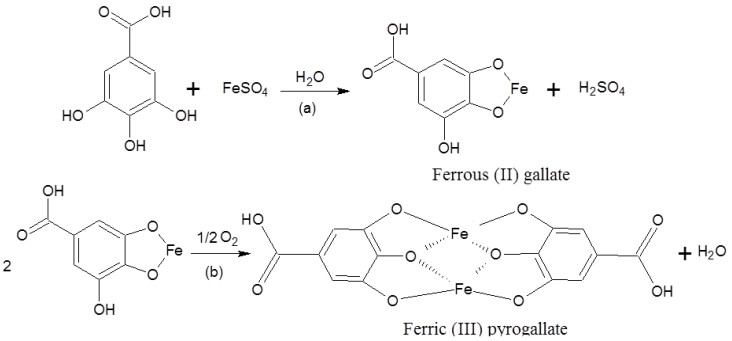

Reaction 1.35

The presence of Fe (II) ions excess can catalyze the oxidation of cellulose through the production of hydrogen peroxide, according to the Fenton mechanism[7], which induces severe degradation of paper by the loss of its mechanical properties (elasticity and tensile strength) as well as along the lines of the ink and the perforation of the inked areas [61, 62].

1.2.4 Paper conservation

Paper conservation is one of the most studied areas in the art and heritage conservation field. Particular and recently the nanosized particles subject.

Alkaline nanosized particles, applied from non-aqueous dispersions have found to be particularly efficient for the preservation of cellulose-based materials which degradation is catalyzed by acidification processes developing in the paper and leading to chemical disruption of the cellulose polymer [63] as exposed before.

It is well known today that the standard composition of paper should have an alkaline reserve (that is, the enough amount of buffer compounds capable of neutralizing acids) and have more than 1% lignin content, in way to prevent the paper deterioration. Deacidifying agents can provide this alkaline reserve, neutralizing the acidic groups present and avowing their acid hydrolysis. The use of non-acidic additives to make paper is becoming more prevalent and the stability of these papers is less of an issue. However an universal treatment of paper, able to deacidify, strengthen and protect against biological attack is still a challenge.

1.2.4.1 Deacidification agents

Deacidification is the neutralization of existing acids in the paper and a chelating step to inactivate the transition metal ions that are needed for a successful treatment [64]. This treatment is unavoidable in the preservation of paper because it provides a complete neutralization of paper and, in most cases, introduces an alkaline reservoir that opposes the incoming assault from the acidity present in the environment [65]. Correct deacidification process should produce the complete neutralization of the acidic paper and thermodynamically stable side products keeping the pH around 8-9 [54].

Although deacidification agents include strong bases such as sodium hydroxide (NaOH) the materials most often used for deacidification are weak bases, including carbonates, bicarbonates and some hydroxides, various oxides and amines [58]. Due the high compatible of these materials with the treated substrates it limits the drawbacks and ensures a long-lasting beneficial effect on the paper surface.

[7] The definition is presented on **Annexe I**.

1.2.4.2 Calcium carbonate and calcium hydroxide nanoparticles

Functionalization processes through nanoparticles surfaces can passivate, protect and/or functionalize them, for a specific goal. Based on literature [54, 63, 64] nanoparticles can be applied by spraying, brushing or immersion and their use does not require any special safety procedures. Their reactions and applications are usually simple to assemble and, in this particle case, relatively inexpensive.

These materials have found fundamental applications for the compatible preservation of both immovable (e.g. consolidation of wall-paintings) and movable (e.g. deacidification of paper and wood artefacts) works of art [56]. They penetrate within the cellulose fibres on paper and neutralize the inherent acidity, causing a strong reduction in paper aging. One of the most important features about these nanoparticles is their capability of nucleation and growth due its significance for the formation of inorganic crystals control [56].

(i) Carbonates

Calcium carbonate ($CaCO_3$) occurs as three anhydrous crystalline polymorphs (calcite, aragonite and vaterite), in two crystal forms (hexahydrate ikaite and monohydrate) and also as amorphous material. While calcite, with a rhombohedral symmetry, is the most thermodynamically stable polymorph of this compound, under ambient conditions, the other two anhydrous crystalline forms are metastable in nature (orthorhombic aragonite and the hexagonal vaterite crystal systems). Aragonite changes to calcite at 380–470°C and vaterite is even less stable [66, 67].

The applications of $CaCO_3$ particles are determined by a number of strictly defined parameters (e.g., morphology, structure, size, brightness, oil adsorption and chemical purity) [63, 68]. These nanoparticles can enhance properties of the coating such as weather resistance, anti-corrosion, rheological properties and low abrasiveness [69, 70].

Alkaline earth carbonates, namely calcium and magnesium carbonate, must be considered as leading candidates for deacidification of paper because of their chemical simplicity, relatively low cost, high brightness and suitability for use as paper fillers. However simple carbonates tend to be relatively insoluble in neutral water as well as in organic solvents, a factor that limits their manner of distribution on paper-based documents. Relatively pure calcium carbonate products, as all limestone and chalk, tend to buffer the pH in a more moderate range (7.5 to 8.5) in comparison with some precipitated $CaCO_3$ products that may contain some residual calcium hydroxide ($Ca(OH)_2$) (pH>9) [58].

One of the most problematic issues for the use of $CaCO_3$ is it hydrophilicity. Surface modification of this compound with hydrophobic species would lead to a great expansion in its applications [68, 71]. A way to solve this problem is to tailoring the surface properties of nanoparticles by using organic capping layers or chemically installing functionality on nanoparticles surfaces through organic synthesis [72].

(ii) Hydroxides

Suspensions or dispersions of alkaline earth hydroxides are typically used to achieve an almost instantaneous neutralization of free H^+ ions with water formation [56].

Baty *et al.* [58] report that micro- and nano-particulate dispersions of calcium and magnesium hydroxides show evidence of cellulose breakdown when unaged paper is treated; these adverse effects were attributed to excessively high pH.

Calcium hydroxide ($Ca(OH)_2$) proved to be an excellent deacidifying agent. It excess is slowly converted into carbonate because once the particles are deposited in paper, ensuring a good physicochemical compatibility with the support, they have the theoretical ability of reacting with carbon dioxide from the air, forming calcium carbonate (alkaline buffer) *in situ* and without originate any undesirable side products [54, 56].

(iii) Calcium carbonate and calcium hydroxide nanoparticles functionalization

Surface functionalization is the process of modification the nanoparticles´ surfaces through the introduction of specific chemical functionalities. This process can, for example, efficiently promote the dispersion of particles in a solvent. Organic additives can be introduced to the crystallization process to modify the crystal surfaces and to control the particle nucleation and growth, too.

Particularly, dodecanoic, or lauric, acid (DA) is a saturated fatty acid which is generally present in the form of a white powder and like many other fatty acids, is inexpensive and non-toxic, long shelf-life compound [73, 74].

DA is used in the present work as a surface modifier. It changes the $CaCO_3$ nanoparticles from hydrophilic to hydrophobic and it is also used to control the particle size and shape. The Ca^{2+} ions react with the DA to form a hydrophobic salt $Ca(C_{12}H_{23}O_2)_2$. After a CO_2 flow, the hydrophobic properties of the final calcium carbonate nanoparticles are attributed to the deposition of these salt molecules onto the $CaCO_3$ surface [68, 71]. According to Sarkar [66, 75] dodecanoic acid used as an additive during the preparation of calcium carbonate, favours the formation of aragonite over calcite. Thus, the acid initiates the phase transformation from thermodynamically stable calcite to metastable aragonite phase.

Calcium carbonate and calcium hydroxide nanoparticles synthesis

Despite of synthesis of nanoparticles is a simple process to carry out its thermodynamic tendency to agglomerate into bulk structures can be a problem. It is usually difficult to achieve the necessary high supersaturation degree for nucleation and the effect of co-ions at these concentrations can be critical. The effects of control parameters, such as reaction temperature, concentration of reacting species, and aging time of the nanostructure characteristics have been reported. Also, some studies report significant effects of organic solvents on the shape and size of the particles obtained by precipitation [63, 65].

There are two main different methods to synthesize nanomaterials, differentiated only by the starting material: top-down method - a material whose features are not in the nano-scale is worked to produce a nanostructure material; and bottom-up procedure - the nanostructures are built atom by atom from scratch. Different methods are very often combined to produce materials with the desired properties [56].

In the present study the paper by Chen *et al.* [68] is followed in order to test the new route proposed by the authors. Here, a top-down method is used. It starts from a bulk material that is broken into small pieces using mechanical, chemical and/or other forms of energy (temperature). The drawback is the poor control of the nanoparticles dimensions, since the smallest size that can be produced by grinding is limited by the tendency to re-aggregate and particles below a few microns cannot usually be produced [63]. The contaminations of the particle surface by atmospheric gases and by materials used for the mill are others disadvantages [63]. In this case calcium oxide (CaO), mixed with water, is used to synthesize $Ca(OH)_2$ (this reactions usually leads to a rather small amount of unreacted CaO) and then functionalized with dodecanoic acid (combination of steps **(1)** and **(2)** presented in the reactions below). After that and trough calcination with CO_2 the remaining hydroxide is precipitated in $CaCO_3$ (combination of **(3)** and **(4)** steps). By tuning the critical reaction parameters $Ca(OH)_2$ and $CaCO_3$ nanoparticles of different sizes and shapes can be produced. During this process the conversion of oxide particles to hydroxide is accompanied by a change in volume, which leads to a fragmentation of the particles and a reduction of their size. Finally, these particles can be effectively dispersed in a non-polar organic solvent (here, cyclohexane or nonane) trough ultrasound bath. In this particular the synthesis reaction is composed by four steps:

(1) Calcium oxide reaction with water producing $Ca(OH)_2$ (**Reaction 1.36**). Part of this dispersion is removed from the flask to dry and characterize. This compound can be dissociated in Ca^{2+} and OH^-(**Reaction 1.37)**:

$$CaO + H_2O \rightarrow Ca(OH)_2 \qquad \textbf{Reaction 1.36}$$

$$Ca(OH)_2 \leftrightharpoons Ca^{2+} + 2OH^- \qquad \textbf{Reaction 1.37}$$

(2) The calcium hydroxide which is not removed from the flask, reacts with an ethanol:dodecanoic acid solution producing a calcium laurate salt ($Ca(C_{12}H_{23}O_2)_2$) through the arrangement of the acidic ions with the free Ca^{2+} cations (**Reaction 1.38**):

$Ca(OH)_2 + 2$ 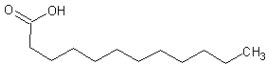 $\rightarrow [Ca^{2+}][$ 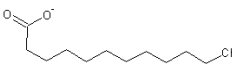 $]_2 + 2H_2O$ **Reaction 1.38**

(3) When carbon dioxide dissolves in water (present in the solution) it exists in chemical equilibrium producing carbonic acid (**Reactions 1.39** to **1.41**):

$$CO_2 + H_2O \leftrightharpoons H_2CO_3 \qquad \textbf{Reaction 1.39}$$

$$H_2CO_3 \leftrightharpoons HCO_3^- + H^+ \qquad \textbf{Reaction 1.40}$$

$$HCO_3^- \leftrightharpoons CO_3^{2-} + H^+ \qquad \textbf{Reaction 1.41}$$

(4) Finally the CO_3^{2-} anions react with the Ca^{2+} ions in excess producing calcium carbonate (**Reaction 1.42**):

$$CO_3^{2-} + Ca^{2+} \rightarrow CaCO_3 \qquad \textbf{Reaction 1.42}$$

The hydrophobic properties of the final $CaCO_3$ nanoparticles are attributed to the deposition of the resulted salt onto the calcium carbonate surface. Nucleation of calcite is induced by carboxylate functional groups. According to Chen *et al.* [68] this carbonation route can provide new insight into the industrialized production of $CaCO_3$ with complex morphology.

2 TECHNIQUES

Most of the archaeological objects, regardless their form or materials, are unique and most of the times cannot suffer sampling. Therefore the analytical methods/techniques applied to such samples should be non- or micro-destructive, preserving the integrity of the object. This is especially important when valuable antique artefacts are investigated or trace element analysis is required.

2.1 Coins visual analysis: a macro scale morphologic approach

The general appearance of the corroded surface is of great importance not in order to establish a direct identification of the patina products, since this assumption may induce some evaluation mistakes but in order to observe typical corrosion areas such as "cauliflower" corrosion crust. In fact, this specific type of corrosion is considered to be a particular form of "black spot" and can be distinguish by its structure (cauliflower-looking like) that can grow in spots or cover wider areas, and colour, mostly brown/black [76, 77].

2.2 Nanoparticles dispersions analysis

To work with nanoparticles dispersions one of the most important points is the solvent choice. It should be selected based on the features of the porous materials under evaluation. Even more, the dispersing solvent can be use as pure or in a mixture in order to achieve the ideal penetration inside the artefact and the ideal rheological properties for the application purposes [63]. The best methods for paper deacidification are based on the use of non-aqueous solvents, once less polar fluids minimize the risk of ink solubilisation [65]. Moreover, since nanoparticles are stable in alcohols without the need for stabilizers that could leave residues on the treated artefacts, alcoholic hydroxide dispersions can be used for the neutralization of paper acidity, generating an alkaline reserve of carbonate that prevents further degradation, minimizing the risk of swelling and solubilisation of metal-gall inks, which may be lost by using aqueous treatment. Once delivered on the paper the nanoparticles are immediately available for the deacidification or buffering.

In this case, the dispersions were made with non-polar organic solvents namely, cyclohexane or nonane, noticing that, the dispersions were not mixed and were directly sonicated. This ultrasonic treatment promotes the physical absorption of the organic reactant on the nanoparticles´ surface and yields to nanosized units that aggregate further into mass-fractal superstructures. The dispersions analysis is very important to understand how the

modified hydrophobic particles behave in this type of solvents. The ideal dispersions should be stable in a time interval from 18 h to 24 h.

2.3 Turbidimetry

Turbidimetry is the process of measuring the turbidity (or cloudiness) by quantifying the degree of attenuation of a radiant beam which focuses on the particles suspended in a particle/solvent system. This measurement is made in the directly transmitted beam, i.e. upon the loss of intensity of transmitted light due to the scattering effect of particles caused by the finely divided suspended objects.

(i) Equipment and measurements

Figure 2.1 shows the instrumental design generally used on this technique. Here the light passes through a filter creating a light beam of known wavelength that passes through a cuvette containing the dispersion. In this procedure, the decrease in the radiation's transmitted power is measured. If a beam of light is passed through a turbid sample its intensity is reduced by scattering and the quantity of scattered light is dependent upon the concentration and size distribution of the particles [78]. For instrumental measurement it is advisable to ensure that settling of the particles being measured will be negligible [78, 79]. In order to have consistent results variables must be carefully controlled, such as the used wavelength and extremely dilute suspensions may be measured [78].

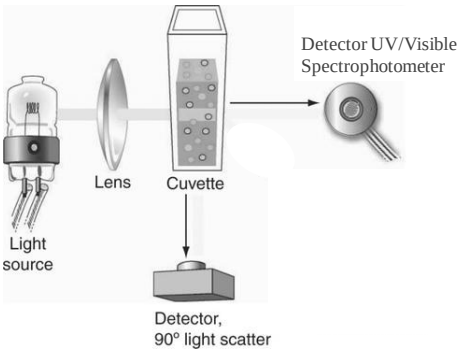

Figure 2.1 – Optical arrangements of turbidimetry [80].

Turbidimetric measurements permit analyze the amount of sediment in a liquid which makes the use of this technique particularly usefully on the assessment of precipitates formed by the interaction of very dilute solutions or other particulate matter [78]. As that turbidimetry is used in order to study the obtained $CaCO_3$ and $Ca(OH)_2$ dispersed particles stability. This technique works as a technical consolidation of the visual analysis, being much more efficient and accurate, as would be expected, since it lowers, in large-scale, the human error.

2.4 Attenuated Total Reflectance

Attenuated total reflectance (ATR) is a sampling technique used in conjunction with infrared (IR) spectroscopy enabling samples to be examined directly in the solid or liquid state, with minimal preparation. This technique, typically performed within a few seconds, allows the obtainment of structural information from the surface and measurement of thin layers (surface characterization) [81, 82].

(i) Equipment and measurements

ATR is based on the phenomenon of total internal reflection and measures the changes that occur in an internally reflected infrared beam that comes into contact with the sample through the ATR crystal (diamond, in this case). When a sample is placed in contact with the diamond the resulting evanescent wave is attenuated in the regions of the IR spectrum where the sample absorbs energy, being the powder directed placed on the sampling plate over the optic window (just enough amount to cover it (mm)) noticing that the sample thickness does not affect the intensity of the absorbance bands and it is in direct contact with the ATR crystal [81, 83, 84]. **Figure 2.2** illustrates the ATR principle.

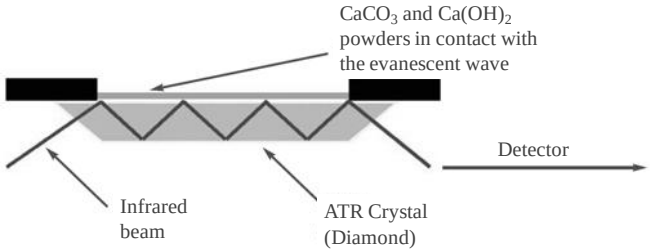

Figure 2.2 – ATR principle. Internal reflections through an ATR crystal.

Due the internal reflectance to the crystal only a fraction of light reaches into the sample. The penetration depth depends on the wavelength, the refractive indices (n) of the ATR crystal and the sample ($n_{\text{ATR crystal}} > n_{\text{sample}}$) and the angle of the entering light beam (typically 45^{o} relative to the crystal surface) [81, 84, 85]. In regions of the IR spectrum where the sample absorbs energy the evanescent wave will be attenuated or altered by the sample and the reflected radiation is returned to the detector.

Diamond is an ideal crystal material for routine measurements on a wide range of samples since it possesses extreme chemical and mechanical robustness and durability and it is chemically inert [81, 82, 84].

ATR provides excellent data quality combined with the highest reproducibility of any IR sampling technique. The improved spectral acquisition and reproducibility associated with this technique leads to better quality database building for more precise material verification

and identification. However, there are some potential drawbacks to using this technique, namely the cost of the optics and ATR element is relatively fragile and should be handled with care [81-85].

In order to study the chemical nature of the $CaCO_3$ (0.0% and 5.0% DA) powders samples were used ATR technique. This procedure provides an important idea about the reaction effectiveness, i.e. it allows analyzing the final product reaction in order to understand what it is constituted by.

2.5 X-ray techniques

X-ray analysis includes two main techniques. X-ray Fluorescence (XRF) spectrometry which is based on the measurement of the characteristic X-ray (XR) emission energies and works on the qualitative and quantitative analysis of elements with high atomic numbers (typically, Z>13). On the other hand X-ray powder Diffraction (XRD) uses diffraction data obtained by the study of structure-dependent scattering phenomena. Here, the shapes and positions of diffraction peaks can be used to establish a wide range of physical properties, namely stress, texture, crystallinity and particle size and phase identification.

2.5.1 X-ray Fluorescence

X-ray Fluorescence (XRF) technique is governed by the photoelectric effect. According to this principle, a high energetic radiation is used to ionize the atoms present in a sample, inducing the ejection of an electron from its atomic position and creating a vacancy on a fully occupied inner shell. In order to the atom revert to its stable state two different processes may occur. In the first case a rearrangement of the atom may occur originating the emission of a second electron (Auger effect). While the second process is based on the transference of an electron from an outer electron to fill the free internal vacancy, emitting a photon and originating the X-ray fluorescence phenomenon (**Figure 2.3**). This process repeat and series of photons will be emitted until a free electron replaces an outermost valence spot so the atom returns to the ground state.

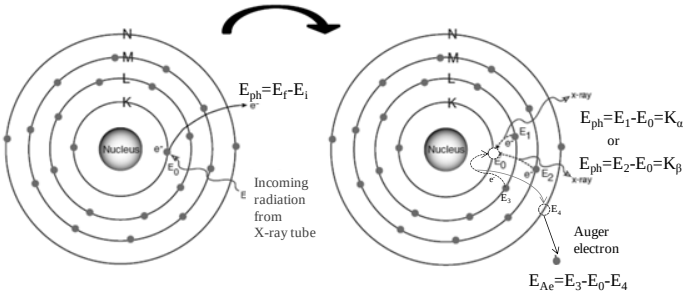

Figure 2.3 – Schematics of X-ray Fluorescence phenomena.

The kinetic energy of the emitted X-ray photon (E_{ph}) depends and corresponds to the energy difference between the shell´s final (E_f) and initial (E_i) binding energies. Because this difference is characteristic for every element the excited atoms emit characteristic radiation (**Figure 2.4**).

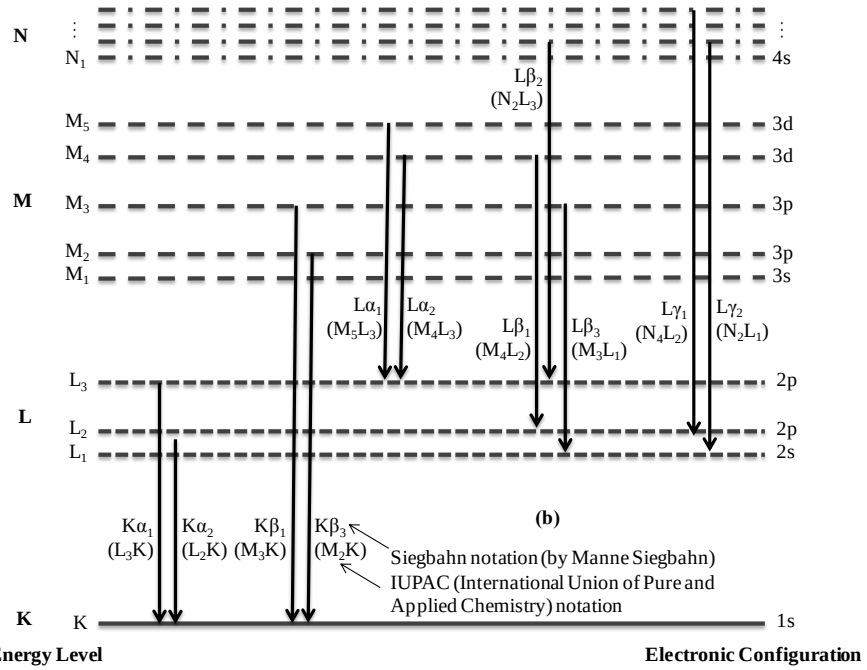

Figure 2.4 – X-ray emission lines, particularly K and L radiation and its respective notations according Siegbahn and IUPAC rules.

Moreover the energy of X-ray lines depends on the atomic number of the emitting atom being this relation translated by the Henry Moseley's law (**Equation 2.1**) [86, 87]:

$$\frac{1}{\lambda} = K(Z - \sigma)^2 \qquad \textbf{Equation 2.1}$$

where λ is the wavelength of the characteristic emission to the atomic number Z and K and σ are constants values specific for the energy distribution levels and sublevels involved in a given transition. Note that K lines are generally more intense.

The energy of Auger electrons (E_{Ae}) depend on the energy difference between the vacancy and the jumping level but also on the binding energy of the emitted electron. Both processes (emissions of X-ray photons and Auger electrons) are competing. As that their probability is complementary and the chance of Auger effect occur increases with a decrease in the difference between the energy states (highest for low Z elements) [86, 88].

It is important to notice that X-rays have different interactions with the material, namely absorption and scattering.

Absorption occurs when the incoming radiation is absorbed in the sample and has to be considered as two different interactions. The first one is described by the Lambert-Beer law (**Figure 2.5** and **Equation 2.2**) where I_0 is the incident radiation and I is the transmitted one, noticing that the intensity is reduced by exponential function in dependence of mass absorption coefficient μ, thickness of the layer d and density ρ on the sample [86, 89]. And secondly as the absorption of fluorescence radiation on the way to the sample surface, which describes the information depth of XRF and heat up the sample.

$$I = I_0 \exp^{-\mu d \rho} \quad \textbf{Equation 2.2}$$

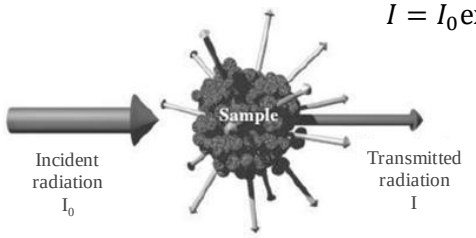

Figure 2.5 – Absorption and dissipation (in all angles) of electromagnetic radiation.

On the other hand, scattering results from the interaction of X-ray photons with the electrons of the target element, changing their direction and possibly loosing energy. Two main types of scattering take place in the photon-atom interaction: Compton (incoherent or inelastic) and Rayleigh (coherent or elastic) scattering. On Compton effect (**Figure 2.6 (a)**) the incoming photon is scattered on a weakly bonded electron that can take over a part its energy being the radiation characterized by a slightly lower energy compared to that from the incoming beam. In case of Rayleigh effect (**Figure 2.6 (b)**) no energy is lost in the collision process once it is a result of photons scattering on strongly bonded electrons. These electrons can only oscillate with the frequency of the incident photon. As no energy change is involved the Rayleigh radiation will retain exactly the same energy as the incident beam.

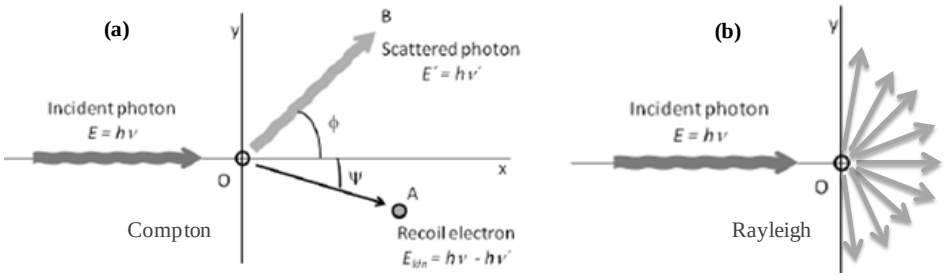

Figure 2.6 – Compton **(a)** and Rayleigh **(b)** scattering effects.

Because of these phenomena, in addition to the characteristic radiation of the elements present in the irradiated sample, the XRF spectrum presents peaks that correspond to a Compton and Rayleigh scatters of the incident beam. Even more, Rayleigh scatter peaks are

characterized by sharp shapes that correspond to the characteristic energies of the incident beam while Compton peaks are wider and located at slightly lower energies. Intensity of scattered is dependent on the average atomic number and on the density and the thickness of the sample being irradiated, as consequence light elements give rise to high Compton effects and low Rayleigh scatter [87, 90].

Due to its versatility XRF technique is widely used in chemistry, biology, forensic science, engineering, agriculture, clinical chemistry, cultural heritage and many other fields [89]. Some of its benefits and drawbacks are related with a low spectral background caused by scattered tube radiation and the relatively simple instrumentation; and the low spatial resolution originated by the impossibility for focusing the X-rays [86].

Normally, XRF measurements are referred to bulk analysis [90]. However the two main points to consider in relation with the penetration depth are the depth of penetration of the primary X-ray beam into the sample and the escape depth from which fluorescent X-rays can be detected. Both of these are directly linked to the energy of the X-rays: the higher the X-ray energy the deeper the X-ray penetrates. Moreover, X-rays penetration depth can vary from micrometers down to several millimetres, depending on the sample matrix [91].

The lighter elements (e.g. Al, Si) have very low energy X-rays and thus will be difficult to detect even at relatively small depths within the sample. Heavier elements (e.g. Cu, Ag) have much more energetic X-rays which will be able to pass through large distances within the sample. So, heavy elements (i.e. energetic fluorescent XR) will be detectable relatively deep within a sample matrix primarily comprised of light elements (i.e. low absorption) and light elements will be detectable only at the surface of a sample matrix comprised of heavy elements [91].

(i) Equipment

In the present study a micro Energy Dispersive X-ray Fluorescence (μ-EDXRF) spectrometer is used. This is an analytical method with sensitive elemental analysis of (non)homogeneous material that focus the incident radiation (by introducing appropriate focusing optics) to a much smaller size spot (μm/nm scale) on the sample [86, 87]. The equipment consists in two basic units: the excitation source and the spectrometer detection system. Here the detector can be very close to the sample so a high amount of fluorescence radiation can be captured [86]. The sample chamber operates under vacuum, which is a crucial condition in the determination of light elements.

Detector

Detectors transform the emerging energy of the X-ray photons into electric pulses (counts) detecting both fluorescence radiation and scattering. A Silicon-Drift-Detector (SDD) is used in the present work. SDD are developed with a cylindrically symmetric structure that generates the electrical field for charge carrier collection, guiding the electrons through the detector and reducing the entrance capacity for the preamplifier, dropping the electronic noise in the detector and, consequently, reducing the filter which means that count rates can be enhanced guarantying very high count rates and good energy resolutions [86-88]. It is made in highly pure silicon with a very low leakage current [87].

At this point it is important to define some main criteria for the detection system (detector plus amplifier and multichannel analyzer) evaluation. Resolution is the ability of the detector to distinguish between different photons with very close energies. It influences the selectivity of the methodology and is estimated by the Full Width at Half Maximum (FWHM) [87, 88]. The detector efficiency is defined as the percentage of ionizing radiation reaching the detector (higher number of pulses, higher number of incoming photons, higher efficiency). It depends on the detector size and shape, the distance from it to the sample, the absorption of radiation before it reaches the detector and the backscatter radiation toward it [87]. Finally, sensitivity corresponds to the capability to produce a usable pulse for a given type of radiation and energy. This parameter depends on the detector cross-section and its volume, the detector window and the intrinsic detector noise [88].

Additional peaks (spectrum artifacts) can arise in an XRF spectrum from sources other than the meaningful elements in the sample and due the photoelectric events that occur deep inside the detector. It is important to be aware of the nature of these events in order to get quality analytical results once they contribute to the full energy peak [87, 88]. For events which occur near the surface, there is a significant probability that the characteristic X-ray escapes and the corresponding amount of energy is lost from the signal. The atoms in a detector (Si, in this work) will also emit their own characteristic radiation when struck by the incoming X-ray beam. The majority of this radiation is immediately absorbed within the detector and not contributes to the overall charge collected [87]. The result of this escape process is an escape peak located at an energy value lower than the parent peak and equivalent to the difference between the energy of the original photon and the energy of the line of the detector element [87, 88]. These artifacts could be reduced by preventing the incident radiation from interacting in the periphery of the detector by means of collimation [88]. Other common spectral artifacts are sum peaks. They are the result of the high-intensity

peaks that arrive to the detector so close together in time that the pileup inspector cannot recognize them as two events; therefore the energy of the resulting peak is the sum of the two initial energies and it effect is for the signals to be seen as only one [87, 88]. Finally, background artifact, which is mainly due to coherent and incoherent scattering, already exposed. It shape can be complex and depends on the initial shape of the excitation spectrum and on the sample composition as well as on the incomplete charge collection of intense fluorescence lines in the spectrum [88]. **Figure 2.7** presents some spectrum artifacts detected on the present work, namely the copper escape peak, the Compton effect, as well as the characteristic signals from the equipment (Zr) and X-ray tube (Rayleigh scatter-Rh).

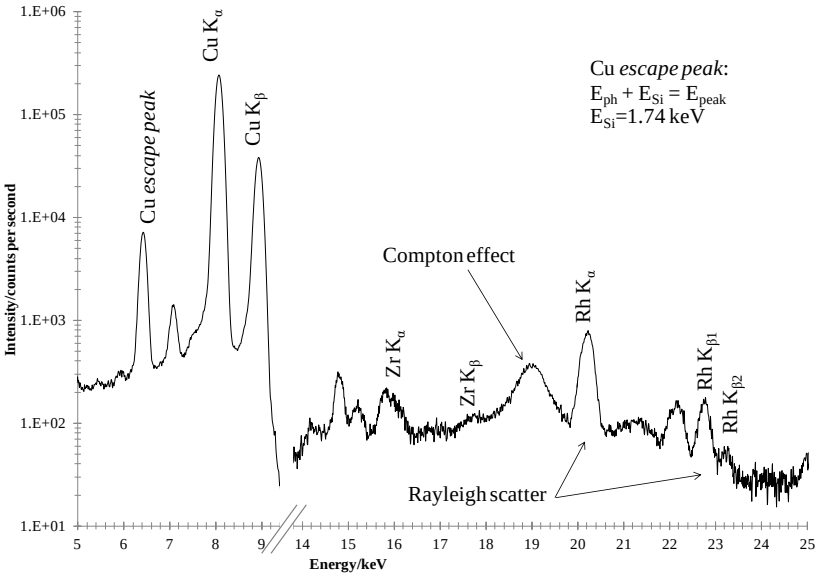

Figure 2.7 – Spectrum artifacts and characteristic signals from the used equipment.

X-ray tube

In a X-ray tube a beam of emitted electrons, generated by heating up the spiral filament (cathode), are accelerated by a strong electric field against a target (anode) placed inside a vacuum housing [86-88]. The energy of the characteristic radiation of the XR tube is determined by the element from which the anode is made, while the continuous radiation depends on the applied voltage, the current and on the anode material used [87]. This process generates high energetic electromagnetic radiation: X-rays.

X-ray tube windows are normally made of beryllium (Be) because of its high transmission for low energy XR, however Be is a poor conductor so if a window is too thin it can lead to fracture [88]. Even more, in a side-window tube the electrons hit the target with an angle that is different to 90º and the distance from target to window has to be relatively large to avoid the heating of the window [86, 88].

Optics

Concerning cultural heritage related objects X-ray optics devices are a great improvement as it resolves tiny details both lateral and in depth [90]. With these devices it should be possible to change the direction and/or the energetic distribution of the radiation [86]. However, its application is limited when elements with very low concentrations present in a sample have to be determined [87].

The use of capillary lens shape and direct the primary X-ray beam that impinges on the lens´ surface and propagates thorough the system, emerging in a convergent beam with high intensity [87]. Particularly, polycapillary systems, prepared from bundles of very thin single capillaries (inner diameter of 1–2 μm), are used in order to obtain a larger intensity gain within the focal spot [86, 87].

(ii) Qualitative and quantitative analysis

Spectra resulting from this technique allow analytical information about the sample in order to ascertain the elements present in the target sample (qualitative analysis) and/or their content quantification (quantitative analysis).

The position of the characteristic X-ray emitted energies on the spectrum determines the elements present in the sample. In order to get meaningful and qualitative quality analytical results it is important to take into account all the spectrum characteristics and artifacts [87].

Quantitative XRF analysis takes into account the heights of the peaks once they are related to the element concentrations. This evaluation involves both the conversion of the net analytical signs to the analytes concentrations as well as the elements peaks correction for the spectral background and possible overlaps by background correction and deconvolution, respectively. Quantitative analysis when using μ-EDXRF generates relatively large errors. As that these results should be considered as semi-quantitative. The resulting information about the elements content in the sample is relative and indicative, so extra care is important for the data treatment.

Statistical treatment on the analytical results is necessary since the heterogeneities and the modifications of the corrosive conditions can led to variation in the composition of the corrosion products. This topic will be further discussed on **Chapter 4**.

(iii) Measurements

μ-EDXRF is used in order to investigate the coins elemental constitution semi-quantifying the elements that constitute its surface and bulk. Based on historical information the possibility of the studied coins had been silver enriched need to be

investigated. As that is important to notice that regardless the origin of silver enrichment, the enriched layer plays a decisive role in the μ-EDXRF analysis results. If the thickness of enriched layers is greater than the depth under study only the composition of this layer is accessible [33]. Moreover, when the surface silver content is several times higher with respect to the amount of the bulk, this result suggests that the coin had been intentionally silver surface enriched. Even though, the major problem in analysing antique plated coins is whether it is possible to indisputably distinguish intentional silvering from the phenomenon of surface enrichment resulting from long-term selective corrosion.

2.5.2 X-ray Diffraction

A crystal can be defined as a homogeneous and anisotropic body, having the natural shape of a polyhedron and where a typical 3D regular arrangement of atoms represented by the smallest repeating unit showing the full symmetry of the crystal structure (unit cell) can be seen. Lattice planes are defined from shape and dimensions of the unit cell. These planes are imaginary and provide a reference grid to which the atoms in the crystal structure may be referred [92, 93].

X-ray Diffraction (XRD) analysis is a versatile technique for examining, identify and characterize almost any crystalline material, whether inorganic or organic through the use of X-rays [92, 94]. Since every ordered material is made up of a unique arrangement and number of atoms it will give a diffraction pattern that is, to all intents and purposes, also unique [92]. This fact introduces the concept of finger printing on X-ray Diffraction analysis, one of the most important ones on the identification of unknown materials.

The operative equation in XRD is the Bragg equation (**Equation 2.3**):

$$n\lambda = 2d\ sen\theta \qquad \textbf{Equation 2.3}$$

where n is the order of a reflection, λ the wavelength, d the distance between parallel lattice planes and θ the angle between the incident beam and the lattice plane, known as the Bragg angle. $2d\ sen\theta$ represents the path length in the crystal. When its value is a multiple of the wavelength constructive interference occurs and diffracted intensity is obtained [94]. Bragg´s Law is represented in **Figure 2.8**.

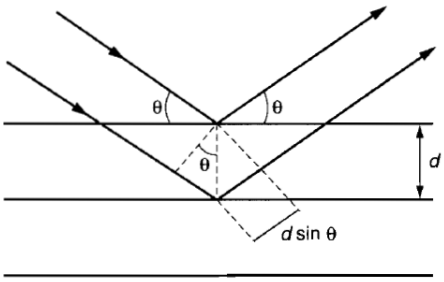

Figure 2.8 – Illustration of Bragg´s Law [94].

The two basic parameters being used in this search/match process are the *d* values, calculated from the measured 2θ values in the diffractogram, and the relative intensities of the lines in the pattern. *d*-spacing is a function of the lattice parameters (*a,b,c*) and angles (α,β,γ) that define the unit cell; and the Miller indices (*h,k,l*) denoting a particular reflection. Each family plans is separated by a specific *d* gap whose value allows identifying a particular and unique plan, so the main structure has a characteristic set of interplanar distances *d*. As such, it is the geometry of the crystal lattice that determines the positions of the peaks in its diffraction pattern. In general, the more symmetrical the material, the fewer peaks in its diffraction pattern [94]. X-ray diffraction is thus capable of providing general purpose qualitative and quantitative information on the presence of phases (e.g., compounds) in an unknown mixture [92].

(i) Equipment and measurements

Powder diffractometer systems have a geometric arrangement (**Figure 2.9**) known as the Bragg–Brentano parafocusing system and is typified by a diverging beam from a line source F (X-ray source), falling onto the specimen S, which is diffracted and passes through a receiving slit R, to the detector, passing along a two-circle goniometer (A). Distances FA and AR are equal. The amount of divergence is determined by the effective focal width of the source and the aperture of the divergence slit D. The equipment control and data collect and analysis are made on a computer [92, 94].

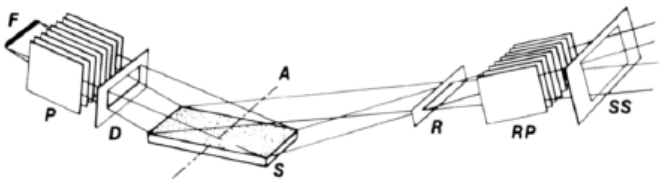

Figure 2.9 – Geometry of the Bragg–Brentano diffractometer [92].

Legend: F-source; P and PR-Soller slits; S-sample; D- divergence slit; R- receiving slit. The axis of the goniometer is at A.

By synchronizing the scanning speed of the goniometer with the recorder diffractogram (a plot of 2θ intensity *vs* degrees) is obtained. The goniometer can be used in two different configurations: $\theta/2\theta$ (sample stage *vs* detector) or θ/θ (tube *vs* detector). Moreover, this device may be oriented to keep the sample horizontal or vertical [94]. A diffracted beam monochromator may also be used in order to improve signal-to-noise characteristics. Finally, in Crooks tube a tungsten wire exerts pressure on the poles increasing the pressure between the cathode and the anode and releasing a cathode ray beam that collides with the metal target.

A large data base (either computed or in paper) of pure single-phase materials is normally available so that rapid empirical file-searching techniques can be employed for measuring phases (compounds) [92, 94]. The diffractogram is reduced to a list of *d*-spacing's and intensity values and then submitted for file search/matching [92].

With relation to the set of studied coins this technique is used in order to identify crystalline unknown compounds. In this case, the work is particularly complex and prolonged due to the lack of information about the patina constituents' compounds. Even more, being completed unknown the coins origin. The application of this technique to 0.0% and 5.0% DA $CaCO_3$ powders works in the opposite way. XRD is used, on this case, in order to examine the components crystal structure allowing identifying the presence of crystalline compounds and their phases. Here XRD is used to confirm the already known compounds that are present in the powders.

2.6 Scanning Electron Microscopy / Energy Dispersive X-ray Spectroscopy

The Scanning Electron Microscopy (SEM) sweeps the solid surface, according to the operator command, with a focused high energy electron beam that interacts with atoms on the sample surface producing various signals that can be detected and which are translated into 2D images of the object showing its spatial properties variations [95]. The signals that derive from electron-sample interactions reveal information about the morphology (texture and topographical) and chemical composition (in microanalysis detail) [96, 97] of the object. This approach is especially useful in qualitatively or semi-quantitatively analyses. Even more, SEM technique reveals levels of detail and complexity inaccessible by light microscopy and it creates precise measurements of very small features and objects down to 50 nm [96, 97].

SEM is routinely used to generate high-resolution images of shapes on objects and to show spatial variations in chemical compositions acquiring elemental maps or spot chemical analyses when coupled with Energy Dispersive X-ray Spectroscopy (EDS).

(i) Equipment and measurements

Figure 2.10 shows the SEM inside structure. It comprises an electron generating component (gun) fitted, generally, with a tungsten filament cathode at the top; a column down which the electron beam travels; a series of lenses to shape the electron beam; the sample chamber at the base; a series of pumps to keep the system under vacuum; a computer that drives the microscope, with the additional bench controls; and an ancillary equipment to, for example, composition analyses [97]. This device runs on all axes allowing analyzing the sample in any perspective [95]. Note that EDS detectors cannot detect very light elements (e.g. H or Li).

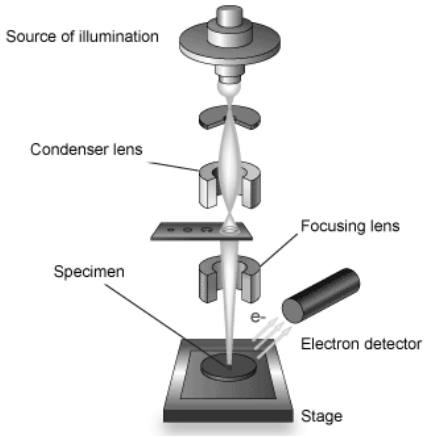

Figure 2.10 – Schematic figure on Scanning Electron Microscopy [98].

Sample preparation can be minimal depending on the nature of the samples and the data required. However, the objects must be solid, fit into the microscope chamber and stable in a vacuum.

This technique is used on both surface samples, i.e. for the evaluation on the conservation state of the antique Portuguese *dinheiros* as well as in the nanoparticles´ characterization for cultural heritage conservation, in the same way. On coins, the SEM/EDS is applied in order to study their corroded surface allowing to evaluate the degradation phenomena extent and punctually quantifying the elemental composition in several specific spots. In the 0.0% and 5.0% DA $CaCO_3$ synthesized powders the goal is to analyze their surfaces, identifying the morphology changes and realize the size (nano or not) of the particles.

PART I

EVALUATION ON THE DEGRADATION STATE OF ANTIQUE COINS BY SPECTROSCOPIC TECHNIQUES

3 EXPERIMENTAL PART

A set of six *dinheiros* dated from the first Portuguese dynasty (13rd and 14th centuries) were chosen to be analyzed by means of μ-EDXRF, XRD and SEM/EDS.

3.1 Coins visual analysis: a macro scale morphologic approach

From the historical point of view coins are classified in different series based on their numismatic characteristics. **Table 4.1** presents the set of the studied *dinheiros*. In order to simplify the data analysis, notation composed by the coin catalogue number followed by the letters O (obverse) and R (reverse) when both faces need to be discriminated was used.

3.2 μ-Energy Dispersive X-ray Fluorescence

In order to proceed the X-ray Fluorescence elemental measurements a high performance micro-Energy Dispersive X ray Fluorescence (μ-EDXRF) spectrometer M4 Tornado from Bruker was used. The X-ray tube is a micro-focus side window Rh tube powered by a low power high voltage generator and cooled by air. A polycapillary is used to obtain a spot size down to 25 μm for Mo-K_α. The X-ray generator was operated at 50 kV and 600 μA and a composition of filters was used to reduce background (100 μm Al/ 50 μm Ti/ 25 μm Cu). Detection of fluorescence radiation is performed by energy dispersive Silicon-Drift-Detector with 30 mm² sensitive area and energy resolution of 142 eV for Mn-K_α. Measurements were carried out under 20 mbar vacuum conditions and performed directly on the samples. Spectra deconvolution, fitting and quantification were performed using the in-built ESPIRIT software.

The Limits of Detection were calculated by the use of the Certificate Reference Material (CRM) 32X SN7 (batch A) (MBH Analytical Ltd). A disc ~40 mm diameter in bronze (chill cast) manufactured by Polycast Ltd. The spectra deconvolution and fitting were performed using WinAXIL software package.

3.3 X-ray Diffraction

Powder X-ray Diffraction (XRD) was used in order to characterize the nature of the patina films on the coins surface. The procedure was carried out with a Panalytical X'pert Pro diffractometer ($\theta/2\theta$) equipped with X'Celerator detector and with automatic data acquisition (X'Pert Data Collector (v2.0b) software). The patterns were collected using unfiltered Cu-K_α radiation, 40 kV–30 mA, and the Bragg−Brentano geometry over the 2θ range 10−90° with a 2θ-step size of 0.017º and a scan step time of 20 s. The structural characterization of the

samples was made according JCPDS/ICCD (Joint Committee on Powder Diffraction Standard Data/International Centre for Diffraction Data) database.

3.4 Scanning Electron Microscopy / Energy Dispersive X-ray Spectroscopy

The morphology and elemental composition were investigated by Field Emission Gun Scanning Electron Microscopy (FEG SEM) JEOL 7001F coupled to Oxford light elements EDS detector and EBSD detector. For the collection of micrographs the electron gun was operated at 25 kV accelerating voltage.

4 RESULTS PRESENTATION AND DISCUSSION

In order to proceed the evaluation on the conservation state and the determination of the patina constituents and propose a possibly corrosion mechanism in the system alloy/interface several techniques were used, namely μ-EDXRF, XRD and SEM/EDS. The present chapter presents a complete discussion of the obtained results.

4.1 Coins visual analysis: a macro scale morphologic approach

The examination on the surface of the coins helps understanding the composition of the substrate and its patina compounds. However it does not allows to assume their composition but, on a general point of view, could be an useful criteria in order to be aware of the coin history.

The general appearance of the coins and the main observations on each face is described on **Table 4.1**.

It could be concluded that all the coins were well preserved taking into account their dating period (13rd and 14th centuries). The only exceptions were on 257 R, 283 R and 500 R, particularly, 275 R which presents a typical and local "cauliflower" corrosion area.

Generally, well defined surfaces with black-brownish coloration were observed in all the coins. Moreover, coins numbered 280, 257 and 283 showed a copper like coloration on some high relief areas.

A yellow-brownish colour on low relief areas was observed on 275, 279, 280 and 500 coins. A locally green coloration on 279 coin (low relief region) and a red-brownish colour on 257 (covering the surface) has been observed.

Table 4.1 - Observations on the macro scale general appearance on the studied set of *dinheiros*.

Legend: cn – catalogue number.

cn	Obverse	Observations	Reverse	Observations
275	 **275 O**	Well defined surface with a black-brownish coloration. Yellow-brownish colour on low relief areas.	 **275 R**	Well defined surface with a black-brownish coloration. Yellow-brownish colour on low relief areas. Local "cauliflower" corrosion.
279	 **279 O**	Well defined surface with a black-brownish coloration. Yellow-brownish colour on low relief areas. Locally green coloration on the low relief areas around the central figure.	 **279 R**	Well defined surface with a black-brownish coloration. Yellow-brownish colour on low relief areas. Locally green coloration on low relief areas near the coin centre.
280	 **280 O**	Well defined surface with a black-brownish coloration. Yellow-brownish coloration on low relief areas. Locally copper coloration near the coin edges on high relief areas.	 **280 R**	Well defined surface with a black-brownish coloration. Yellow-brownish coloration on low relief areas.

cn	Obverse	Observations	Reverse	Observations
257	 257 O	Well defined surface with a copper like coloration on the coin centre and a black-brownish colour near the coin edges. Locally some corroded areas near the coin edges presenting a red-brownish coloration	 257 R	Corroded areas mainly near the coin edges. Red-brownish coloration in part of the coin surface.
283	 283 O	Well defined centre. Black-brownish coloration in the low relief areas and cooper like coloration on some high relief areas. Imperceptible coinage on the edges.	 283 R	Poorly defined surface with a black-brownish coloration on low relief areas. Cooper like coloration on some high relief areas.
500	 500 O	Well defined surface with a black-brownish coloration. Yellow-brownish coloration on low relief areas.	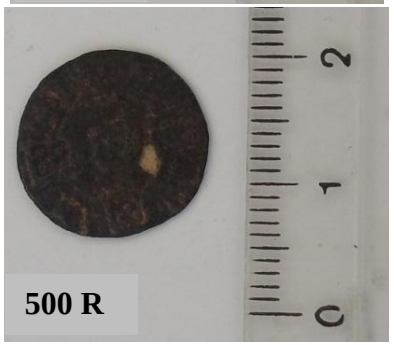 500 R	Poorly defined surface. Imperceptible coinage on the edges. Black-brownish colour all over the surface. Visibly yellow-brownish dirty.

The macro scale morphologic characterization on the studied set of *dinheiros* is presented on **Table 4.2**.

Table 4.2 – Macro scale morphologic characteristics on the studied set of *dinheiros*.

			Dinheiros			
Catalogue Number	**Kingdom**	**Date**	**Maximum Diameter/mm**	**Minimum Diameter/mm**	**Thickness /mm**	**Weight/g**
275	D. Sancho II	1223-1248	16.8	14.8	0.8	0.8
279	D. Afonso III	1248-1279	17.6	16.0	0.6	0.7
280	D. Dinis	1279-1325	16.2	15.1	1.1	1.0
257	D. Pedro I	1357-1367	17.2	16.2	0.5	0.6
283	D. Fernando I	1367-1383	15.4	14.7	0.6	0.6
500	D. Fernando I	1367-1383	14.2	14.1	0.9	1.0

Based on this data it can be concluded that the numisms have similar diameters and slightly different weights.

4.2 µ-Energy Dispersive X-ray Fluorescence

Micro Energy Dispersive X-ray Fluorescence (µ-EDXRF) spectrometry was used in order to investigate the elemental composition on the coins (bulk and surface).

It is important to highlight some ideas before presenting the results. The beam penetration depth is dependent on the sample matrix – heavier elements have more energetic X-rays, which will be able to pass through large distances within the sample and hence can be produced deeper inside the bulk. On the other hand, if a coin has a very thick patina layer the incident radiation has to cross this coating before the bulk. In any case, elements Z>13, such as carbon and oxygen, are undetectable by XRF technique.

Figure 4.1 presents the obtained results (element identification and copper quantification) when two points on the same coin, particularly 283 coin, where compared. The point's choice was based on its visual similar characteristics, i.e. the position on the coin, high relief and presented colours (both identified by the white circles on the figure).

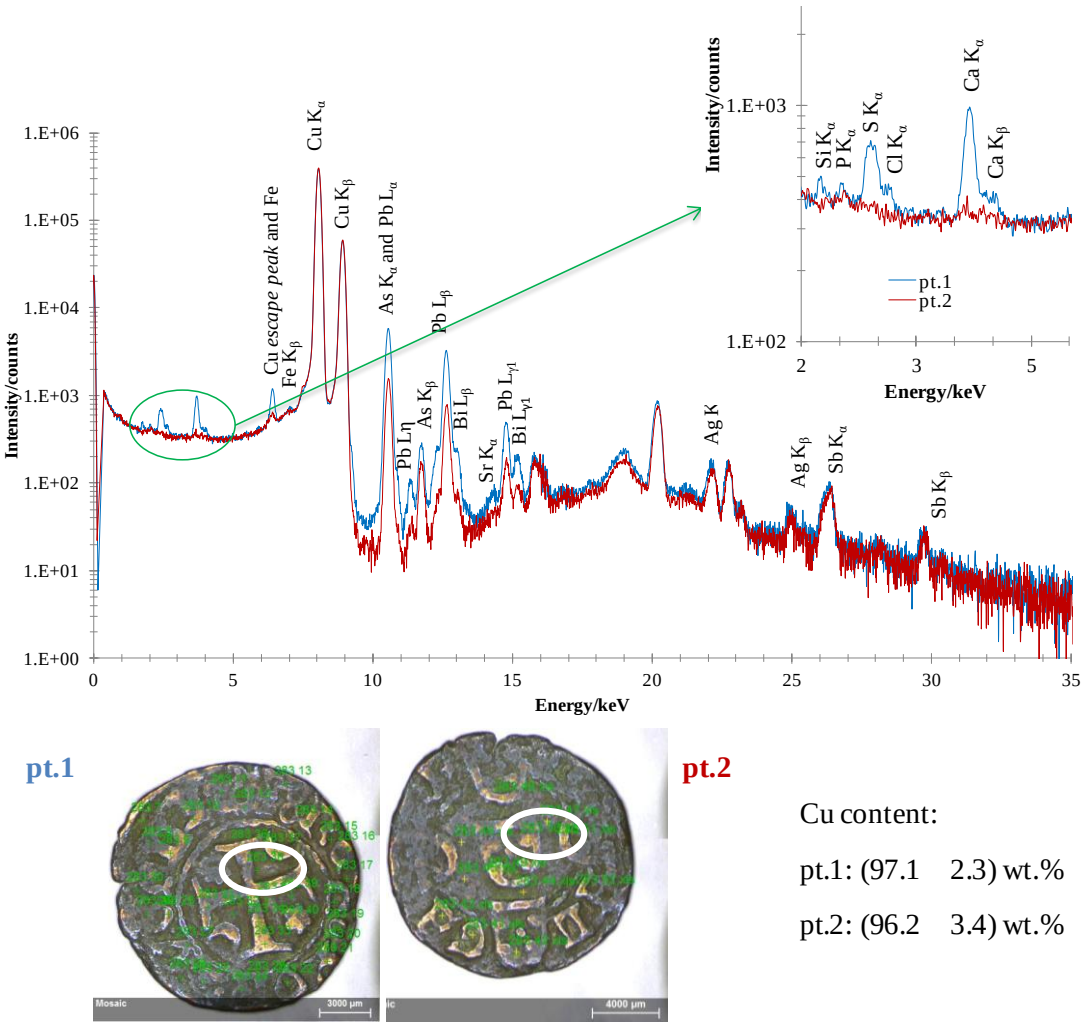

Figure 4.1 – µ-EDXRF spectra and images obtained on 283 coin for pt.1 (blue line) and pt.2 (red line). Copper quantification on both points.

Based on these results it can be concluded that iron (Fe), arsenic (As), lead (Pb), bismuth (Bi), silver (Ag), antimony (Sb) and copper (Cu) were identified on both spectra. Furthermore, the similarity on the copper content on both points (Cu > 96 wt.%) is clear.

In fact, the main differences between both spectra were the peaks significance for the light elements, such as silicon (Si), phosphorus (P), sulphur (S), chlorine (Cl), calcium (Ca) and strontium (Sr). These variations are particularly important since it allows to demonstrate the differences between the presence, or not, of exogenous elements on the analysis. Si, P, S, Cl, Ca and Sr were present on the coin surface due environmental contamination or as corrosion products, being part of the patina layer and not as constituents of the alloy. This topic will be further discussed. In consequence, it can be assumed that pt.2 (red line) should be mostly representative of the alloy once the presence of these contaminants is lower, regarding the obtained spectra.

These results represent the main criterion chosen for the following discussion. As consequence of the proved existence of these "contaminants" on the coin surface, the spectra representing the remaining studied coins were chosen based on its elemental quantifications in order to reduce, as much as possible, the presence of elements such as Si, P, S, Cl, Ca or Sr. This choice allowed to present, in the best way possible, the bulk constitutions.

The obtained quantifications should be taken carefully, as previously exposed. Parameters such as the standard deviation and the relative standard deviation (RSD) as well as the Limit of Detection (LOD) are very important is the method and results evaluation. **Annexe II** presents the detailed information and formulas in order to accomplish the data treatment according to the literature [87, 99-102].

4.2.1 Limit of Detection

The signal at the Limit of Detection (LOD) is derived from the smallest measure that can be detected with reasonable certainty for a given analytical procedure. The value of LOD, for µ-EDXRF is given by the **Equation 4.1 [**87, 99]:

$$LOD = \frac{3c_i\sqrt{N_b}}{N_p} \qquad \textbf{Equation 4.1}$$

where c_i is the concentration of the element i and N_b and N_p are the counting rates for the background and for the peak, respectively.

In practice, the limit of detection represents the level below which cannot be confident whether or not the element is actually present. It follows from this that no analytical method can ever conclusively prove that a particular chemical substance is not present in a sample, only whether it cannot be detected [100]. LOD is better when the background is less, the instrumental sensitivity increases, and through longer counting times **[**87].

Table 4.3 presents the calculated LOD´s by the measure of the CRM 32X SN7.

Table 4.3 – LOD values obtained by µ-EDXRF on CRM 32X SN7 (wt.%).

	Cu	**As**	**Ag**	**Sb**	**Pb**	**Bi**	**Sn**	**Zn**	**Co**	**Ni**
LOD	$1.0x10^{-2}$	$2.9x10^{-3}$	$2.2x10^{-2}$	$3.3x10^{-2}$	$5.5x10^{-3}$	$4.1x10^{-3}$	$3.3x10^{-2}$	$5.7x10^{-3}$	$5.5x10^{-3}$	$8.2x10^{-3}$
U(LOD)[a)b)]	± $1.8x10^{-5}$	± $1.6x10^{-4}$	± $1.5x10^{-3}$	± $3.8x10^{-3}$	± $3.0x10^{-4}$	± $5.2x10^{-4}$	± $5.9x10^{-4}$	± $1.2x10^{-4}$	± $2.0x10^{-4}$	± $3.2x10^{-4}$

[a)] k = 2,for a confidence level of, approximately, 95%.

[b)] the relative uncertainty of N_p was neglected in the combined uncertainty calculation.

4.2.2 Coins analysis

Since the elemental quantification on each point varies with the number of elements detected and selected on each spectrum, the final error on the results takes this into account. On practice, these errors can be minimized by reporting the mean value of the quantifications however they can be assumed only as representative of the total content of each element.

The individual µ-EDXRF spectra and elemental quantification for each one of the studied *dinheiros* are present on **Figures A.III.1** to **A.III.6** and **Tables A.III.1** to **A.III.6** on **Annexe A.III.1**. The complete chemical composition of the patina layer and of the bulk metal of the samples and the respective statistical treatment is presented on **Table A.III.7** on the same Annexe.

Several elements were identified and quantified as constituents of the studied *dinheiros*, being part of its billon alloy or as patina constituents. The obtained results showed that copper was the main component in the all of them, followed by silver and some minor elements, namely Si (non-detected only on sample 257), Fe, Pb, Sb, As, Ca, P, Cl, S and K (all with contents > 0.11 wt.%), bismuth (Bi), gold (Au), mercury (Hg), titanium (Ti) and Sr (contents < 0.09 wt.%) when detected. However Ag is a particularly case of study.

Table 4.4 presents a resume on the copper and silver contents. These are the main elements under study once, historically, the set coins should be made on billon alloy – copper/silver.

Table 4.4 – Copper and silver contents (wt.%) on the studied set of *dinheiros*.

Coin	Kingdom	Element quantification (wt.%)	
		Cu	Ag
275	D. Sancho II	86.7 ± 1.8	8.1 ± 1.3
279	D. Afonso III	88.2 ± 3.0	8.7 ± 1.1
280	D. Dinis	85.3 ± 4.3	9.2 ± 1.7
257	D. Pedro I	89.6 ± 1.5	9.3 ± 1.4
283	D. Fernando I	97.1 ± 2.3	0.248 ± 0.078
500	D. Fernando I	95.7 ± 6.3	0.242 ± 0.048

In order to facilitate these relationships the graphs below were made (**Figure 4.2**):

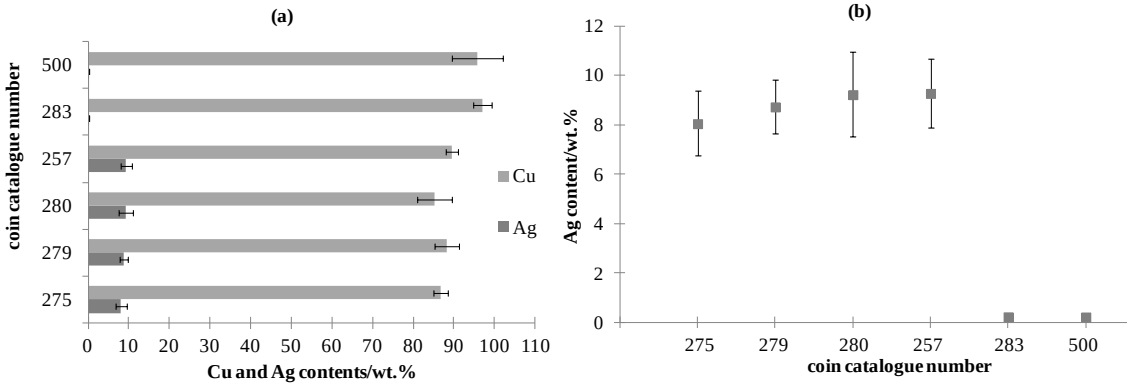

Figure 4.2 –Copper and silver contents (wt.%) **(a)** and silver contents (wt.%) **(b)** variations on the studied set of *dinheiros*.

Based on these data it can be concluded that copper content was practically invariable (always Cu > 81.0 wt.%). On the other hand, the silver content had a different behaviour. As a result two different groups of coins, regarding this element quantification could be established: the first group (G1) constituted by coins with the catalogue numbers 275, 279, 280 and 257, with high contents of Ag varying from 11.0 wt.% to 7.0 wt.%; and a second one (G2) which the coins numbered 283 and 500 (dated from D. Fernando I reign) belonged. G2 presented a silver content that varied between 0.3 wt.% to 0.1 wt.%.

According to these results it can be assigned that even though G1 and G2 were constituted by a similar billon alloy, the coins from D. Fernando I period of reign were weakened. These results are in accordance with the historical information at that date. The economical situation of the country was well demonstrated by the fact that the silver content between 0.24 wt.% and 0.25 wt.% did not corresponded to the legal one: 2.78 wt.% [12]. These coins are composed by a billon alloy with a low content in silver.

The presented results were compared with the ones obtained by Guerra *et al*. [12]. These authors concluded that during the first dynasty, the average fineness corresponds to the legal one from D. Afonso Henriques to D. Pedro I. However, for D. Fernando I they registered exactly the same behaviour. **Table 4.5** compares the legal values and the results from Guerra *et al.* [12] with the data collected in the present work.

Table 4.5 – Comparison between the silver contents in literature (legal content and the results from Guerra *et al.* [12]) and the results obtained in the present analysis for the coins dated from D. Afonso III, D. Dinis, D. Pedro I and D. Fernando I.

Coin	Kingdom	Legal content [12]	Guerra *et al.* [12]	Observed
279	D. Afonso III	8.33	8.13 ± 1.14	8.75 ± 1.10
280	D. Dinis	8.33	8.11 ± 1.05	9.24 ± 1.73
257	D. Pedro I	8.33	8.57 ± 0.06	9.29 ± 1.38
283	D. Fernando I	2.78	0.17 ± 0.06	0.25 ± 0.08
500				0.24 ± 0.05

In most cases, with time, the devaluation of the alloy corresponded to the replacement of the noble metal by a less expensive one [12].

Figures 4.3 and **4.4** present the stacked µ-EDXRF spectra for the studied set of *dinheiros* according to the groups that they represent. **Figure 4.3** shows G1 composed by 275, 279, 280 and 257 coins) results and **4.4** represents G2 constituted by coins numbers 283 and 500). In both cases the principal peak identification can be seen.

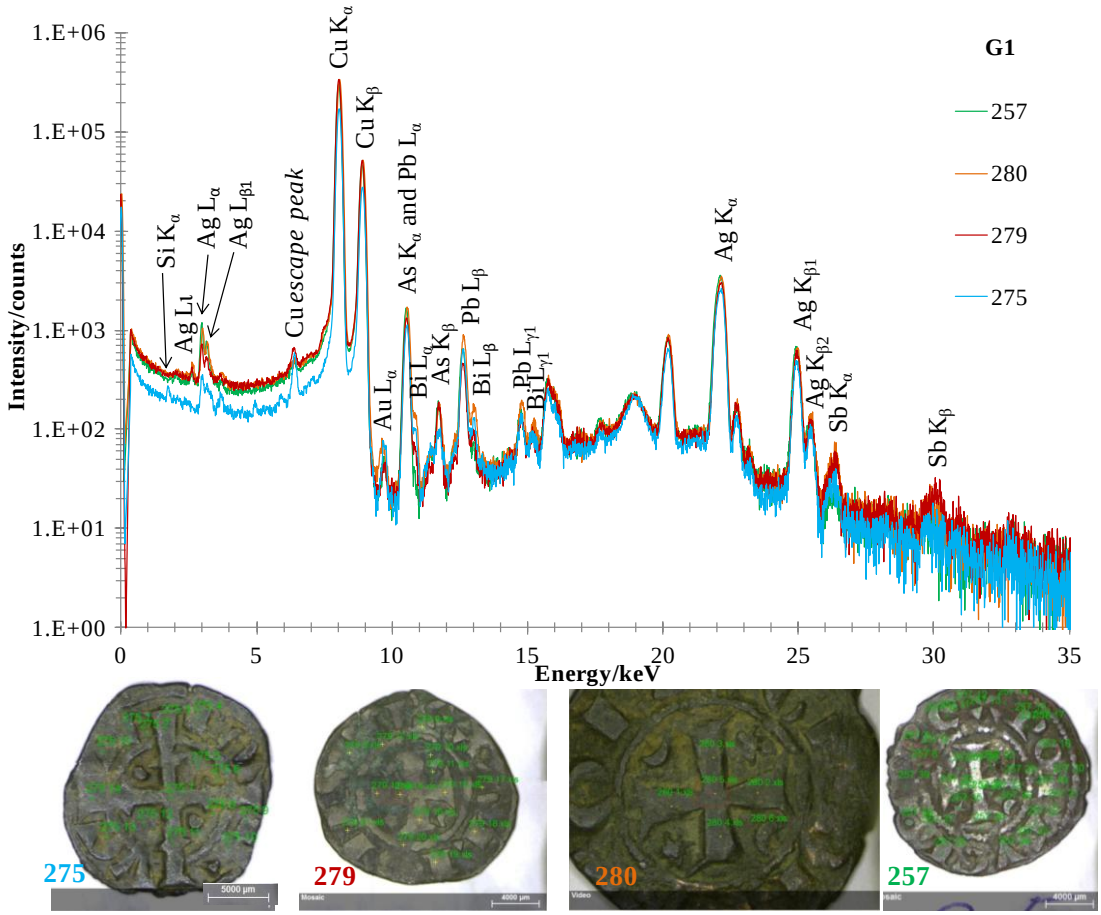

Figure 4.3 - µ-EDXRF spectrums and images obtained on G1 (275, 279, 280 and 257).

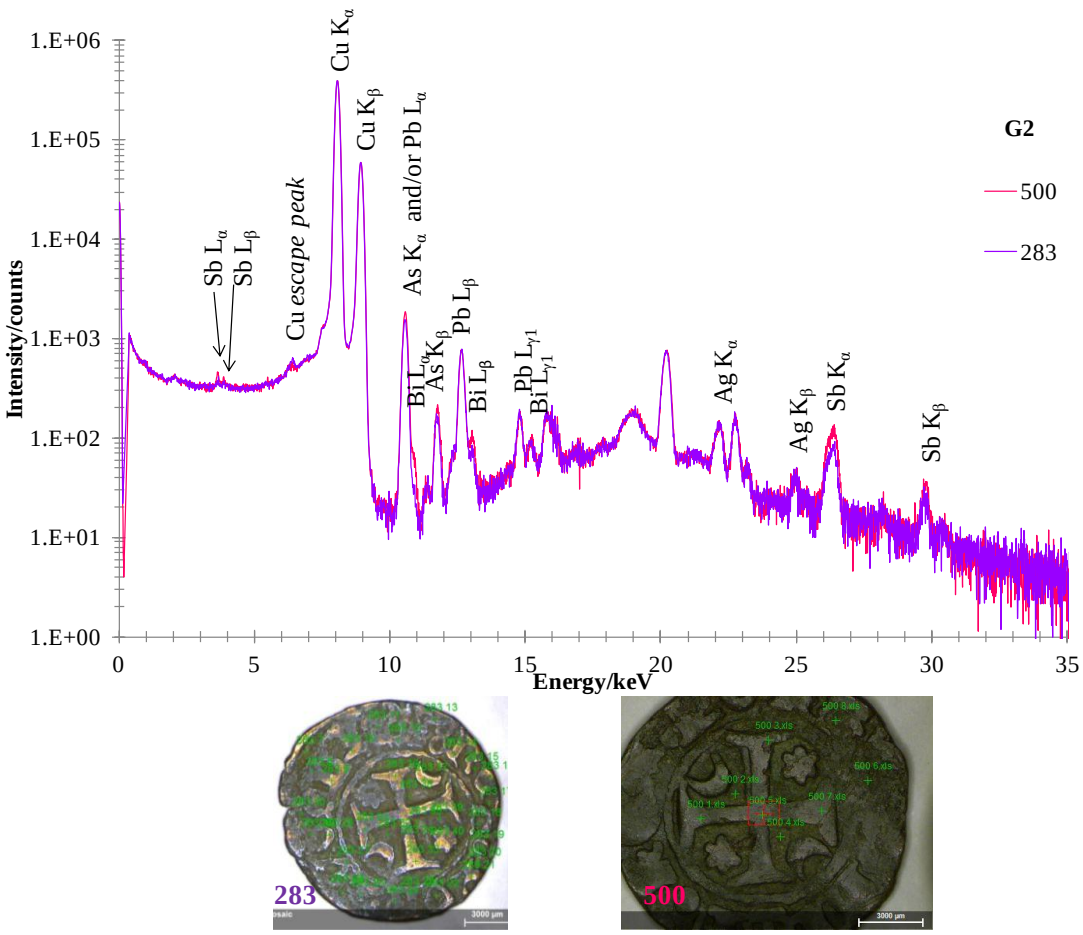

Figure 4.4 - µ-EDXRF spectrums and images obtained on G2 (283 and 500).

On both groups the main identified elements were arsenic, antimony, lead, bismuth and, the most intense peak in all spectra, copper. Silver was also identified, but it is important to notice the difference in the intensity and the number of lines presented in both cases. The coins with less silver contents had fewer and less intense Ag peaks.

Based on the provenance and manufacturing chapters presented on this work some relationships can be proposed. Detected elements as Si, Cl, Ca, P and possibly K, Fe and Hg are present on this evaluation as contamination from the surrounding environment.

Cu, Ag, Bi and Au and possible Sb, Pb and Fe can be present as part of the ore, i.e. they are result of the ore provenance or, in the 3 last cases due to provenance or technology. The presence of lead can be, in fact, justified by the use of this element in order to achieve a better "fluidity" of copper and decrease the melting point of the metal during the manufacturing process of the coin [13]. The lead distribution can be strongly influenced by the cooling rate of the initial melting of the copper alloy. Indeed, this element is not substantially soluble on Cu so it is normally dispersed in the metallic

matrix [13]. The minor elements concentrations can be governed by ore mineralogy/composition or related to the smelting process.

Based on the date period of the coins (13rd and 14th centuries) As is probably present due to ore provenance or the technology methodologies used on the coins manufacturing; while S, Ti, and Sr can be present as a result of technology processes.

Anyway this should be a careful analysis since elements as silver, copper, lead and gold can be interpreted by casting irregularities, corrosion or by the process of chemical cleaning or enrichment/dilution. Even more, thermal and/or mechanical treatments can also induced changes in alloy composition.

4.3 X-ray Diffraction

X-ray Diffraction (XRD) technique was used in order to identify the crystalline patina products formed on the surface of the coins.

4.3.1 Coins analysis

Figure 4.5 presents the stacked XRD difractogram obtained on the studied set of *dinheiros*. The individual patterns and its respective peaks attribution can be seen on **Figures A.III.7** to **A.III.11** and **Tables A.III.8** to **A.III.15** on **Annexe A.III.2**. The patterns present the peaks which relative intensities are above, approximately, 2.0%.

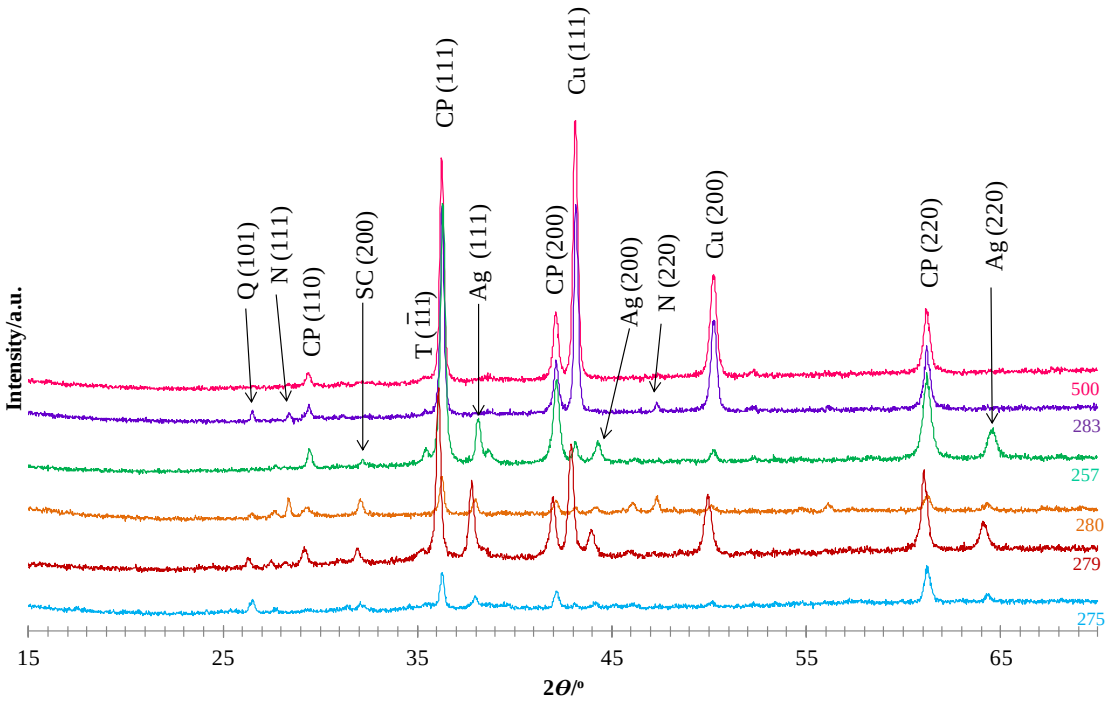

Figure 4.5 – Stacked XRD patterns obtained on the studied set of *dinheiros* Principal peak identification. Legend: Q-quartz; N-nantokite; CP-cuprite; SC-chlorargyrite; T–tenorite.

The obtained X-ray diffractograms identified: natives copper (Cu), silver (Ag) and lead (Pb); cuprite (Cu_2O), tenorite (CuO), malachite ($Cu_2CO_3(OH)_2$), nantokite (CuCl), atacamite ($Cu_2Cl(OH)_3$); chlorargyrite (AgCl) in the coins where high silver contents were present; and calcite ($CaCO_3$) and quartz (SiO_2), as the major crystalline products present on the studied set of coins. The peak identification was done according the JCPDS/ICCD database: 4-0836 (Cu); 4-0783 (Ag); 4-686 (Pb); 5-586 ($CaCO_3$, calcite); 5-288 (CuO); 5-0667 (Cu_2O); 6-0344 (CuCl); 10-399 ($Cu_2CO_3(OH)_2$); 25-269 ($Cu_2Cl(OH)_3$); 31-1238 (AgCl); 33-1161 (SiO_2).

Table 4.6 presents the relationship between the observed compounds and the respective coins where they were found:

Table 4.6 – Correlation between the identified peaks on XRD patterns and the respective coins.

		275	279	280	257	283	500
Native copper	**Cu**	•	•	•	•	•	•
Native silver	**Ag**	•	•	•	•		
Native lead	**Pb**					•	
Cuprite	**Cu_2O**	•	•	•	•	•	•
Tenorite	**CuO**	•	•		•	•	•
Malachite	**$Cu_2CO_3(OH)_2$**	•	•				
Nantokite	**CuCl**		•	•		•	
Atacamite	**$Cu_2Cl(OH)_3$**			•			
Chlorargyrite	**AgCl**	•	•	•	•		
Calcite	**$CaCO_3$**						•
Quartz	**SiO_2**	•	•	•		•	

Some important conclusions could be taken from the information exposed above.

Native copper (Cu) was identified in all coins. Even more, this element which presents a cubic crystal system was the most intense peak on the coin with the catalogue number 500. Moreover, cuprite (Cu_2O) (that also presents a cubic symmetry) was present in all coins and it was the most intense peak for all the remaining *dinheiros*. In fact, from the analysis of the total set of obtained patterns it was possible to conclude that cuprite is the major product on the samples. This is the first patina compound that is formed over time.

Other typical crystalline copper corrosion products were indentified. Tenorite (CuO) on 275, 279, 257, 283 and 500 coins and malachite ($Cu_2CO_3(OH)_2$) on 275 and 279, both with a monoclinic symmetry. Nantokite (CuCl) on coins with the catalogue numbers 279, 280 and 283 and atacamite ($Cu_2Cl(OH)_3$) on 280 were also recognized. These two last compounds present cubic and orthorhombic crystal symmetries, respectively.

Chlorargyrite, a cubic crystal system of AgCl, was identified on the coins with high silver contents (quantified by μ-EDXRF) and where native silver (identified by XRD) were present, namely on 275, 279, 280 and 257 (G1) coins. Native silver (cubic symmetry) or its degradation products are not present on the coins dated from of D. Fernando I kingdom (G2).

On coin with the catalogue number 283 was also identified native lead (Pb).

Finally, quartz (SiO_2 – hexagonal symmetry) in all coins expect 500 and calcite ($CaCO_3$ - rhombohedral crystal system) on this *dinheiro* were identified too.

A final note to the fact that no specific support was used in the patterns acquisition. The coins were directly placed under the sample holder to be analyzed.

Patina compounds *vs* environment:

To propose a supported and detailed corrosion mechanism it would be very important the knowledge of the coins provenance as well as a detailed study of the soils or walls where these objects were found. However this information is absolutely unknown for the studied set of *dinheiros*. As a result, it is only possible to try to establish a possible relationship between the patina constituents and its probable surrounding environment.

Based on patina evolution along time and environment (summarized on **Figure 4.6**) a relationship between copper and its corrosion products can be notice. In fact, it seems like that what happened in practice is the interconversion of cuprite according the different reactions between Cu_2O and the environment, originating various patina products: firstly, tenorite and nantokite and then malachite and atacamite. Even more, Cu_2O presence may indicate not so aggressive coins´ environmental exposure or a possible cleaning once this inner layer is identified as the main patina compound in all coins.

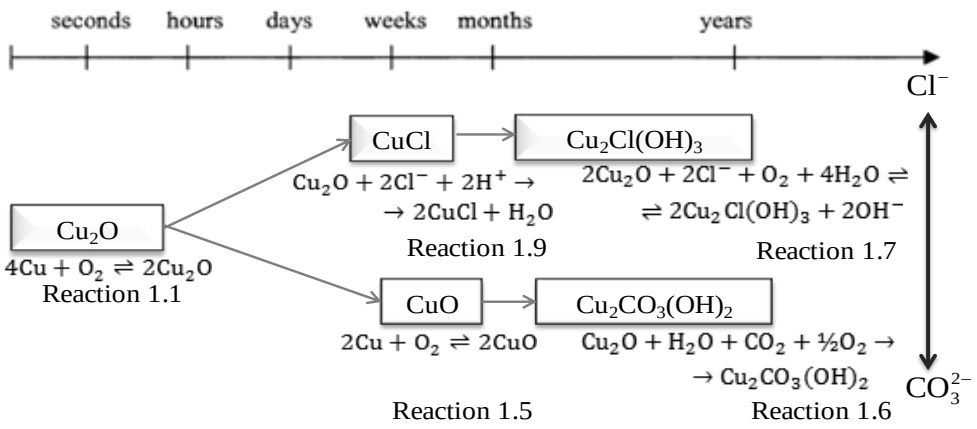

Figure 4.6 – Main compounds found on patina layers of the studied coins. Possible patina evolution with time and environment of exposure and its possible formation reactions.

According to the crystalline identified compounds it is possible that the coins had been in contact with chlorine and/or carbonate rich environments. The presence of chloride compounds on the coins surface, namely nantokite or atacamite can be due to marine proximity.

In this Cl^- rich environment silver corrosion products can be formed on copper enriched areas, namely the observed chlorargyrite, particularly induced by oxygen and humidity:

$$Cu^{2+} + 2Cl^- + Ag \rightleftharpoons AgCl + CuCl \qquad \text{Reaction 1.17}$$

This was the only silver crystalline corrosion product identified.

Finally, the identification of quartz and calcite may be related with some crystalline impurities presence on the surface of the coins.

As consequence of the so far results, a general stratification scheme on the interactions between the metallic surface, its patina components and the surrounding marine environment can be suggest (**Figure 4.7**):

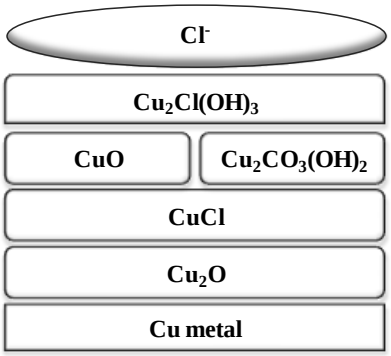

Figure 4.7 – Possible stratification scheme of species in a Cu corrosion film on marine rich environment.

4.3.2 Coin 275: a particularly case of study

Coin with the catalogue number 275 was a particularly case of study once it was the only *dinheiro* with visibly damaged surface. **Figure 4.8** presents the XRD patterns obtained on this sample on both obverse and reverse faces, particularly, was tried to accomplish the measurements on the visibly corroded area ("cauliflower" denoted by R2) and the on rest of the coin reverse (denoted by R1).

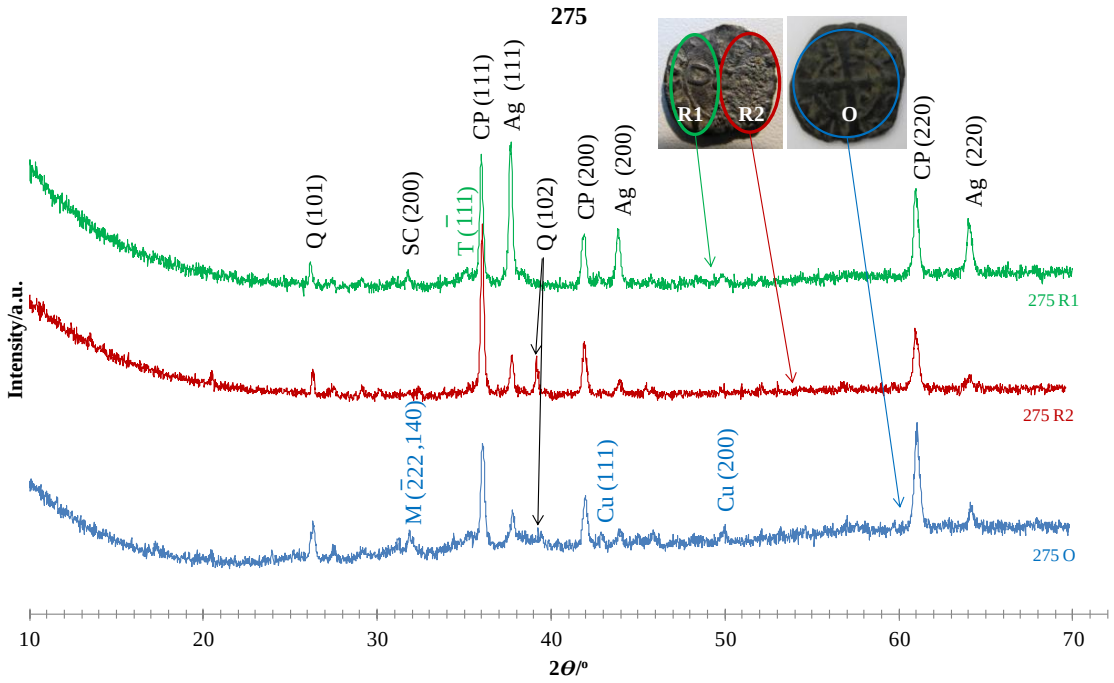

Figure 4.8– Powder XRD patterns obtained for 275 coin on both obverse (blue line denoted by 275 O) and reverse faces, particularly, the visibly corroded area ("cauliflower" – red line denoted by 275 R2) and the rest of the coin reverse (green line denoted by 275 R1).

Legend: M-malachite; Q-quartz ; SC-chlorargyrite; T-tenorite; CP-cuprite.

The analysis of this coin deserved special care taking into consideration the lack of precision in the coin position for the analysis. It was tried to investigate these specific areas however is not safeguarded the precision on the exact placement of the coin under analysis.

Based on these results it can be concluded that the main difference between both "cauliflower" area and the rest of the coin surface were the most intense peaks and the tenorite and malachite identifications. Cuprite was the most intense peak on 275 O and 275 R1 diffractograms while silver corresponded to the 100 % peak on this particularly corroded surface (275 R2). Apart from this difference no other significant distinctions were noted.

4.4 Scanning Electron Microscopy / Energy Dispersive X-ray Spectroscopy

Scanning Electron Microscopy coupled with Energy Dispersive X-ray Spectroscopy (SEM/EDS) was used with the view to characterize and identify the morphology and the chemical element distribution along the *dinheiros* surface, helping to understand the corrosion mechanism and the patinas constituents.

4.4.1 Surface analysis

More or less corroded the total set of the studied *dinheiros* were almost completely coated with a smooth and in the low relief areas a dense patina layer. On the high relief areas this layer revealed the metallic core mixed with possible patina oxides, chlorides and/or carbonates. This uplayer should be a protective coating patina since almost all the coins looked, on a macroscopic scale, well preserved. Furthermore, it was also clear the presence of silver and its corrosion products denoting the possible presence of silver surface enrichment.

However, on a micro and nanometre scale some typical corrosion signs could be observed. **Figure 4.9** presents some SEM images on the surface of five of the studied coins:

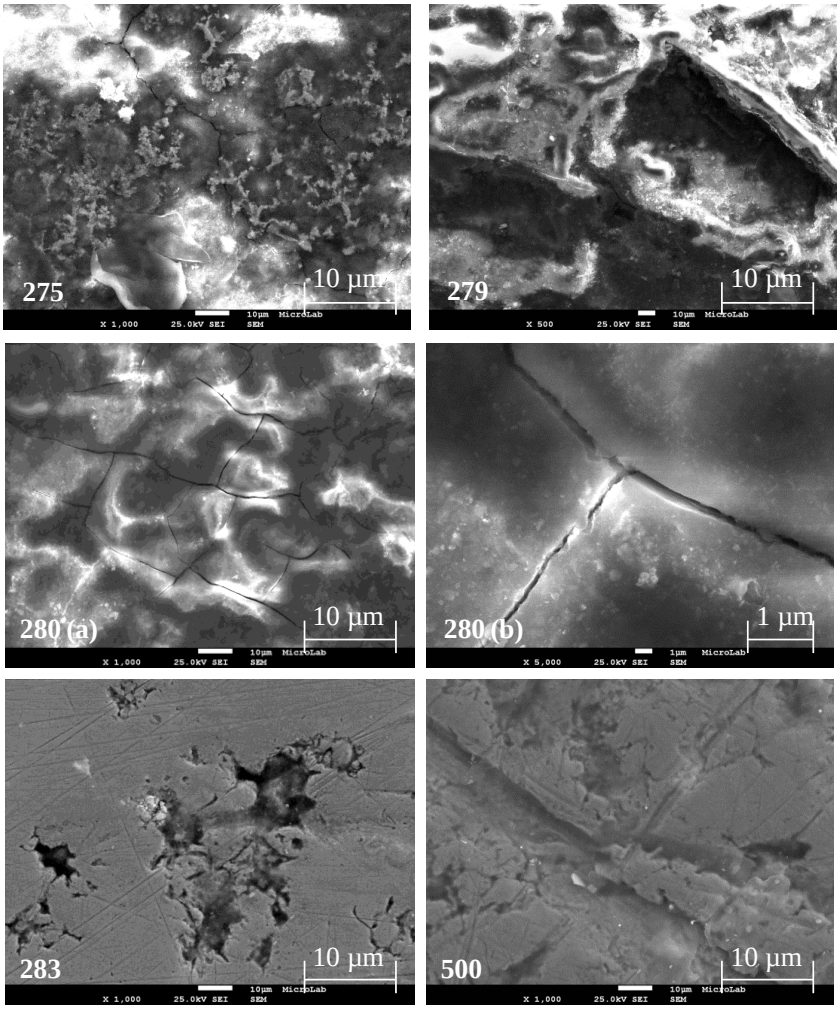

Figure 4.9 – SEM images on the surface of five of the studied coins.

Typical corroded fractures and fissures along the surface could be seen, mainly on 275 and 280 coins (compatible with μ-EDXRF and XRD results). The brittle behaviour on billon alloys is not uncommon. Here, several perpendicular and parallel cracks were observed. These fissures caused probably by hydration and dehydration of the corrosion components are served as a starting point for a localized corrosion. They may also result from changes in volume resulting from corrosion. The conversion of nantokite into atacamite is followed through volume expansion (sample 280) which favours the transfer of elements from the environment to the coin surface, promoting its intergranular corrosion. Moreover, silver corrosion products are extremely aggressive. Among others they may have been one of the causes of 275 coin fissures.

Some black cavities could be identified too (mainly on coins 279 and 283). They may had caused leaching and diffusion of copper during the corrosion process.

Meanwhile, SEM images of the uplayer (**Figure 4.10**) indicate a compact surface on 279(a) and 257 coins and a porous morphology on 275, 279(b), 283 and 500 samples.

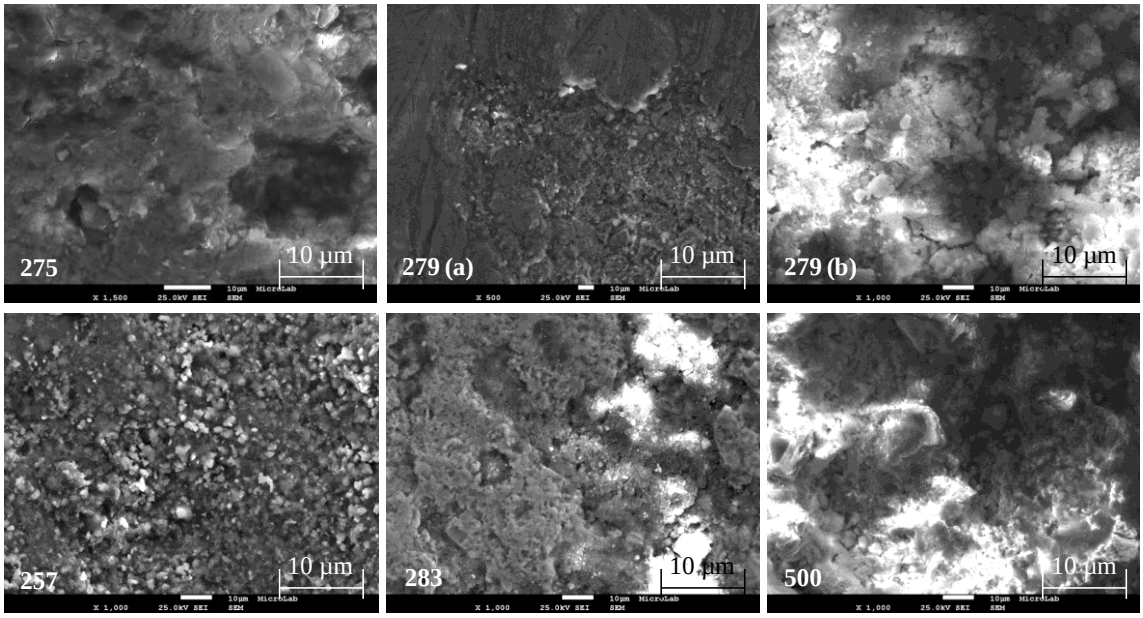

Figure 4.10 - SEM images on the coins surfaces regarding compact (279 (a) and 257) and porous (275, 279(b), 283 and 500) patina layers.

Note the white flakes on the above figures (**4.9** and **4.10**). These "clouds" should be loosely adherent corrosion products and are generally associated with high deposition rate of chlorides.

4.4.1.1 Identified phases

By the use of SEM/EDS two main phases were identified: copper/copper oxides (in all samples) and silver/silver chloride (on G1[8] *dinheiros*). Moreover, other particularly morphologies were also identified, namely Si, Ca and Pb rich phases. SEM/EDS results can be seen in detail on **Annexe A.III.3** (**Figures A.III.12** to **A.III.24**).

Figure 4.11 presents some examples of the identified copper and copper oxides phases:

[8] Remember that G1 is composed by 275, 279, 280 and 257 and G2 by 283 and 500 coins.

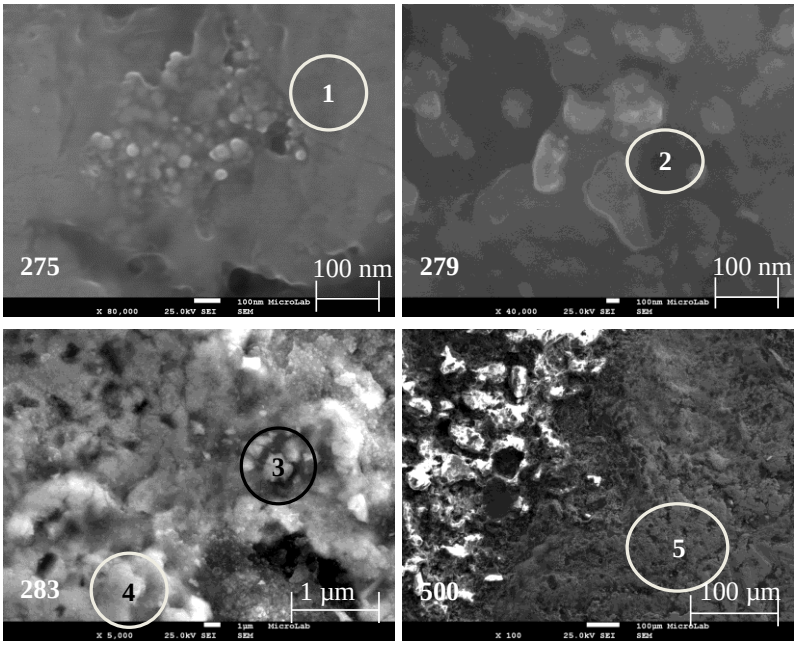

1. Cu: 66.80 wt.%, O: 33.20 wt.%
2. Cu: 56.55 wt.%, O: 43.45 wt.%
3. Cu: 67.14 wt.%, O: 32.86 wt.%
4. Cu: 68.85 wt.%, O: 27.18 wt.%
5. Cu: 66.90 wt.%, O: 36.34 wt.%

Figure 4.11 – SEM/EDS copper phase examples obtained for 275, 279, 283 and 500.

Mainly copper and oxygen (O) were quantified on a relative ratio of approximately 2:1. Once the metal is the main alloy constituent the presence of O can be related with the patina compounds. Moreover, as cuprite was the main crystalline corrosion product identified by XRD it can be concluded that this Cu rich phase is mainly constituted by Cu, Cu_2O or even CuO. However, it should be noticed that not only Cu was identified on these spots. Also Si and Cl (both on site **(4)** and the last one on site **(5)**) were detected and quantified in contents lower than3.21 wt.%.

Many of this copper rich areas are surrounded by another phases. For example, **Figure 4.12** presents the identified copper **(1)** and silver **(2)** morphologies on coin 257. Owing the presence of chloride it can be assumed that both phases can be constituted by metallic Ag/AgCl and in fewer amounts by metallic Cu/CuCl compounds. Even more, it cannot be ignored the existence of other non-crystalline corrosion products, such as copper or silver oxides, sulphides, etc.

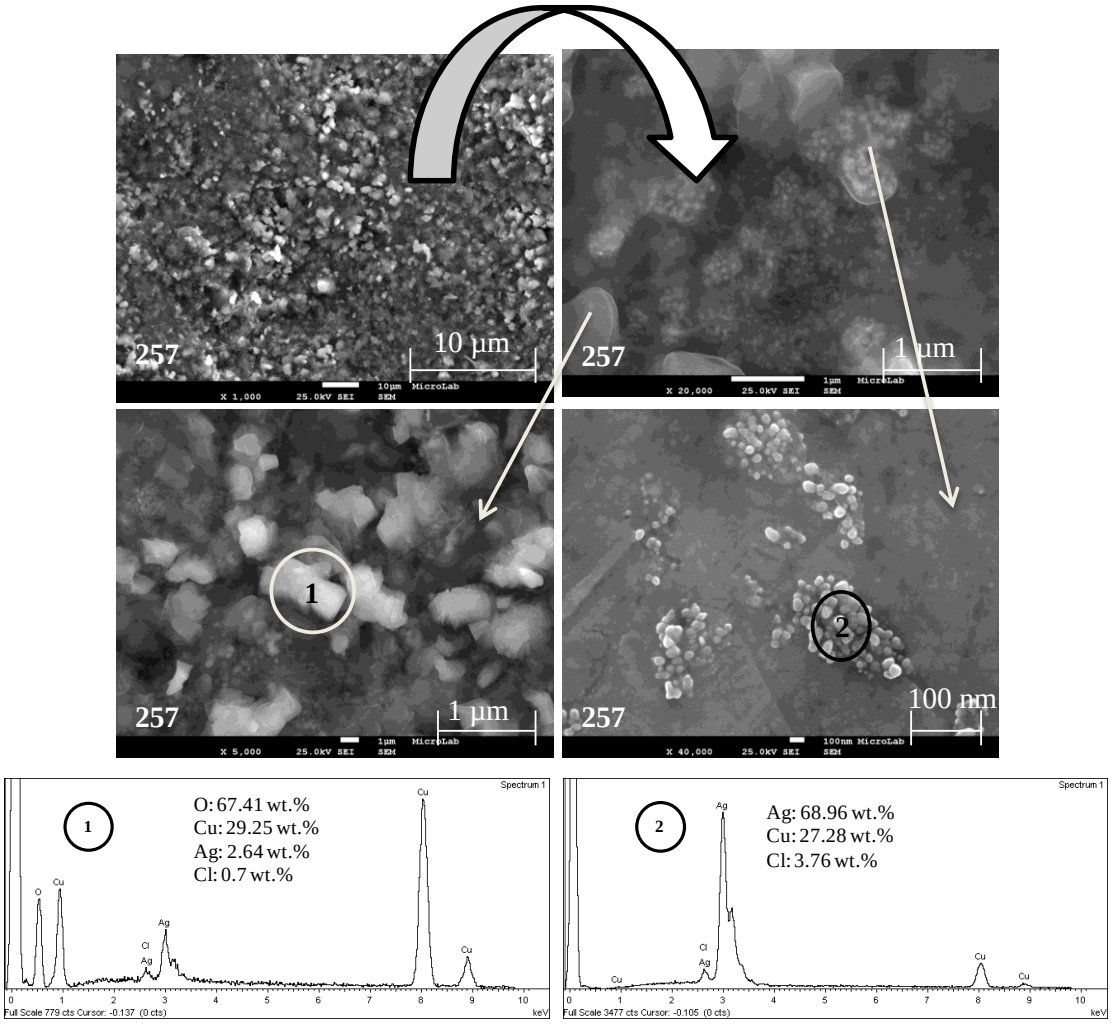

Figure 4.12 – SEM/EDS copper **(1)** and silver **(2)** phases obtained for 257.

Silver phase was identified on 275, 279, 280 and 257 coins. These results are in concordance with the ones obtained by µ-EDXRF and XRD. Even more, the presence of significantly silver contents on large areas on the coins represents a normal behaviour in the Cu/Ag alloy due to the low solubility of silver on copper, and vice versa, at room temperature. During the cooling system, each component is separated in a pure state. Thus formed Ag enriched areas dispersed in the copper matrix, whose size will be dependent on the cooling rate [14]. However, the manufacture of coins can also promote macroscopic or microscopic segregations.

At this point it is important to notice that these two different phases (Cu and Ag) can be characterized by very different morphologies. The observed dark areas were copper typical accidence; while silver phases were identified as bright areas with "cluster" organization. On the other hand, copper/copper oxides were presented on dense, plain or cuboid, arrangements.

Figure 4.13 shows some silver phases identified on 279 and 280 coins.

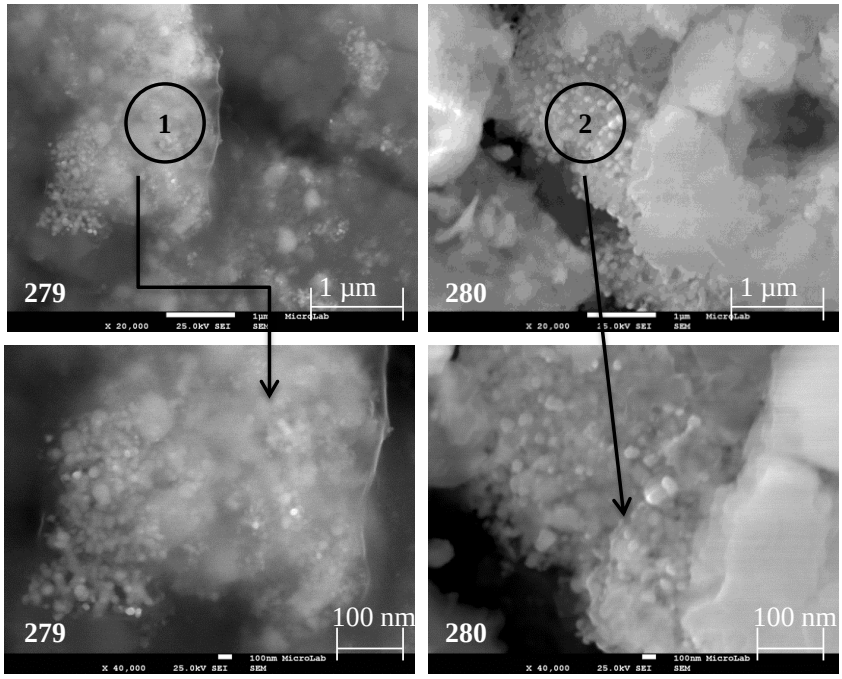

1. O: 43.94 wt.%,
   Ag: 22.71 wt.%,
   Cu: 19.92 wt.%,
   Cl: 10.50 wt.%

2. O: 55.93 wt.%,
   Ag: 17.11 wt.%,
   Cu: 8.9 wt.%,
   Cl: 5.69 wt.%

Figure 4.13 – SEM/EDS silver phase examples obtained for 279 and 280.

Regarding the above examples exposed on **Figure 4.13**, 279 **(1)** and 280 **(2)** coins, presented other minor elements were identified, namely, Si (in both coins), Ca, P, Al and Fe (all in 280). As SEM/EDS is a surface technique it can be concluded that these are exogenous elements and were present on the coins surface due to environmental contamination, particularly, during patina formation or even dust incrusting the corrosion products [17]. Once again, these results are in concordance with the ones obtained by µ-EDXRF.

Other different morphologies could be identified by SEM:

- Silicon (**Figure 4.14**) and calcium (**Figure 4.15**):

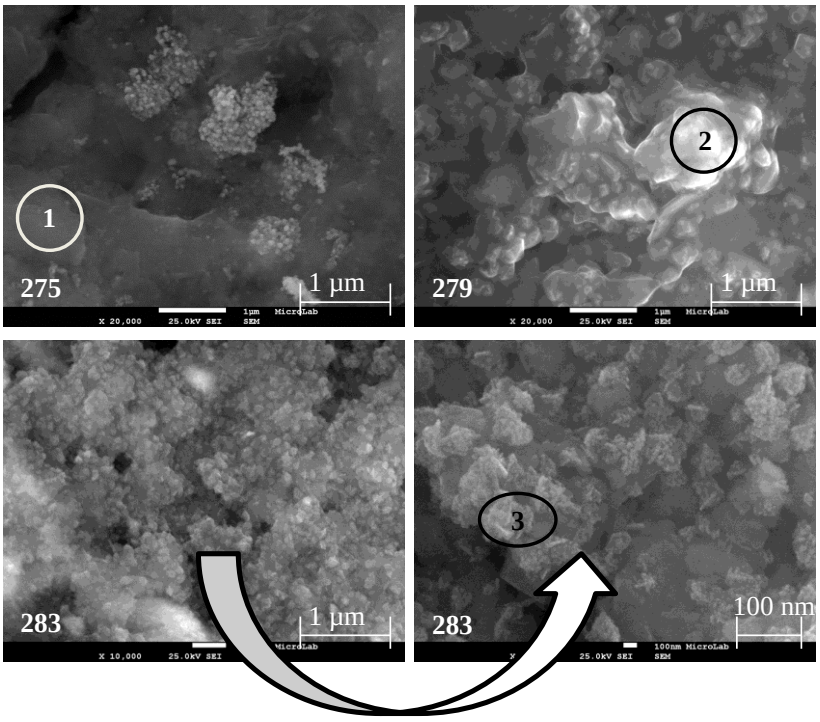

1. O: 66.76 wt.%, Si: 21.86 wt.%
2. O: 71.88 wt.%, Si: 17.99 wt.%, Cu: 10.12 wt.%
3. O: 53.91 wt.%, Si: 24.82 wt.%, Cu: 18.02wt.%

Figure 4.14 – SEM/EDS silicon phase obtained for 275, 279 and 283.

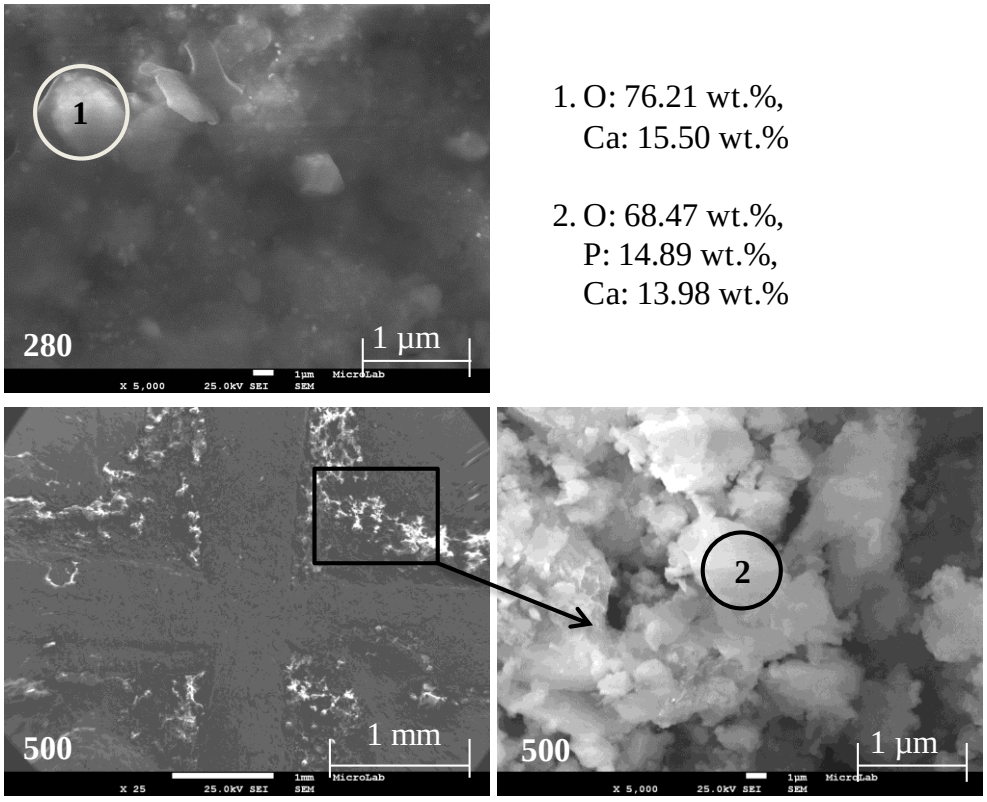

1. O: 76.21 wt.%, Ca: 15.50 wt.%
2. O: 68.47 wt.%, P: 14.89 wt.%, Ca: 13.98 wt.%

Figure 4.15 – SEM/EDS calcium phase obtained for 280 and 500.

Both silicon (**Figure 4.14 – (1), (2), (3)**) and calcium (**Figure 4.15 - (1), (2)**) are exogenous elements constituents of patina. As proposed before their presence should be related with surrounding environment contamination. Even more, as can be seen on the coin with the catalogue number 500 (**Figure 4.15 – 1 mm** scale) the major impurity contents are located on the low relief areas. These regions generally looked like white shiny areas on SEM images. This happens because they form generally light and loosely compounds.

- Lead (**Figure 4.16**):

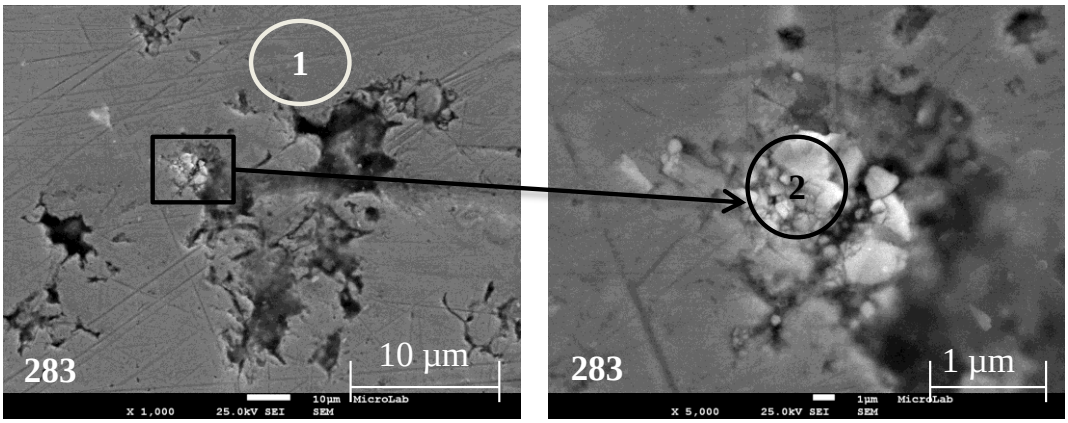

1. C: 57.03 wt.%,
   Cu: 33.89 wt.%,
   O: 9.08 wt.%

2. O: 51.37 wt.%,
   Cu: 23.79 wt.%,
   Pb: 12.47 wt.%

Figure 4.16 – SEM/EDS copper and lead phases obtained for 283.

The morphological details and the surface chemical composition of the patina disclose an interesting feature of the presence of lead. This element usually originates cracks and selective corrosion Pb islands which extend deeply in the metal surface, as can be seen on **Figure 4.16 (2)**. Note that 283 was the coin with higher content of lead by µ-EDXRF and the only one where crystalline Pb was identified by XRD. Pb presence is generally related to its very low solubility in copper and its low melting temperature with respect to that of the copper matrix as exposed already exposed on the µ-EDXRF data treatment.

In conclusion the results indicated that the *dinheiros* surface is characterized by a copper/copper oxide dense and plane layer. An external thin region where an appreciable silver/silver chloride/oxide enrichment was observed on a copper core characterized by a low Pb content (279, 280, 283) and a small amount of other minor elements such as Si, Ca, Al, Mg, P, S, K, Br, Fe, Sb, Sn.

4.4.2 Scraped edges

In order to investigate the coins edges SEM/EDS measurements were made. Here different treatments and samples were analyzed, namely, the non-scarped edges of 257 (constituted by Cu/Ag alloy) and 500 (mainly Cu) coins; and the manual scarped edge of 257 coin. **Table 4.7** present the obtained results. Moreover, **Annexe A.III.3** (**Figures A.III.25** to **A.III.27**) shows the detailed SEM/EDS results.

Table 4.7 - SEM/EDS obtained for 257 scraped and non-scraped edges and for 500 non-scraped edges.

Coin	SEM/EDS		
257 non-scraped edge	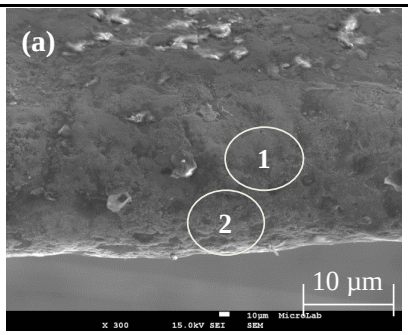	1.Cu: 66.87 wt.%, O: 22.10 wt.%, Cl, Ag, C < 4.42 wt.% 2.Cu: 95.03 wt.%, O: 4.16 wt.%, Cl: 0.81 wt.%	
257 scraped edge	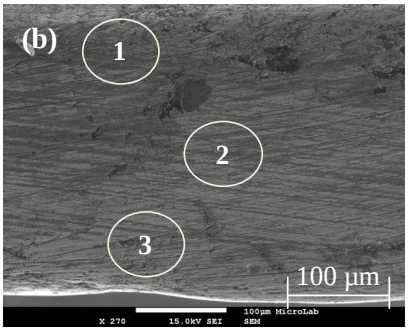	1.Cu: 87.93 wt.%, O: 4.84 wt.%, Ag: 3.10 wt.% 2.Cu: 95.75 wt.%, Ag: 2.75 wt.% 3.Cu: 96.03 wt.%, Ag: 2.73 wt.%	2,3: O < 1.50 wt.%
500 non-scraped edge	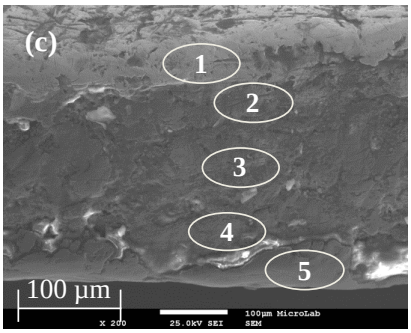	1.Cu: 94.20 wt.%, O: 5.80 wt.% 2.Cu: 91.63 wt.%, O: 3.33 wt.% 3.Cu: 91.89 wt.%, O: 3.96 wt.% 4.Cu: 86.68 wt.%, O: 4.91 wt.% 5.Cu: 81.37 wt%, Ni: 15.27 wt.%, O: 1.71 wt.%	2, 3, 4: Ni < 7.13 wt.% 4, 5: P < 1.65 wt.%

Based on this information it can be concluded that any linear conclusion can be assumed.

On 257 sample the copper content on both non-scraped **(a)** and scraped edge **(b)** increases from the upper **(1)** to the lower **(3)** edge of the coin, having Ag the opposite behaviour, i.e. silver content decreases "down" in the currency (from **(1)** to **(3)** sites) after cleaning **(b)**. Note that no silver content was detected on the sample with the

non-scraped edge. **(a)**. It is important to notice that copper content decreases (approximately 20 %) when the edge is scraped.

On the other hand, on 500 non-scraped edge **(c)** the copper content decreases from the upper **(1)** to the lower **(5)** edge of the coin. Here, oxygen was detected in all the analyzed sites and "down" in the coin, nickel content increased from **(3)** to **(5)**. Regarding to oxygen, is important to notice that on the first point only Cu and O were detected, this may justify the Cu_2O or CuO presence.

An examination of the coins cross-section would be very helpful in the determination of the exact composition of the substrate however conservators hesitate to remove the corrosion layer (once it could be a protective one) or damage the original piece.

5 CONCLUSIONS

The combined action of non-destructive analytical techniques of μ-EDXRF, XRD and SEM/EDS allowed interpreting the nature of patina products formed on the studied set of six antique Portuguese coins.

By the coins visual analysis regarding a macro scale morphologic approach several kind of patinas could be identified, namely a yellow- brownish layer on coins numbered 275, 279, 280 and 500 and a green one on 279 coin on the low relief areas; and a red-brownish coating on 257 coin.

The interaction of the environment with the metallic material was also evidenced by the μ-EDXRF and the SEM/EDS results through the presence of elements such as Si, Cl, Ca, P and possibly K, Fe and Hg outside the alloy composition of the artefact. Moreover, μ-EDXRF results allowed to admit that Cu, Ag, Bi, Au and possible Sb, Pb and Fe can be present as part of the ore. In fact, it was verified that all the coins were made on billon alloy (copper/silver). However it was historically and scientifically proven the metal debasement during D. Fernando I period of reign.

XRD analyses showed the presence of oxides, namely cuprite (Cu_2O) in all coins and tenorite (CuO). In some cases malachite ($Cu_2CO_3(OH)_2$) and some chlorides, mainly, nantokite (CuCl) and atacamite ($Cu_2Cl(OH)_3$) were also identified. Moreover, in the numisms with high silver content, chlorargyrite (AgCl) was identified too (275, 279, 280 and 275).

The evolution of corrosion can be assumed as the initial formation of cuprite in concordance with the medium interface and its subsequent conversion into other chemical compounds according to the surrounding environment. The significant chloride contents and products (CuCl, AgCl, $Cu_2Cl(OH)_3$) may indicate a marine rich environment, compatibly with the coastal location of Portugal.

Chlorides usually induce an autocatalytic copper corrosion. This fact may explain that 275 and 280 coins were the most damaged ones. This fact is proven by all the *micro* data collected. Finally is important to notice that other corrosion products should be present on the surface of the coins. However XRD is capable to detect only crystalline compounds. As consequence, other amorphous compounds are probably present as patina constituents, namely sulphates, phosphates, or others.

PART II

DEVELOPMENT OF NANOMATERIALS FOR CULTURAL HERITAGE CONSERVATION

6 EXPERIMENTAL PART

The experimental part on the development of nanomaterials for cultural heritage conservation consists on the syntheses and their characterization descriptions.

6.1 Synthesis of calcium carbonate and calcium hydroxide nanoparticles

6.1.1 Material and Reactants

For the experimental process all the glassware was previously decontaminated with a 1 $mol.dm^{-3}$ hydrochloric acid solution. The washing solution was made from HCl Carlo Erba Reagent 37% (w/w). The precipitates were prepared with Type I water obtained with a Milli-Q Elix 3 water purification system (R=5 to 15 MΩ.cm) (Merc Milipore). Ethanol (absolute) (Analar Normapur), CaO (Riedel-de Haen; assay 96-100.0%) and DA (Fluka Analytical; assay > 99%) were used. The carbon dioxide was obtained from a CO_2 welding gas cylinder model: 1480-10 (950 cc volume, tare 1120 g and 390 g of maximum content).

6.1.2 Procedure

In order to prepare the calcium carbonate nanoparticles the route proposed by Chen et al. [68] was followed.

The process starts with the calcium hydroxide suspension preparation. It was done dispersing, approximately 2.356 g of CaO into 50 cm^3 of deionised water, at 80°C (constant temperature) and kept overnight for ageing. A 0.1 $mol.dm^{-3}$ ethanolic solution of dodecanoic acid (etanhol:DA) was prepared. Solution concentration was maintained constant varying only the volume added to the suspension. 0.5%, 1.5%, 2.0% and 5.0% (w/w)[9] suspensions were prepared. **Annexe IV** presents the criteria used in the suspensions choice (**Figure A.IV.1**) and a detailed description on the amounts of CaO (g) and ethanol:DA (dm^3) used (**Table A.IV.1**). In order to simplify the text notation henceforth representative of the different dosages of the suspensions will *x*% DA (*x* = 0.0, 0.5, 1.5, 2.0 or 5.0). The mixture was stirred, at room temperature, and under magnetic starring for 2 hours. $Ca(OH)_2$ nanoparticles were collected by separating

[9] 2.0% (weight DA/weight $CaCO_3$).

the suspension, at this point, in two parts. Approximately half of the suspension was collected and kept until wash and dry.

A continuous flow rate of CO_2 was carried into the remaining suspension with pH control (pH≈7 units) and the $CaCO_3$ suspensions were collected. The white powders were separated from the mother liquid by vacuum filtrations and were washed with deionised water and ethanol, several times.

All the solids were dry in vacuum oven, at 60^{o}C, for 24 h.

6.2 Characterization of calcium carbonate and calcium hydroxide nanoparticles

In order to study the nanoparticles´ stability; chemical nature; morphology and crystalline phase, their shape and size (including the surface characteristics and surface modifications) several techniques were used, namely visual dispersion analysis and turbidimetry; Attenuated Total Reflectance (ATR); X-ray Diffraction (XRD) and Scanning Electron Microscopy (SEM), respectively.

6.2.1 Nanoparticles dispersions analysis

Several dispersions, using proportional amounts of $CaCO_3$ (~0.027 g) and $Ca(OH)_2$ (~0.020 g) synthesized powders were made (**Annexe IV** (**Table A.IV.2**)). The dispersions were prepared in cyclohexane obtained from PA Panreac (assay > 99.5.0%) to a 20 cm^3 total volume glass flask. The dispersions were sonicated in an ultrasound bath (Elma S 30H from Elmasonic) in various cycles of 10 minutes each. The number of cycles is dependent on the experience. In order to analyze the nanoparticles stability only the dispersions with the same number of cycles were compared.

Based on the obtained results was decided that the highest point of interest were the 0.0% and 5.0% DA $CaCO_3$ nanoparticles. For this reason a few more dispersions were made for the 5.0% functionalization, in order to compare all the dispersions and their stabilization capability varying the non-polar solvent, nonane (Sigma Aldrich), and/or introducing, on both dispersions (cyclohexane and nonane), 3 drops of 1-butanol (Fluka Chemika; assay > 98.0.0%) to analyze the changes that this solvent may, or may not, induce (**Table A.IV.3** in **Annexe IV**).

6.2.2 Turbidimetry

Turbidimetry was used in order to study the particles´ stability on the cyclohexane dispersions. The equipment used was a Cary100 Bio, UV-Visible spectrophotometer, from Agilent Technologies, controlled by a Cary WinUV Kinetics software. The measuring conditions were set as follows: wavelength fixed on 500 nm and a time-cycle´ analysis depending on the observed stability on the dispersion.

6.2.3 Attenuated Total Reflectance

To study the chemical nature of the samples was used Attenuated Total Reflectance (ATR) technique. These measurements were performed with an Nexus 870 FTIR ESP spectrometer with a golden gate (Thermo Nicolet) and a Graseby diamond ATR accessory (Specac), coupled with OMNIC software. $CaCO_3$ functionalized powders with 0.0% DA and 5.0% DA spectrums were recorded at a constant ambient temperature with a spectral resolution of 2 cm^{-1} (λ: 400-650 cm^{-1}).

6.2.4 X-ray Diffraction

The powder X-ray diffraction patterns were recorded on a Bruker D8 Advanced diffractometer coupled with a DIFFRAC-EVA commander software. The sample analyses were made on the 0.0% and 5.0% DA functionalized $CaCO_3$ powders, using Cu-K_α radiation, applying a tension of 40 kV and a current of 40 mA. The 0.02° steps in the 2θ range from 5° to 80° were selected to analyse the crystal structure. Structural characterization of the samples was based on the # PDF-2-2003 database, on JCPDS/ICCD data and according to literature [66, 75, 103].

6.2.5 Scanning Electron Microscopy

Finally for the nanoparticles´ morphology characterization (shape and size) was used a Gemini FE-SEM for nano-scale analytics (Sigma Zeiss) coupled with Smart SEM software. Instrument setting was optimised for each single analysis looking for "compromise" conditions ensuring the best analysis quality by the detectors. The only fixed value was the extra high voltage set at 5.0 kV.

7 RESULTS PRESENTATION AND DISCUSSION

In this chapter a full presentation and discussion of the obtained results both global and at the various stages of the experimental procedure is presented.

7.1 Nanoparticles´ visual dispersions analysis

Several $CaCO_3$ and $Ca(OH)_2$ dispersions were prepared in non-polar solvents, namely cyclohexane and nonane. Theoretically they must be stable for a period of 18 h to 24 h but in practice this point was not achieved.

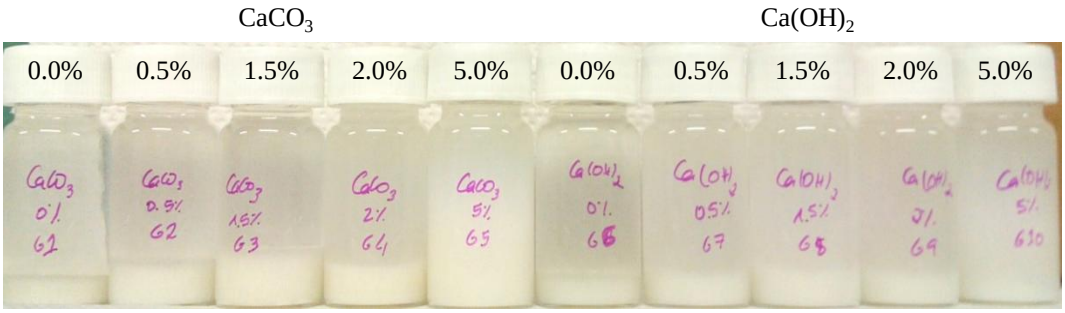

Figure 7.1 – $CaCO_3$ and $Ca(OH)_2$ nanoparticles dispersions in cyclohexane from 0.0% to 5.0% DA after 6 ultrasound cycles, 10 min each.

Figure 7.1 presents the results for the 0.0% DA to 5.0% DA $CaCO_3$ and $Ca(OH)_2$ dispersions in cyclohexane after 6 ultrasound cycles of 10 min each and settling for 30 min.

After settling for 24 h it could be seen that, for the 0.5% and 1.5% DA dispersions any or just a little amount of powder was suspended into the dispersion. Here the cyclohexane phase remained transparent and the powder was (almost) completed settled down. For the 5.0% DA dispersions the suspended amount of powder was superior and some flocculation processes were observed.

7.1.1 Number of ultrasonic cycles dependence

During this work the influence of the number of ultrasonic cycles on the $CaCO_3$ and $Ca(OH)_2$ dispersions were studied.

After vary the number of cycles but maintaining the period of it, it was concluded that more cycles improve the nanoparticles dispersion.

7.1.2 Other dispersions (nonane and 1-butanol influence)

Visually comparing the stabilizing effect of the different solvents (cyclohexane; nonane; cyclohexane+1-butanol and nonane+1-butanol) on the $CaCO_3$ and $Ca(OH)_2$ dispersions it could be concluded that, after the 3 first ultrasocinc cycles the most stable dispersion was the one with nonane+1-butanol. However, increasing the number of cycles it made clear that the best dispersion was the one composed only by cyclohexane. Another interesting conclusion was that 1-butanol increased the dispersion speed however it did not make teh dispersions more stable.

Maybe any other solvent or mixture of solvents can produce more stable solutions however, based on the visual stability tests, cyclohexane is the best tested organic non-polar solvent for the obtained $CaCO_3$ nanoparticles.

7.1.3 Nanoparticles dispersions conclusions

It could be concluded that the stabilization time of each dispersion was incompatible with the proposed end because it was too short in time. Thus, at this point and based only on their visual analysis, theoretically, these dispersions could not be used advantageously and with positive results for paper conservation.

7.2 Turbidimetry

Depending on the particles´ visual dispersions stability different time-cycle´ analyses were used on turbidimetry tests (**Table 7.1**).

Table 7.1 – Time of analyses for the various cyclohexane dispersions of $CaCO_3$ and $Ca(OH)_2$.

% (w/w)	Time/min	
	$CaCO_3$	$Ca(OH)_2$
0.0	60	60
0.5	60	60
1.5	120	120
2.0	120	116.4
5.0	102	120

Graphically and based on the obtained results it was found that no significant changes in the dispersions´ stability occur from 60 min on. Therefore, are now presented the stacked graphs with a maximum time limit of 60 min. **Figures A.V.1** to **A.V.5** and **Figures A.V.6** to **A.V.10** (**Annexe A.V.1**) present the full graphic results on $CaCO_3$ and $Ca(OH)_2$ systems, respectively, for the full time range.

7.2.1 $CaCO_3$ dispersions

Figure 7.2 represent the stacked turbidimetry results for the $CaCO_3$ with 0.0, 0.5, 1.5, 2.0 and 5.0% DA dispersions in cyclohexane.

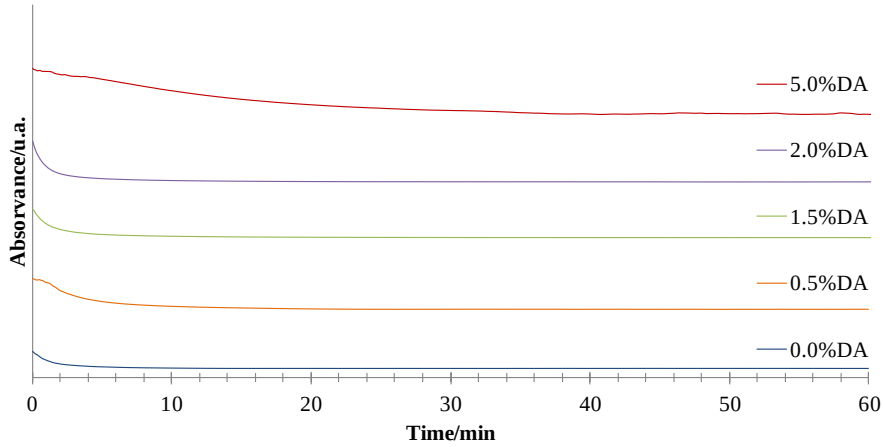

Figure 7.2 – Stacked turbidimetry results for the $CaCO_3$ with 0.0, 0.5, 1.5, 2.0 and 5.0% DA dispersions in cyclohexane.

Table 7.2 shows the result comparison for the $CaCO_3$ nanoparticles dispersions from 0.0% to 5.0% DA.

Table 7.2 – Turbidimetry results comparison for the $CaCO_3$ with 0.0% to 5.0% DA dispersions in cyclohexane, respectively. Legend: t_1 – time until the curve reaches its constant value; abs_c – constant value of absorbance; abs_i – initial value of absorbance.

	$CaCO_3$			
% DA	**Abs_i/u.a.**	**abs_c/u.a.**	**abs_c-asb_i**	**t_1/min**
0.0	0.852	0.320	0.533	10.401
0.5	1.191	0.230	0.962	18.001
1.5	1.428	0.507	0.920	25.201
2.0	1.621	0.315	1.306	36.601
5.0	1.949	0.499	1.450	72.901

As expected, the initial absorbance value grew from the dispersions with 0.0% to 5.0% DA content, i.e. more percentage of dodecanoic acid in the dispersion, higher was the initial absorbance of it. Apart from this, it can be concluded that higher amounts of acid made the settling time slower. Regarding to these results it could be concluded that the $CaCO_3$ dispersions were not stable.

7.2.2 $Ca(OH)_2$ dispersions

The stacked turbidimetry results for the $Ca(OH)_2$ with 0.0, 0.5, 1.5, 2.0 and 5.0% DA dispersions in cyclohexane are present on **Figure 7.3**.

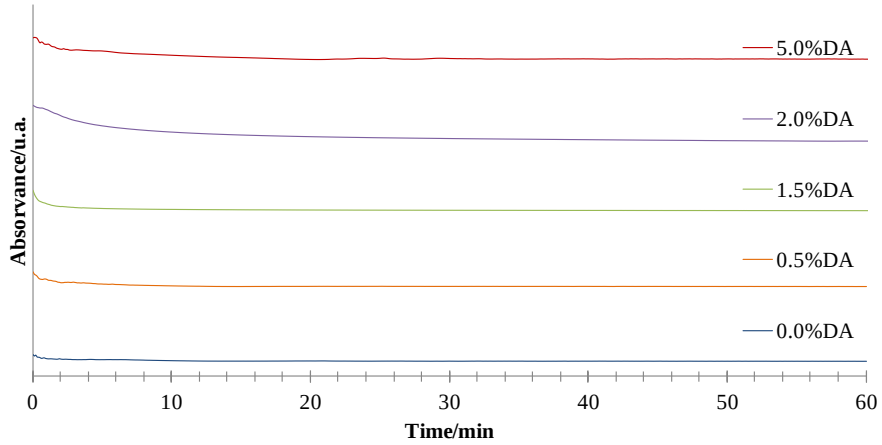

Figure 7.3 – Stacked turbidimetry results for the $Ca(OH)_2$ with 0.0, 0.5, 1.5, 2.0 and 5.0% DA dispersions in cyclohexane.

Table 7.3 presents the result comparison for the $Ca(OH)_2$ nanoparticles dispersions from 0.0% to 5.0% DA.

Table 7.3 – Turbidimetry result comparison for the $Ca(OH)_2$ with 0.0% to 5.0% DA dispersions in cyclohexane, respectively. Legend: t_1 – time until the curve reaches its constant value; abs_c – constant value of absorbance; abs_i – initial value of absorbance.

		$Ca(OH)_2$		
% DA	**Abs_i/u.a.**	**abs_c/u.a.**	**abs_c-asb_i**	**t_1/min**
0.0	0.583	0.439	0.144	9.501
0.5	0.808	0.416	0.393	14.701
1.5	0.998	0.484	0.515	11.201
2.0	1.304	0.322	0.982	56.901
5.0	1.096	0.536	0.560	81.201

The $Ca(OH)_2$ dispersions had identical behaviour to the $CaCO_3$, under identical conditions and regarding the initial absorbance values and the time until the curve reaches its constant value, that is: higher DA percentages gave higher initial absorbance values and the time to reach stability increased from the low concentrated dispersion to the most concentrated one. The only exception is for the 0.5% DA sample which takes more time until reaches absorbance´ stabilization point than the immediately after content (2.0%); however the difference is not significant.

These results made clear that $Ca(OH)_2$ systems were more stable than the $CaCO_3$ dispersions. However it does not mean that they are perfect systems because neither one of them was enough stable for the proposed end.

7.2.3 Turbidimetry conclusions

Generally and schematically it could be concluded, for both carbonate/hydroxide systems, that:

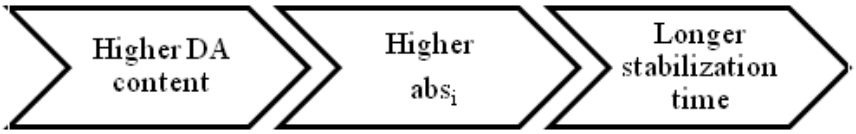

Turbidimetry results verified what the visual analysis on the dispersions gave idea about. Neither $CaCO_3$ nor $Ca(OH)_2$ dispersions, regardless the dodecanoic acid functionalization percentage, were stable enough to the proposed goal.

From this point on the analyses were made only for the calcium carbonate powders functionalized with 0.0% and 5.0% DA. This choice was made based on other studies that were being developed in the group as well as the innovation that comes from this new method of synthesis and dispersion.

7.3 Attenuated Total Reflectance

The stacked ATR spectra for $CaCO_3$ nanoparticles with 0.0% and 5.0% DA are presented in **Figure 7.4**.

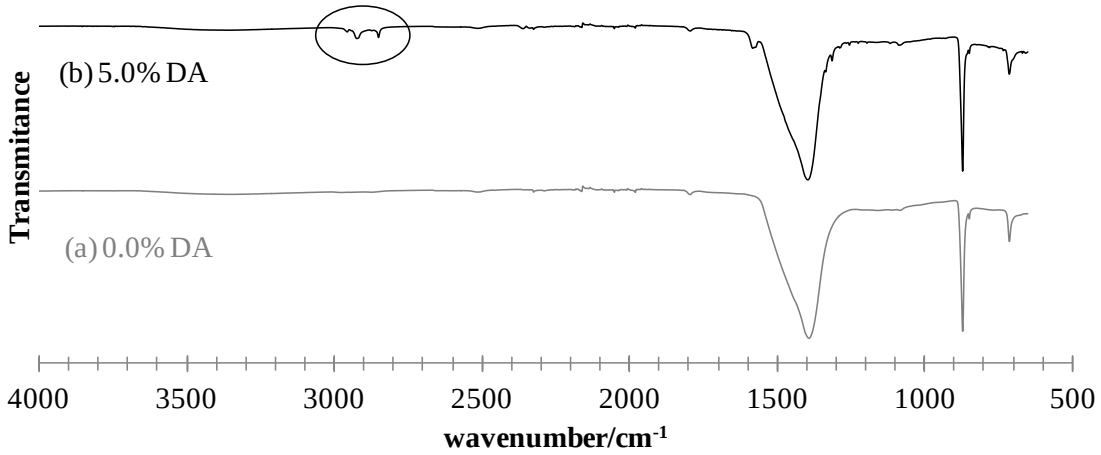

Figure 7.4 – ATR stacked spectra for $CaCO_3$ with 0.0% DA **(a)** and 5.0% DA **(b)** powders.

Table 7.4 exhibits the frequencies identification regarding to the ATR spectra peaks obtained for $CaCO_3$ 0.0% and 0.5% DA according to literature ([68, 104-106]) and numerous infrared tables.

Table 7.4 – Peak list identification on the ATR spectra obtained for $CaCO_3$ 0.0% and 0.5% DA powders. Legend: str – strong; med – medium; wk – weak; vwk – very weak.

0.0%DA	**ῡ/cm^{-1}**	**Intensity**	**Corresponding function**
	1391.39	str	υ_a (CO_3^{2-}) asymmetric stretching
	870.32	str	δ_a (CO_3^{2-}) asymmetric bending
	712.22	med	δ_s (CO_3^{2-}) symmetric bending
5.0%DA	**ῡ/cm^{-1}**	**Intensity**	**Corresponding function**
	2923.45	wk	υ (-CH) stretching
	2849.74	wk	
	1581.67	wk	carboxylate – carboxylic acid salt
	1395.04	str	υ_a (CO_3^{2-}) asymmetric stretching
	1400-1200	wk-vwk	δ (-CH_2, -CH_3) bending and υ (-CO) stretching.
	870.51	str	δ_a (CO_3^{2-}) asymmetric bending
	712.40	med	δ_s (CO_3^{2-}) symmetric bending

Calcium carbonate has a planar XY_3 type structure which allows symmetric and asymmetric stretching between the atoms in the CO_3^{2-} ions. Since CO_3^{2-} typical peaks were identified it could be concluded that on 0.0% DA powder, $CaCO_3$ was present in the sample. These results were used to confirm the presence of this compound on 5.0% DA synthesized powder.

On other hand the dodecanoic acid has a planar structure allowing the C-H (CH_2 and CH_3) bendings on the aliphatic chain as week as the C=O stretches by the acidic group. On 5.0% DA sample both DA and its respective carboxylic acid salt peaks were identified allowing to confirm its presence on the final compound.

7.4 X-ray Diffraction

Figure 7.5 presents the stacked X-ray diffraction patterns obtained for the 0.0% and 5.0% DA $CaCO_3$ powders. **Tables A.V.1** and **A.V.2** on **Annexe A.V.2** present the individual peak identification according to # PDF-2-2003 database, JCPDS/ICCD: 5-586 ($CaCO_3$, calcite); 41-1475 ($CaCO_3$, aragonite) and literature [66, 75, 103].

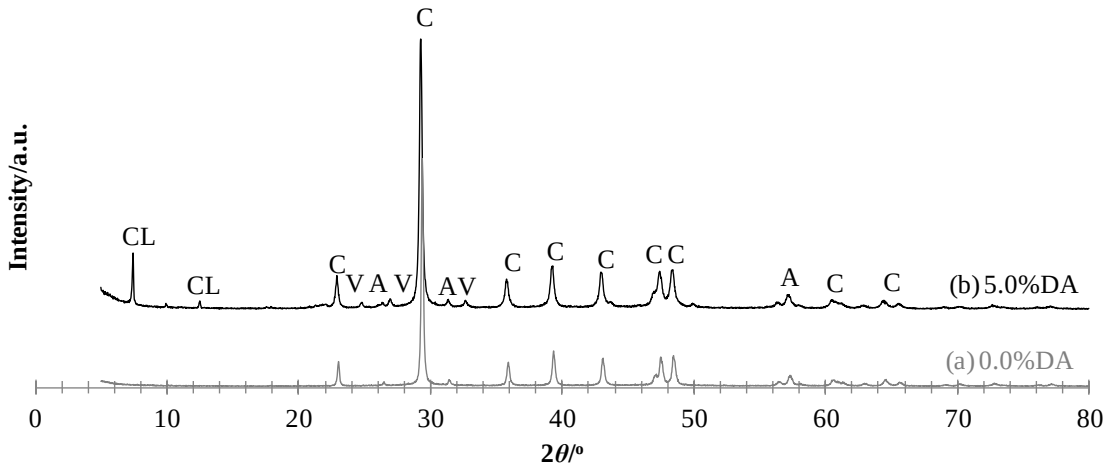

Figure 7.5 – Stacked XRD patterns obtained for $CaCO_3$ 0.0% **(a)** and 0.5% DA **(b)** powders. Principal peak identification. Legend: C-calcite; A-aragonite; V-vaterite; and CL-calcium laurate.

It could be concluded that calcite (rhombohedral symmetry) and aragonite (orthorhombic crystal system) were presented on the $CaCO_3$ with 0.0% DA synthesized powder.

In turn the X-ray powder diffractogram collected on $CaCO_3$ sample with 5.0% DA showed the presence of calcite, vaterite (hexagonal symmetry) and aragonite, three possible structures for this compound. Moreover, one of the most important peaks on this pattern was $2\theta = 7{,}423^{o}$. According to Sarkar *et al.* [66, 75] it corresponds to the calcium laurate structure which proved the crystalline salt ($Ca(C_{12}H_{23}O_2)_2$) presence. This fact was also observed on the ATR spectrum (**Figure 7.4 (a)**) and by the sharp morphology obtained on the SEM images (this topic will be discussed on the following chapter).

7.5 Scanning Electron Microscopy

On **Figure 7.6** the SEM images collected on the calcium carbonate particles functionalized with 0.0% and 5.0% of dodecanoic acid, respectively, can be seen.

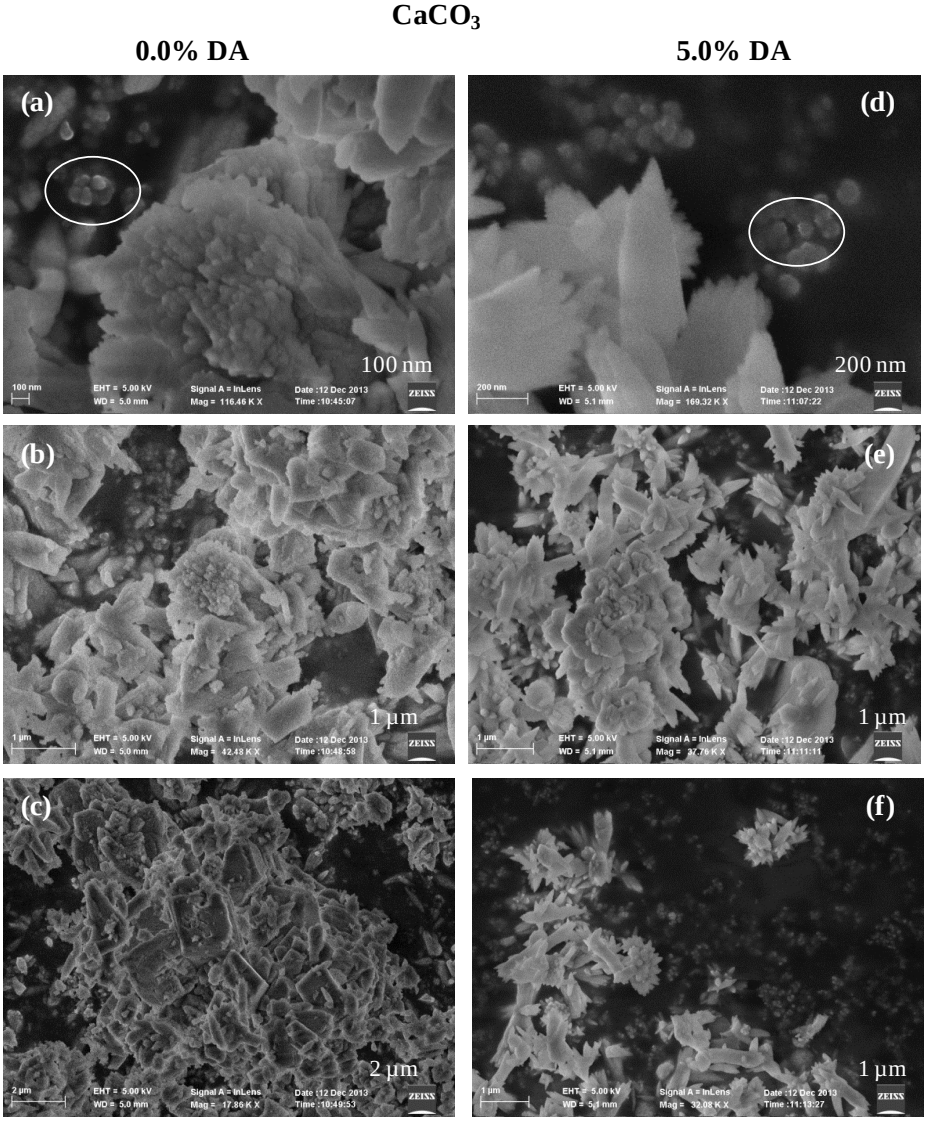

Figure 7.6 – SEM images on $CaCO_3$ with 0.0% **(a, b, c)** and 5.0% **(d, e, f)** DA powders.

Based on these images it could be concluded that for the 0.0% DA sample (**Figure 7.6** (**a**, **b** and **c**)) something-like polymorphous clusters were present. These objects, according to the previous results, should be composed by a combination of calcite and aragonite and/or polymorphs materials. However, these items are bigger than nano-sized particles, being non-homogeneous even on their grain size.

For the 5.0% DA $CaCO_3$ powder (**Figure 7.6** (**d, e** and **f**)) it could be seen that an evident morphology change occurred due the dodecanoic acid presence. The

polymorphous morphology changed to a sharp and pointed one. In this case, population was well distributed and with a small presence of, probably, nanoparticles.

In general, it could be concluded that there was no significant amount of calcium carbonate nanoparticles in the synthesized powders. On both cases (0.0% and 5.0% DA) small populations (in the white circles - **Figure 7.6 (a)** and **(d)**) that possibly are nano-objects were observed. However its amount was not enough to admit that the synthesis was well achieved, not leading to the production of enough contents of nanomaterials.

The morphology of the crystals ascertained by SEM images together with the diffraction patterns obtained by XRD allowed to state that DA has promoted a morphologic change from (something-like) calcite and/or aragonite to rosette shaped aragonite particles. Probably these rosette shaped particles were comprised of an aggregation of nano-aragonite rods explained by the aragonite needles tendency to aggregate and form this kind of rosettes structures. A similar morphology of aragonite has been reported by Sarkar *et al.* [66, 75]. Finally, DA complexed with the calcium ions yielding calcium laurate, which acted as a seed agent to nucleate, preferentially, aragonite instead of calcite.

8 CONCLUSIONS

First of all it is important to note that the obtained results were different from the ones that were expected. In fact it was proved that the followed route was not able, under the specific applied conditions, to produce enough nanoparticles capable of reaching the proposed goal.

Results from the visual analysis dispersions and turbidimetry technique ($CaCO_3$ and $Ca(OH)_2$ with 0.0, 0.5, 1.5, 2.0 and 5.0% of dodecanoic acid dispersed in cyclohexane) were in concordance. Both results proved the instability, at least not the necessary one, of the dispersions. However and based in all the accomplished tests cyclohexane proved to be the best solvent from the studied set.

Based on these results and according to other ongoing works in the group, the following studies were made on 0.0% and 5.0% DA calcium carbonate particles. According to ATR spectra, XRD patterns and SEM images it could be concluded that the reaction without any acid content was effective. It could be seen that calcite and aragonite structures were present but the nanoparticles amount was not significant. About the reaction with 5.0% DA the nanoparticles amount was again non-significant but the introduction of this organic fatty acid induced enormous morphology and crystallography changes on the $CaCO_3$ particles. After the functionalization the powder showed the presence of calcite, vaterite, aragonite and the carboxylic acid salt (calcium laurate). It was evident the morphologic change to rosette shaped particles.

Moreover, in both cases, the reduced amount of nano-objects can, probably, justify the non-stability dispersions.

Chemically the dodecanoic acid changes are very interesting. However this $CaCO_3$ functionalized powders are not useful for the main goal once the amount of nanoparticles was so reduce that the dispersed particles would not penetrate deeply inside the surface (due to their size). Therefore the powders would not be very effective against the internal acidity of the paper.

9 FUTURE WORK AND SIGNIFICANCE

Patina evaluation is one of the best ways to do the evaluation on the conservation state of antique coins. First of all and taking advantage of the used techniques an examination on the coins cross-section by SEM/EDS would be helpful in order to study the coin stratification and constitution (patina and bulk). The use of other techniques such as Radio Frequency Glow Discharge (rf-GD-OES) in order to analyze the depth profiling (less evasive than cross-section) or Raman spectroscopy for the organic compounds, evaluations would be also interesting. However, all of these proposals involve destruction of the matrix under study. A detailed research and study on the ore provenance would also be very interesting. It was tried to study the ore origin however due the coins antiquity this information would required more time and resources. An interdisciplinary approach in order to understand the ore derivation and the consequent soil study would be recommendable.

Nanomaterials for art and heritage conservation play an important role in the field of paper conservation. In fact, they are the future due the enormous interest in protect and treat the old papers and prevent the new one´s deterioration. Its operating costs have great potential even for big scale applications. It would be very interesting to see the made dispersions application and their characterization results, according to the exposed methodology. It would be the most effective form to confirm all the obtained and exposed results. As future work it is advisable the improvement of the proposed synthesis. Ameliorate parameters such as: make sure that the environment inside the synthesis flask is rich in carbon dioxide; a high and effective control on the reactants concentrations, maybe varying its proportions; as well as, a greater temperature control during the reactions, since this is a key point in the nanoparticles´ formation. This would help obtaining a more accurate model in order to create reduced particles size. It would also be beneficial experiment other non-polar organic solvents for the dispersions. Obtaining a better synthesis and understanding its dispersions, especially relatively on particle size, would further improve the results.

10 BIBLIOGRAPHY AND WEBGRAPHY

[1] Vaz, J.F. (1969). *Book of the coins of Portugal I*. Braga.

[2] Reale, R., Plattner, S.H., Guida, G., Sammartino, M.P., Visco, G. (2012). Ancient coins: cluster analysis applied to find a correlation between corrosion process and burial soil characteristics. *Chemistry Central Journal*, **6** (Suppl 2):S9.

[3] Hajivaliei, M., Nadooshan, F.K. (2012). Compositional study of Parthian silver coins using PIXE technique. *Nuclear Instruments and Methods in Physics Research B*, **289**, 56-58.

[4] Daraban, L., Cosma, C., Fiat, T. (1995). X-ray fluorescence analysis of some roman silver coins. *Journal of Radioanalytical and Nuclear Chemistry*, **201** (5), 447-457.

[5] Ingo, G.M., Caro, T., Padeletti, G., Chiozzini, G. (2004). Microchemical investigation on Renaissance coins minted at Gubbio (Central Italy). *Applied Physics A*, **79**, 319-325.

[6] http://www.moedanumismatica.com/coins/portugal.html (accessed on 18 Mar, 2014).

[7] https://www.incm.pt/portal/incm_hcm.jsp (accessed on 9 May, 2014).

[8] http://www.uc.pt/sobrenos/historia (accessed on 9 May, 2014).

[9] Walaszek, D., Senn, M., Faller, M., Philippe, L., Wagner, B., Bulska, E., Ulrich, A. (2013). Metallurgical and chemical characterization of copper alloy reference materials within laser ablation inductively coupled plasma mass spectrometry: Method development for minimally-invasive analysis of ancient bronze objects. *Spectrochimica Acta Part B*, **79–80**, 17-30.

[10] Guerra, M.F. (1995). Elemental analysis of coins and glasses. *Applied Radiation and Isotopes*, **46** (6/7), 583-588.

[11] Caridi, F., Torrisi, L. Cutroneo, M., Barreca, F., Gentile, C., Serafino, T., Castrizio, D. (2013). XPS and XRF depth patina profiles of ancient silver coins. *Applied Surface Science*, **272**, 82-87.

[12] Guerra, M.F., Barrandon, J.N., Magro, F., Gil., F.B. (1989). Analyse de dinheiros de la Ière dysnastie du Portugal: nouvelles approches. *Revue d´Archéomértrie*, **13**, 31-41.

[13] Martins, C.M.B., Martins, J.I. (2009). Mecanismo de corrosão em numismas de época romana provenientes da Senhora do Castelo. *Corrosão e Protecção de Materiais*, **28** (4), 126-133.

[14] Martins, C.M.B., Martins, J.I., Ferreira, J.A. (2010). Análise dos produtos de corrosão de uma moeda medieval procedente do Monte da Sehnora do Castelo. *Corrosão e Protecção de Materiais*, **29** (2), 49-54.

[15] Martins, C.M.B., Martins, J.I. (2011). Identification of corrosion products on a medieval copper-silver coin. *Protection of Metals and Physical Chemistry of Surfaces*, **47** (1), 128-132.

[16] Mata, A.L., Salta, M., Neto, M., Mendonça, M.H., Fonseca, I.T. (2009). Caracterização de uma moeda Portuguesa proveniente de uma Villa Romana de São Pedro, em Fronteira (Alentejo, Portugal). *Corrosão e Protecção de Materiais*, **28** (4), 114-119.

[17] Mata, A.L., Carneiro, A., Neto, M., Proença, L.A., Salta, M.M., Mendonça, M.H., Fonseca, I. (2010). Characterisation of five coins from the archaeological heritage of Portugal. *Journal of Solid State Electrochemistry*, **14**, 495–503.

[18] Wallinder, I.O., Zhang, X., Goidanich, S., Bozec, N., Herting, G., Leygraf, C. (2014). Corrosion and runoff rates of Cu and three Cu-alloys in marine environments with increasing chloride deposition rate. *Science of the Total Environment*, **472**, 681-694.

[19] Antonijevic, M.M., Milic, S.M., Petrovic, M.B. (2009). Films formed on copper surface in chloride media in the presence of azoles. *Corrosion Science*, **51**, 1228-1237.

[20] Qin, T.T., Li, J., Luo, H.Q., Li, M., Li, N.B. (2011). Corrosion inhibition of copper by 2,5-dimercapto-1,3,4-thiadiazole monolayer in acidic solution. *Corrosion Science*, **53**, 1072-1078.

[21] Pernicka, E. (1999). Trace element fingerprint of ancient copper: a guide to technology or provenance? *Metals in Antiquity, BAR international series*, **792**, 163-171.

[22] Gorghinian, A., Esposito, A., Ferretti, M., Catalli, F. (2013). XRF analysis of Roman Imperial coins. *Nuclear Instruments and Methods in Physics Research B*, **309**, 268-271.

[23] Moreno-Suárez, A.I., Gómez-Tubío, B., Respaldiza, M.A., Chaves, F., Ortega-Feliu, I., Ontalba-Salamanca, M.A., Ager, F.J. (2011). Combining

non-destructive nuclear techniques to study Roman leaded copper coins from Ilipa (II–I centuries B.C.). *Nuclear Instruments and Methods in Physics Research B*, **269**, 3098-3101.

[24] Mousser, H., Amri, R., Madani, A., Darchen, A., Mousser, A. (2011). Microchemical surface analysis of two Numidian coins. *Applied Surface Science*, **257**, 5961-5965.

[25] Bray, P.J., Pollard, A.M. (2012). A new interpretative approach to the chemistry of copper-alloy objects: source, recycling and technology. *Antiquity Publication Ltd.*, **86**, 853-867.

[26] Constantinides, I., Adriaens, A., Adams, F. (2002). Surface characterization of artificial corrosion layers on copper alloy reference material. *Applied Surface Science*, **189**, 90-101.

[27] He, L., Liang, J., Zhao, X., Jiang, B. (2011). Corrosion behavior and morphological features of archeological bronze coins from ancient China. *Microchemical Journal*, **99**, 203-212.

[28] Robbiola, L., Blengino, J.M., Fiaud, C. (1998). Morphology and mechanisms of formation of natural patinas on archaeological Cu-Sn alloys. *Corrosion Science*, **39** (12), 2083-2011.

[29] Robbiola, L., Portier, R. (2006). A global approach to the authentication of ancient bronzes based on the characterization of the alloy–patina–environment system. *Journal of Cultural Heritage*, **7**, 1-12.

[30] Ingo, G.M., Caro, T., Riccucci, C., Khosroff, S. (2006). Uncommon corrosion phenomena of archaeological bronze alloys. *Applied Physics A*, **83**, 581-588.

[31] Ager, F.J., Moreno-Suárez, A.I., Scrivano, S., Ortega-Feliu, I., Gómez-Tubío, B., Respaldiza, M.A. (2013). Silver surface enrichment in ancient coins studied by micro-PIXE. *Nuclear Instruments and Methods in Physics Research B*, **306**, 241-244.

[32] Linke, R., Schreiner, M. (2000). Energy dispersive X-ray fluorescence analysis and X-ray microanalysis of medieval silver coins. An analytical approach for non-destructive investigation of corroded metallic artifacts. *Mikrochimica Acta*, **133**, 165-170.

[33] Beck, L., Bosonnet, S., Réveillon, S., Eliot, D., Pilon, F. (2004). Silver surface enrichment of silver–copper alloys: a limitation for the analysis of ancient silver

coins by surface techniques. *Nuclear Instruments and Methods in Physics Research B*, **226**, 153–162.

[34] Pitarch, A., Queralt, I. (2010). Energy dispersive X-ray fluorescence analysis of ancient coins: The case of Greek silver drachmae from the Emporion site in Spain. *Nuclear Instruments and Methods in Physics Research B*, **268**, 1682-1685.

[35] Gerwin, W., Baumhauer, R. (2000). Effect of soil parameters on the corrosion of archaeological metal finds. *Geoderma*, **96**, 63-80.

[36] Nord, A.G., Mattsson, E., Tronner, K. (2005). Factors influencing the long-term corrosion of bronze artefacts in soil. *Protection of Metals*, **41** (4), 309-316.

[37] Wiesinger, R., Martina, I., Kleber, Ch., Schreiner, M. (2013). Influence of relative humidity and ozone on atmospheric silver corrosion. *Corrosion Science*, **77**, 69-76.

[38] Samie, F., Tibdlab, J., Kucera, V., Leygraf, C. (2007). Atmospheric corrosion effects of HNO_3-Comparison of laboratory-exposed copper, zinc and carbon steel. *Atmospheric Environment*, **41**, 4888-4896.

[39] Oesch, S., Faller, M. (1997). Environmental effects on the materials: the effect of the air pollutants SO_2, NO_2, NO and O_3 on the corrosion of copper, zinc and aluminium. A short literature survey and results of laboratory exposures. *Corrosion Science*, **39** (9), 1505-1530.

[40] Kratschmer, A., Wallinder, I.O., Leygraf, C. (2002). The evolution of outdoor copper patina. *Corrosion Science*, **44**, 425-450.

[41] Picciochi, R., Ramos, A.C., Mendonça, M.H., Fonseca, I.T.E. (2004). Influence of the environment on the atmospheric corrosion of bronze. *Journal of Applied Electrochemistry*, **34**, 989-995.

[42] Kleber, Ch., Weissenrieder, J., Schreiner, M., Leygraf, C. (2002). Comparison of the early stages of corrosion of copper and iron investigated by in situ TM-AFM. *Applied Surface Science*, **193**, 245-253.

[43] Aastrup, T. (1999). *In situ investigations of the metal/atmosphere interface. Influence of humidity, sulfur dioxide, ozone and nitrogen dioxide on copper*. Doctoral Thesis. Department of Materials Science and Engineering, Division of Corrosion Science, Royal Institute of Technology (Sweden).

[44] Zhang, X., Wallinder, I.O., Leygraf, C. (2014). Mechanistic studies of corrosion product flaking on copper and copper-based alloys in marine environments. *Corrosion Science*, **85**, 15-25.

[45] Kear, G., Barker, B.D., Walsh, F.C. (2004). Electrochemical corrosion of unalloyed copper in chloride media—a critical review. *Corrosion Science*, **46**, 109-135.

[46] Fitzgerald, K.P., Nairn, J., Atrens, A. (1998). The chemistry of copper patination. *Corrosion Science*, **40** (12), 2029-2050.

[47] Tansug, G., Tuken, T., Giray, E.S., Findikkiran, G., Sigircik, G., Demirkol O., Erbil, M. (2014). A new corrosion inhibitor for copper protection. *Corrosion Science*, **84**, 21-29.

[48] Chen, Z., Huang, L., Zhang, G., Qui, Y., Guo, X. (2012). Benzotriazole as a volatile corrosion inhibitor during the early stage of copper corrosion under adsorbed thin electrolyte layers. *Corrosion Science*, **65**, 214-222.

[49] Sherif, E.S.M., Erasmus, R.M., Comins, J.D. (2008). Inhibition of copper corrosion in acidic chloride pickling solutions by 5-(3-aminophenyl)-tetrazole as a corrosion inhibitor. *Corrosion Science*, **50**, 3439–3445.

[50] http://www.paperonline.org/history-of-paper (accessed on 2 Oct, 2013).

[51] Manso, M., Carvalho, M.L. (2009). Application of spectroscopic techniques for the study of paper documents: A survey. *Spectrochimica Acta Part B*, **64**, 482-490.

[52] http://www.hqpapermaker.com/paper-history/ (accessed on 2 Oct, 2013).

[53] Adams, J. (2011). Analysis of printing and writing papers by using direct analysis in real time mass spectrometry. *International Journal of Mass Spectrometry*, **301**, 109-126.

[54] Giorgi, R., Dei, L., Ceccato, M., Schettino, C., Baglioni, P. (2002). Nanotechnologies for conservation of cultural heritage: Paper and canvas deacidification. *Langmuir*, **18** (21), 8198-8203.

[55] Area, M.C., Cheradame, H. (2011). Paper aging and degradation: recent findings and research methods. *BioResources*, **6** (4), 5307-5337.

[56] Baglioni, P., Chelazzi, D. (2013). *Nanoscience for the conservation of works of art*. 1st ed. Cambridge, UK: RSC Nanoscience and Tecnology.

[57] http://antoine.frostburg.edu/chem/senese/101/consumer/faq/what-is-cellulose.shtml (accessed on 3 Oct, 2013).

[58] Baty, J.W., Maitland, C.L., Minter, W., Hubbe, M.A., Jordan-Mowery, S.K. (2010). Deacidification for the conservation and preservation of paper based works: A review. *BioResources*, **5** (3), 1955-2023.

[59] http://www.ipst.gatech.edu/faculty/ragauskas_art/technical_reviews/Lignin%20Overview.pdf (accessed on 28 Jan, 2014).

[60] Seery, M. (2013). Saving paper, Education in Chemistry, http://www.rsc.org/eic/ .

[61] Potthast, A., Henniges, U., Banik, G. (2008). Iron gall ink-induced corrosion of cellulose: aging, degradation and stabilization. Part 1: model paper studies. *Cellulose*, **15**, 849-859.

[62] Poggi, G., Giorgi, R., Toccafondi, N., Katzur, V., Baglioni, P. (2010). Hydroxide nanoparticles for deacidification and concomitant inhibition of iron gall ink corrosion of paper. *Langmuir*, **26** (24), 19084-2909.

[63] Baglioni, P., Giorgi, R. (2006). Soft and hard nanomaterials for restoration and conservation of cultural heritage. *Soft Matter*, **2**, 293-303.

[64] Henniges, U., Reibke, R., Banik, G., Huhsmann, E., Hahner, U., Prohaska, T., Potthast, A. (2008). Iron gall ink-induced corrosion of cellulose: aging, degradation and stabilization. Part 2: application on historic sample material. *Cellulose*, **15**, 861-870.

[65] Giorgi, R., Bozzi, C., Dei, L., Gabbiani, C., Ninham, B.W., Baglioni, P. (2005). Nanoparticles of $Mg(OH)_2$: synthesis and application to paper conservation. *Langmuir*, **21** (18), 8495-8501.

[66] Sarkar, A., Mahapatra, S. (2012). Mechanism of unusual polymorph transformations in calcium carbonate: dissolution-recrystallization vs additive-mediated nucleation. *Journal of Chemical Sciences*, **124** (6), 1399-1404.

[67] http://www.webmineral.com/ (accessed on 10 Feb, 2014).

[68] Chen, Y., Ji, X., Zhao, G., Wang, X. (2010). Facile preparation of cubic calcium carbonate nanoparticles with hydrophobic properties via a carbonation route. *Powder Technology*, **200**, 144-148.

[69] Gupta, R. (2004). *Synthesis of precipitated calcium carbonate nanoparticles using modified emulsion Membranes*. Master Thesis. Georgia Institute of Technology (USA).

[70] Sargheini, J., Ataie A., Salili, S.M., Hoseinion, A.A. (2012). One-step facile synthesis of $CaCO_3$ nanoparticles via mechano-chemical route. *Powder Technology*, **219**, 72-77.

[71] Wang C., S. Y.-B. (2007). A novel aqueous-phase route to synthesize hydrophobic $CaCO_3$ particles in situ. *Materials Science and Engineering C*, **27**, 42-45.

[72] Zhang, Z., Gao,D., Zhao, H., Xie, C., Guan, G., Wang, D., Hong Yu, S. (2006). Biomimetic assembly of polypeptide-stabilized $CaCO_3$ nanoparticles. *Journal of Physical Chemistry B*, **110** (17), 8613-8618.

[73] CSID: 3756, http://www.chemspider.com/Chemical-Structure.3756.html (accessed on 25 Jan, 2014).

[74] http://www.thefreedictionary.com/dodecanoic+acid (accessed on 28 Jan, 2014).

[75] Sarkar, A., Ghosh, A.K., Mahapatra, S. (2012). Lauric acid triggered in situ surface modification and phase selectivity of calcium carbonate: its application as an oil sorbent. *Journal of Materials Chemistry*, **22** (6), 11113–11120.

[76] Lee, L.R. (1996). *Investigation into the occurrence of 'black spot' corrosion on copper alloy objects in the British Museum*. Department of Conservation from the British Museum, London.

[77] Weichert, M., Eggert, G., Jones, A.M., Ankersmit, H.A. (2004). *Trees, brunches, cauliflowers - a closer look at sulphuruous corrosion on copper alloys and minerals ("balck spots")*. National Museum of Australia Canberra ACT, 149-159.

[78] http://www.britannica.com/EBchecked/topic/409243/nephelometry-and-turbidimetry#ref100635 (accessed on 26 Nov, 2013).

[79] Harvey,D. (2000). *Modern Analytical Chemistry*. 1st ed. International edition: The McGraw-Hill Companies.

[80] http://quizlet.com/5275979/instrumentation-flash-cards/ (accessed on 10 Dec, 2013).

[81] http://www.azom.com/article.aspx?ArticleID=5958 (accessed on 11 Dec, 2013).

[82] Setnicka, V.. *FT-IR Reflection Techniques. Overview – Main Principles of Reflection Techniques*.

[83] Beasley, M.M., Bartelink, E.J., Taylor, L., Miller, R.M. (2014). Comparison of transmission FTIR, ATR, and DRIFT spectra: implications for assessment of bone bioapatite diagenesis. *Journal of Archaeological Science*, **46**, 16-22.

[84] Perkin Elmer® Precisely (2005). *Technical Note: FT-IR Spectroscopy. FT-IR spectroscopy Attenuated Total Reflectance (ATR)*. Shelton, USA: PerkinElmer Life and Analytical Sciences (www.perkinelmer.com).

[85] PIKE Technologies (2011). *Application Note: ATR-Theory and Applications*. Madison (Wisconsin), USA: PIKE Technologies (www.piketech.com).

[86] Bruker AXS Microanalysis (2010). *M4 Tornado, High performance micro-XRF spectrometer. Physical principles of Micro-X-ray Fluorescence*. Berlin, Germany: Bruker AXS Microanalysis GmbH.

[87] Marguí, E., Grieken, R.V. (2013). *X-ray fluorescence spectrometry and related techniques: an introduction*. 1st ed. New York, USA: Momentum Press.

[88] Pessanha, A.S. (2013). *Non-destructive characterization of artworks in paper support using spectroscopic techniques*. Doctoral Thesis. Physics Department, Faculty of Sciences, University of Lisbon (Portugal).

[89] Skoog, D.A., West, D.M. Holler, F.J., Crouch, R.S. (2004). *Fundamentals of Analytical Chemistry*. 9th ed. USA: Thomson, Brooks/Cole.

[90] Guilherme A.N. (2013). *Spectroscopy techniques for characterizing Portuguese glazed ceramics: a contribution to the study of ancient faiences from Coimbra*. Doctoral Thesis. Physics Department, Faculty of Sciences, University of Lisbon (Portugal).

[91] http://www.horiba.com/us/en/scientific/products/x-ray-fluorescence-analysis/tutorial/penetration-depths/ (accessed on 13 Aug, 2013).

[92] Krull, U.J., Thompson, M., *Encyclopaedia of Physical Science and Technology. Analytical Chemistry*. Chapter: *X-ray analysis*. (Ron, J.; pages 887-902). 3rd ed. University of Toronto, Canada.

[93] West, A.R. (1999). *Basic Solid State Chemistry*. 2nd ed.: Student edition, John Wiley & Sons.

[94] Settle, F. (1997). *Handbook of Instrumental Techniques for Analytical Chemistry*. New Jersey, USA: Prentice Hall, Inc.

[95] Skoog, D.A., Holler, F.J., Nieman, T.A. (1992). *Principles of instrumental analysis.* 5th ed. Madrid, Spain.

[96] http://serc.carleton.edu/research_education/geochemsheets/techniques/SEM.html (accessed on 17 Dec, 2013).

[97] http://www.ammrf.org.au/myscope/sem/background/#term (accessed on 17 Dec, 2013).

[98] http://www.ammrf.org.au/myscope/sem/background/ (accessed on 17 Dec, 2013).

[99] Custódio, P.J., Carvalho, M.L., Nunes, F., Pedroso, S., Campos, A. (2005). Direct analysis of human blood (mothers and newborns) by energy dispersive X-ray fluorescence. *Journal of Trace Elements in Medicine and Biology*, **19**, 151-158.

[100] Silva, R.B, Bulska, E., Godlewsksa Zylkiewicz, B., Hedrich, M., Majcen, N., Magnusson, B., Marincic, S., Papadakis, I., Patriarca, M., Vassileva, E., Taylor, P. (2012). *Analytical measurement: measurement uncertainty and statics*. Geel, Belgium. European commission. Join Research Centre. Institute for Reference Materials and Measurements.

[101] Oliveira, M.I. (2011). *Determinação de metais pesados em cosméticos*. Bachelor Thesis. Chemical and Biochemical Department, Faculty of Sciences, University of Lisbon (Portugal).

[102] Miller, J. N., Miller J. C (2005). *Statistics and chemometrics for analytical chemistry*. 5th ed. London: Pearson Prentice Hall.

[103] http://rruff.info/ (accessed several times, 2014).

[104] Miller, F.A., Wilkins, C.H. (1952). Infrared spectra and characteristic frequencies of inorganic ions, their use in qualitative analysis. *Analytical chemistry*, **24** (8), 1253-1294.

[105] Gunasekaran, S., Anbalagan, G., Pandi, S. (2006). Raman and infrared spectra of carbonates of calcite structure. *Journal of Raman Spectroscopy*, **37**, 892-899.

[106] Bruker Oprics (2009). *Guide for Infrared Spectroscopy*. Analytical, life science, process, Bruker Optics (www.brukeroptics.com).

ANNEXES

Annexe I

DEFINITIONS

1. *Numismatics* - science that studies coins in their essence, origin and expansion by internal and external trade.

2. *Cold working process* – plastic deformation below the recrystallization temperature, at room temperature.

3. *Annealing* – by heating the material and then slowly cool it to room temperature.

4. *Smelting* – process to convert a substance or ore to its purest form by chemical reactions.

5. *Re-melting* - process of changing a substance from solid to liquid form, by heating. In copper alloys this process results in a loss of certain of the included elements through oxidation, particularly arsenic and antimony [21].

6. *Sizing* – introduction of a substance to paper in order to change its surface properties, e.g. to improve strength or reduce absorbency of water. Generally "papermaker's alum" (or alum-rosin), an acidic hydrated aluminium sulphate ($Al_2(SO_4)_3$**.**xH_2O, where x=16 or 18) was added to early paper made from wood pulp, to harden and to help the gelatine sizing, making the paper somewhat water resistant so that inks did not "run" or spread uncontrollably. Synthetic sizing agents as alkyl ketene dimer used industrially to improve hydrophobicity in paper and alkenyl succinic anhydride as a wet strength additive in paper are nowadays used.

7. *Fenton mechanism* – consists on the oxidation of an organic substrate by iron (II) and hydrogen peroxide. On this case the stability of the iron-gall ink complex is governed by the ratio between Fe (II) ions and tanning agent. The free Fe^{2+} ions present in the system act in redox reactions, usually catalyzing cellulose oxidation through a free radical mechanism, leading to the this mechanism. This decomposition can be stopped by introducing a chelating agent to complexing the Fe (II) in the ink [60-64].

Annexe II

STATISTICS FOR ANALYTICAL CHEMISTRY AND METHOD EVALUATION

For a set of *n* values where x_i is the individual value of *x* the following parameters can be defined.

A.II.1 Mean

The mean value ($\bar{x}$) is the arithmetic average of all measurements results. If the sample is randomly taken then the average is the best estimate of the population mean. The mean value is given by **Equation A.II.1** [100]:

$$\bar{x} = \frac{1}{n}\sum_{i=1}^{n}(x_i) \qquad \textbf{Equation A.II.1}$$

A.II.2 Standard deviation, standard deviation of the mean and relative standard deviation

Standard deviation (SD) ($s(x_i)$) is the positive square root of the variance for (n-1) degrees of freedom. This is a useful concept to express the confidence of analytical instrumental response and it is given by **Equation A.II.2** [100]:

$$s(x_i) = \sqrt{\frac{1}{n-1}\sum_{i=1}^{N}(x_i - \bar{x})^2} \qquad \textbf{Equation A.II.2}$$

Standard deviation of the mean ($s(\bar{x_i})$) is an estimate of the standard deviation of the mean values that would arise if repeated samples were taken from the population (**Equation A.II.3**). Its value is smaller than the ($s(x_i)$) [100, 101].

$$s(\bar{x}_i) = \frac{s(x_i)}{\sqrt{n}} \qquad \textbf{Equation A.II.3}$$

The relative standard deviation or coefficient of variation (RSD or CV) is a measure of the spread of data in comparison to the data mean. It is obtained through the ratio between the sample standard deviation and its mean (**Equation A.II.4**) [100, 101]:

$$RSD = \frac{s(x_i)}{\bar{x}} \; or \; RSD(\%) = CV(\%) = \frac{100.\, s(x_i)}{\bar{x}} \qquad \textbf{Equation A.II.4}$$

This parameter quantifies the incidence of random errors in the analytical result. The smaller the RSD better reproducibility of the method, since the spread of results around the mean value is lower [101].

A.II.3 Uncertainty of the Limit of Detection

In order to calculate the combined standard uncertainty relative to the LOD value **Equations A.II.5** and **A.II.6** were follow [100, 102]:

$$\mathrm{LOD} = \frac{3\mathrm{c_i}\sqrt{\mathrm{N_b}}}{\mathrm{N_p}} \qquad \text{Equation 4.1}$$

$$\mathrm{u(LOD)} = \sqrt{(\frac{\mathrm{u_{c_i}}}{\mathrm{c_i}})^2 + (\frac{\mathrm{u_{N_b}}}{\mathrm{N_b}})^2 + (\frac{\mathrm{u_{N_p}}}{\mathrm{N_p}})^2}\ \mathrm{x\ LOD} \qquad \textbf{Equation A.II.5}$$

$$\mathrm{U(LOD)} = \mathrm{k.\, u(LOD)} \qquad \textbf{Equation A.II.6}$$

where u(LOD), $u(c_i)$, $u(N_b)$ and $u(N_p)$ are the relative standard uncertainties from LOD, the concentration of the element i, and the counting rates for the background and for the peak, respectively. U(LOD) is the combined standard uncertainty for the LOD value and k is the coverage factor, in this case, $k = 2$,for a confidence level of, approximately, 95%.

A.II.4 Method precision

The estimation of precision (uncertainty resulting from random errors) is performed by calculating the standard deviation, RSD or the variance of the sample [87, 101]. Precision describes the method reproducibility. Greater precision imply higher equipment reproducibility [101]. In practice the precision of the method can be improved by controlling the random errors introduced during sample preparation and by the analytical instrument [87].

Annexe III

DETAILED RESULTS PRESENTATION

EVALUATION ON THE DEGRADATION STATE OF ANTIQUE COINS BY SPECTROSCOPIC TECHNIQUES

A.III.1 μ-Energy Dispersive X-ray Fluorescence

Figures A.III.1 to **A.III.6** present the individual μ-EDXRF spectra and the respective peak attribution for each one of the studied *dinheiros.* **Tables A.III.1** to **A.III.6** show its respective elements quantification.

Table A.III.7 presents the detailed and statistical information about the quantifications obtained for full list of detected elements on the set of the studied coins.

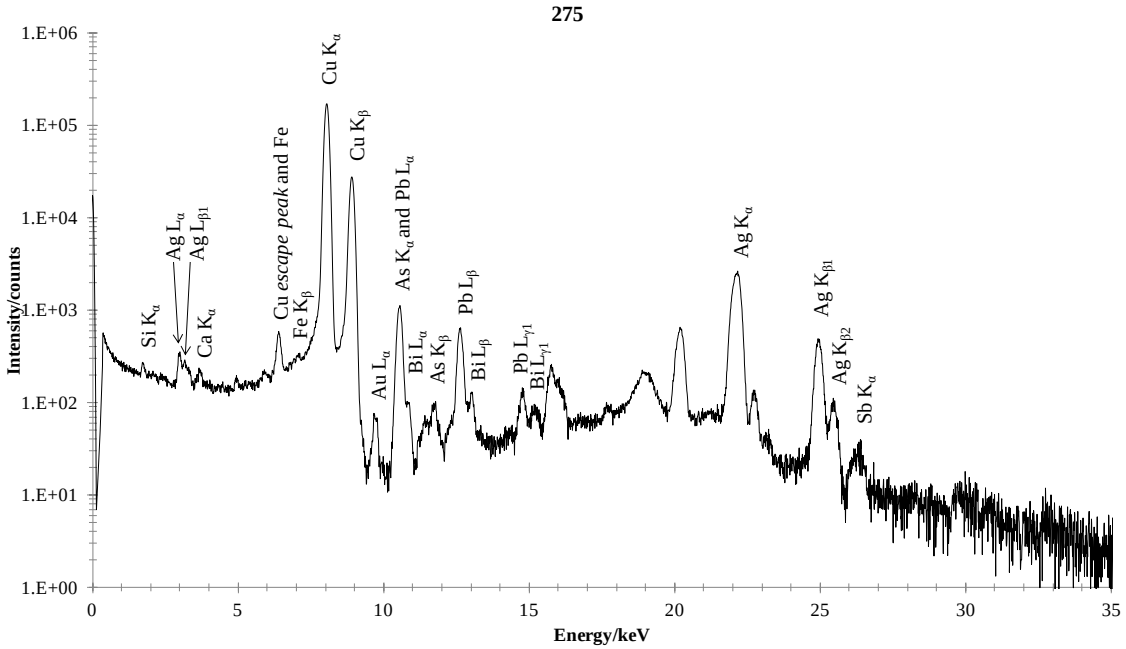

Figure A.III.1 – μ-EDXRF spectra obtained on 275 coin.

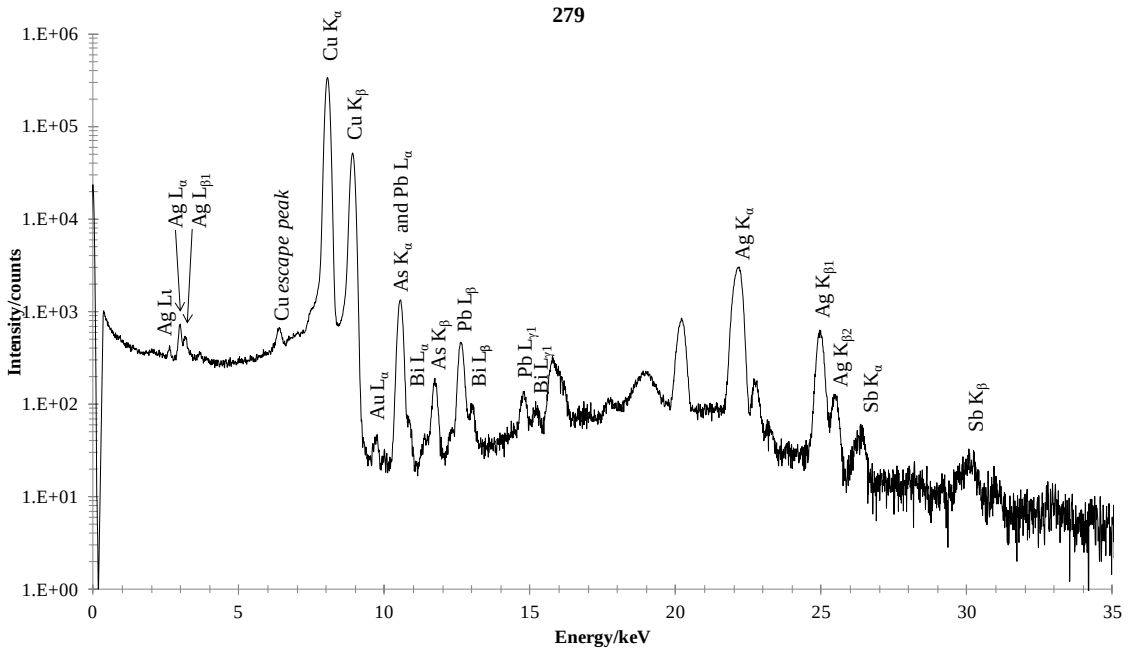

Figure A.III.2 – µ-EDXRF spectra obtained on 279 coin.

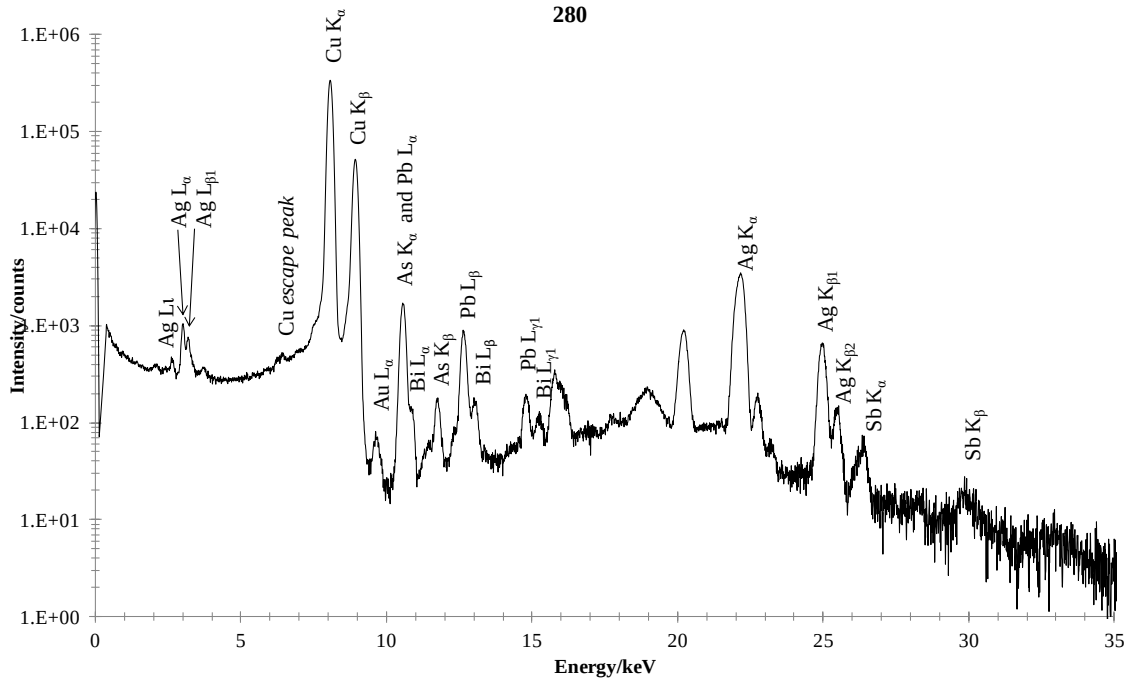

Figure A.III.3 – µ-EDXRF spectra obtained on 280 coin.

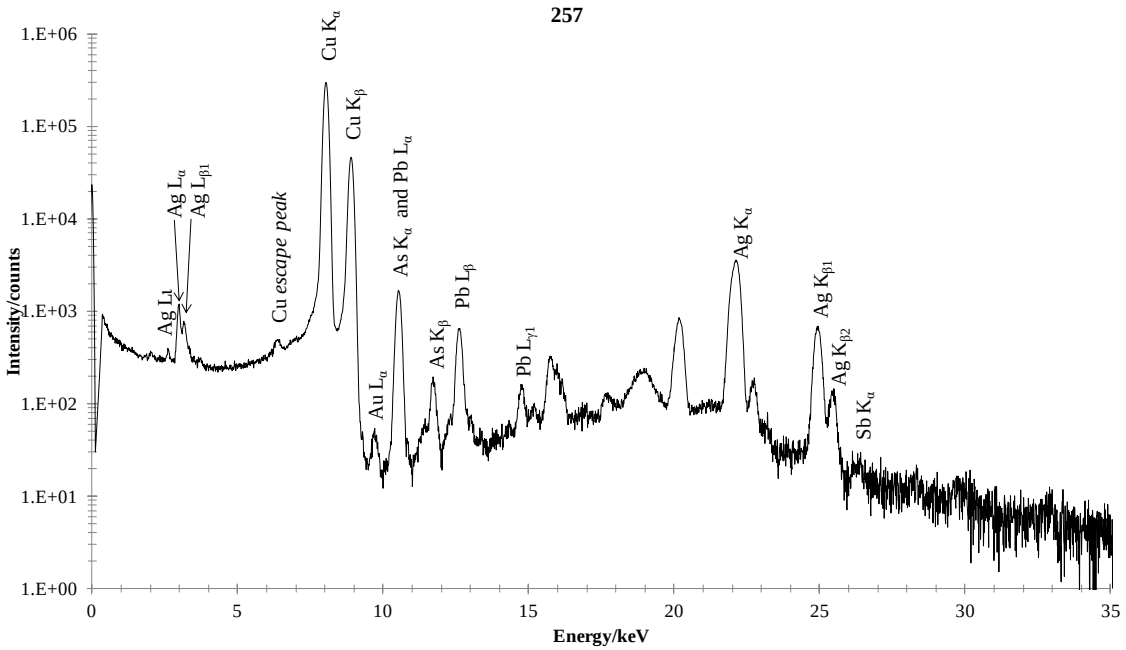

Figure A.III.4 – µ-EDXRF spectra obtained on 257 coin.

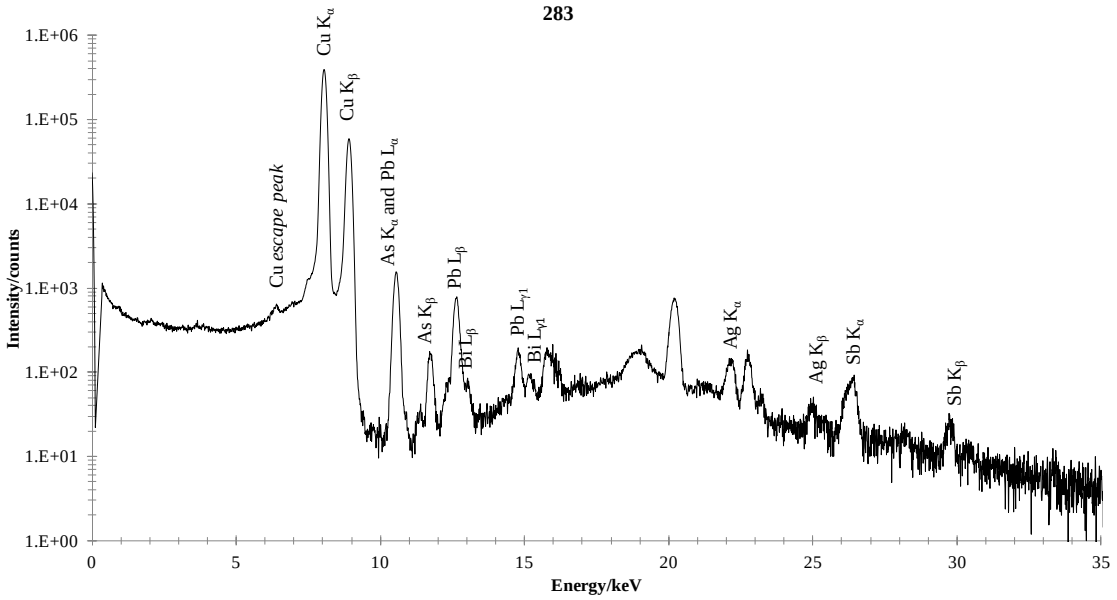

Figure A.III.5 – µ-EDXRF spectra obtained on 283 coin.

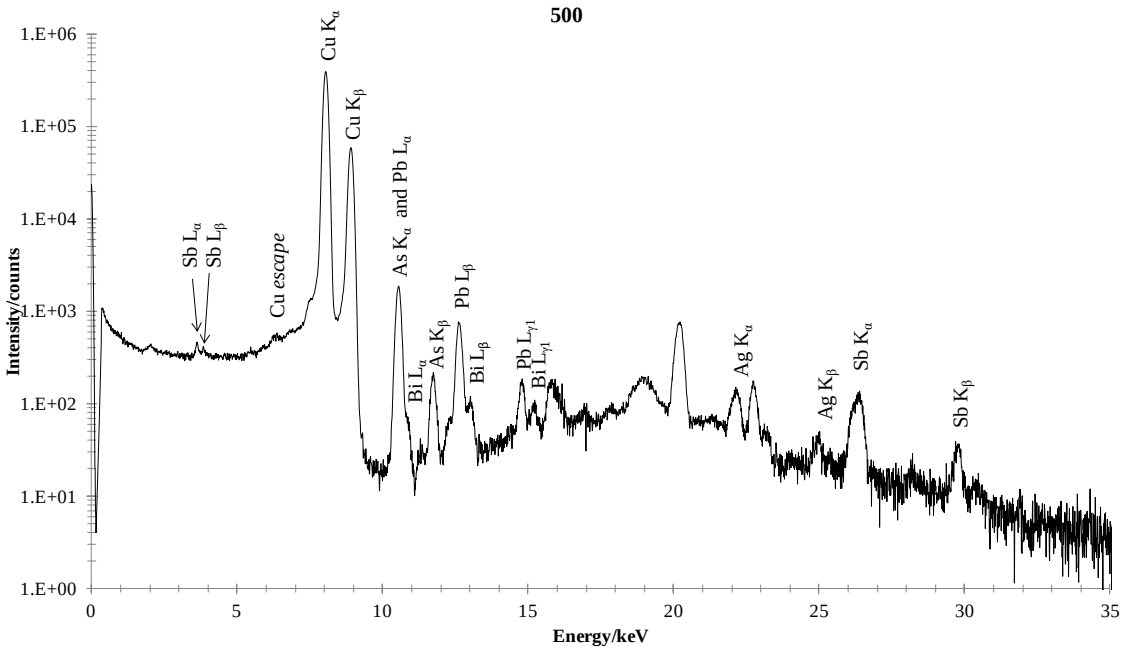

Figure A.III.6 – μ-EDXRF spectra obtained on 500 coin.

Table A.III.1 - μ-EDXRF quantification obtained on 275 coin.

	Element Quantification (wt.%)		
Cu	86.7	±	1.8
Ag	8.1	±	1.3
Si	2.18	±	0.65
Fe	0.833	±	0.508
Pb	0.56	±	0.33
P	0.41	±	0.15
As	0.37	±	0.16
Ca	0.296	±	0.097
Sb	0.231	±	0.047
K	0.23	±	0.25
Cl	0.168	±	0.199
S	0.08	±	0.11
Bi	0.055	±	0.026
Au	0.032	±	0.013

Table A.III.2 - μ-EDXRF quantification obtained on 279 coin.

	Element Quantification (wt.%)		
Cu	88.2	±	3.0
Ag	8.7	±	1.1
Si	0.94	±	1.70
Pb	0.54	±	0.26
As	0.39	±	0.13
Cl	0.34	±	0.22
Sb	0.315	±	0.031
Ca	0.24	±	0.41
Fe	0.18	±	0.37
Bi	0.051	±	0.027
Au	0.024	±	0.011

Table A.III.3 - μ-EDXRF quantification obtained on 280 coin.

	Element Quantification (wt.%)		
Cu	85.33	±	4.28
Ag	9.24	±	1.73
Ca	1.57	±	1.44
Pb	1.48	±	1.15
Cl	1.00	±	0.63
As	0.40	±	0.24
Sb	0.391	±	0.080
Si	0.21	±	0.44
Fe	0.20	±	0.19
Bi	0.091	±	0.041
Au	0.038	±	0.015

Table A.III.4 - μ-EDXRF quantification obtained on 257 coin.

	Element Quantification (wt.%)		
Cu	89.6	±	1.5
Ag	9.3	±	1.4
As	0.58	±	0.30
Pb	0.31	±	0.14
P	0.14	±	0.15
Cl	0.099	±	0.078
Sb	0.091	±	0.014
Ca	0.083	±	0.049
Fe	0.028	±	0.015
Au	$2.8x10^{-2}$	±	$9.8x10^{-3}$
Bi	$7.0x10^{-3}$	±	$1.8x10^{-3}$

Table A.III.5 - μ-EDXRF quantification obtained on 283 coin.

	Element Quantification (wt.%)		
Cu	96.2	±	3.4
Si	1.0	±	1.7
Pb	0.8	±	0.5
Sb	0.523	±	0.088
Fe	0.31	±	0.69
As	0.31	±	0.14
Cl	0.30	±	0.47
Ca	0.28	±	0.38
Ag	0.259	±	0.056
Bi	0.026	±	0.016

Table A.III.6 - μ-EDXRF quantification obtained on 500 coin.

	Element Quantification (wt.%)		
Cu	95.7	±	6.3
Ca	1.3	±	5.9
Pb	0.90	±	0.68
Sb	0.76	±	0.13
As	0.45	±	0.17
Si	0.26	±	0.72
Ag	0.242	±	0.048
Cl	0.17	±	0.29
P	0.11	±	0.20
Fe	0.09	±	0.24
Bi	0.045	±	0.034

Table A.III.7 – Detailed and statistical information about the μ-EDXRF quantifications on the set of the studied *dinheiros* (n.q. - non-quantified).

		Si	Cl	Ca	Ti	Fe	Cu	As	Ag	Sb	Au	Hg	Pb	Bi	Sr	P	K	S
275	$\bar{x}$	2.181	0.168	0.296	0.074	0.833	86.715	0.374	8.067	0.231	0.032	0.010	0.555	0.055	n.q.	0.411	0.231	0.085
	s	0.650	0.199	0.097	0.052	0.508	1.788	0.158	1.322	0.047	0.013	0.008	0.326	0.026	n.q.	0.147	0.249	0.112
	$s(\bar{x}_i)$	0.110	0.034	0.016	0.009	0.086	0.302	0.027	0.223	0.008	0.002	0.002	0.055	0.004	n.q.	0.033	0.056	0.025
	RSD/%	30%	118%	33%	69%	61%	2%	42%	16%	20%	39%	85%	59%	48%	n.q.	36%	108%	132%
	n	35	35	35	35	35	35	35	35	35	35	15	35	35	n.q.	20	20	20
279	$\bar{x}$	0.938	0.343	0.236	0.017	0.180	88.215	0.391	8.745	0.315	0.024	0.010	0.536	0.051	n.q.	n.q.	n.q.	n.q.
	s	1.698	0.219	0.411	0.017	0.368	3.028	0.131	1.099	0.031	0.011	0.012	0.261	0.027	n.q.	n.q.	n.q.	n.q.
	$s(\bar{x}_i)$	0.370	0.048	0.090	0.004	0.080	0.661	0.029	0.240	0.007	0.002	0.003	0.057	0.006	n.q.	n.q.	n.q.	n.q.
	RSD/%	181%	64%	174%	102%	205%	3%	34%	13%	10%	45%	124%	49%	53%	n.q.	n.q.	n.q.	n.q.
	n	21	21	21	21	21	21	21	21	21	21	21	21	21	n.q.	n.q.	n.q.	n.q.
280	$\bar{x}$	0.207	1.003	1.567	0.022	0.203	85.333	0.399	9.241	0.391	0.038	0.002	1.485	0.091	0.021	n.q.	n.q.	n.q.
	s	0.437	0.629	1.443	0.012	0.186	4.280	0.236	1.726	0.080	0.015	0.002	1.151	0.041	0.012	n.q.	n.q.	n.q.
	$s(\bar{x}_i)$	0.117	0.168	0.386	0.003	0.050	1.144	0.063	0.461	0.021	0.004	0.000	0.308	0.011	0.004	n.q.	n.q.	n.q.
	RSD/%	212%	63%	92%	56%	92%	5%	59%	19%	20%	38%	91%	78%	46%	56%	n.q.	n.q.	n.q.
	n	14	14	14	14	14	14	14	14	14	14	14	14	14	10	n.q.	n.q.	n.q.
257	$\bar{x}$	n.q.	0.099	0.083	n.q.	0.028	89.563	0.578	9.291	0.091	0.028	0.014	0.305	0.007	n.q.	0.137	n.q.	n.q.
	s	n.q.	0.078	0.049	n.q.	0.015	1.520	0.304	1.384	0.014	0.010	0.004	0.142	0.002	n.q.	0.147	n.q.	n.q.
	$s(\bar{x}_i)$	n.q.	0.021	0.035	n.q.	0.004	0.406	0.081	0.370	0.004	0.003	0.004	0.038	0.001	n.q.	0.085	n.q.	n.q.
	RSD/%	n.q.	78%	59%	n.q.	53%	2%	53%	15%	15%	35%	28%	47%	26%	n.q.	107%	n.q.	n.q.
	n	n.q.	14	2	n.q.	14	14	14	14	14	14	1	14	4	n.q.	3	n.q.	n.q.
283	$\bar{x}$	0.966	0.297	0.279	0.026	0.314	96.179	0.312	0.259	0.523	0.004	0.005	0.810	0.026	0.011	n.q	n.q.	n.q.
	s	1.695	0.475	0.380	0.037	0.695	3.405	0.138	0.056	0.088	0.002	0.004	0.530	0.016	0.000	n.q	n.q.	n.q.
	$s(\bar{x}_i)$	0.489	0.137	0.110	0.011	0.201	0.983	0.040	0.016	0.025	0.001	0.001	0.153	0.005	0.000	n.q	n.q.	n.q.
	RSD/%	175%	160%	136%	142%	221%	4%	44%	22%	17%	58%	65%	66%	61%	0%	n.q	n.q.	n.q.
	n	12	12	12	12	12	12	12	12	12	12	12	12	12	2	n.q	n.q.	n.q.
500	$\bar{x}$	0.262	0.174	1.260	n.q.	0.087	95.708	0.446	0.242	0.762	0.001	0.004	0.898	0.045	n.q.	0.112	n.q.	n.q.
	s	0.724	0.291	5.901	n.q.	0.243	6.262	0.171	0.048	0.129	0.001	0.003	0.677	0.034	n.q.	0.199	n.q.	n.q.
	$s(\bar{x}_i)$	0.115	0.046	0.933	n.q.	0.038	0.990	0.027	0.008	0.020	0.000	0.000	0.107	0.005	n.q.	0.032	n.q.	n.q.
	RSD/%	277%	168%	468%	n.q.	278%	7%	38%	20%	17%	89%	66%	75%	74%	n.q.	179%	n.q.	n.q.
	n	40	40	40	n.q.	40	40	40	40	40	40	40	40	40	n.q.	40	n.q.	n.q.

A.III.2 X-ray Diffraction

Figures A.III.7 to **A.III.11** present the X-ray diffraction patterns for the analyzed coins being exposed on **Tables A.III.8** to **A.15** the detailed peak attribution.

Table A.III.8 – Powder XRD patterns peak attribution for 275 coin obverse (O).

275 O				
2θ/º	d_{hkl}/Å	I_r/%	Id.	*hkl*
17.499	5.068	7.76	M	120
24.129	3.689	8.80	M	220
26.520	3.361	36.54	Q	101
27.692	3.221	7.34	SC	111
29.376	3.041	6.44	CP	110
31.411	2.848	14.34	M	$\bar{2}$01,140
32.068	2.791	21.22	SC/M	200/320,$\bar{2}$11
36.237	2.477	100.00	CP	111
37.976	2.369	38.57	Ag	111
39.552	2.279	12.19	Q	102
42.207	2.141	45.61	CP	200
43.104	2.099	12.43	Cu	111
44.181	2.050	13.58	Ag	200
46.156	1.967	7.64	SC	220
50.140	1.819	11.47	Cu	200
57.558	1.601	0.83	SC	222
61.218	1.514	89.75	CP	220
64.338	1.447	17.93	Ag	220

Table A.III.9 – Powder XRD patterns peak attribution for 275 coin the visibly corroded area ("cauliflower"-R2).

275 R2 visible corroded area				
2θ/º	d_{hkl}/Å	I_r/%	Id.	*hkl*
20.910	4.248	6.32	Q	100
26.697	3.339	14.23	Q	101
27.886	3.199	4.59	SC	111
29.549	3.023	4.14	CP	110
30.547	2.927	3.87	n.i.	n.i.
32.832	2.728	3.74	SC	200
36.435	2.466	100.00	CP	111
38.141	2.360	23.30	Ag	111
39.545	2.277	23.33	Q	102
42.302	2.137	31.24	CP	200
44.344	2.043	7.82	Ag	200
46.023	1.972	1.77	SC	220
52.480	1.744	2.04	CP	211
61.346	1.510	34.48	CP	220
64.470	1.444	7.21	Ag	220

Table A.III.10 – Powder XRD patterns peak attribution for 275 coin reverse (R1).

275 R1				
2θ/º	d_{hkl}/Å	I_r/%	Id.	*hkl*
26.170	3.405	16.60	Q	101
27.297	3.267	2.86	SC	111
29.088	3.070	4.72	CP	110
31.754	2.818	9.01	SC	200
35.063	2.559	8.70	T	$\bar{1}$11
35.985	2.496	96.59	CP	200
37.660	2.389	100.00	Ag	111
41.893	2.156	38.03	CP	200
43.852	2.065	42.56	Ag	200
45.767	1.983	5.32	SC	220
49.896	1.828	5.48	Q/Cu	112/200
60.960	1.520	63.59	CP	220
64.024	1.453	37.40	Ag	220

Legend: CP – cuprite (Cu_2O); T – tenorite (CuO); M – malachite ($Cu_2CO_3(OH)_2$); SC – chlorargyrite (AgCl); Q – quartz (SiO_2); n.i. – non-identied.

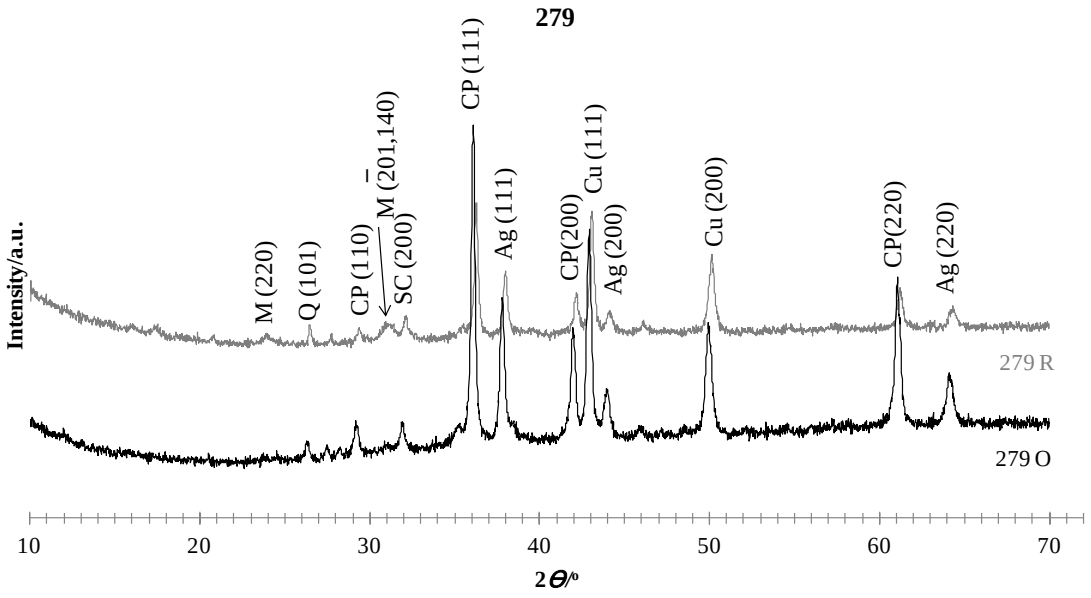

Figure A.III.7 – Stacked XRD patterns obtained for 279 coin on both obverse (279 O) and reverse (279 R) faces.

Table A.III.11 - Powder XRD patterns peak attribution for 279 coin on both obverse (O) and reverse (R) faces.

279 O				
2θ/º	d_{hkl}/Å	I_r/%	Id.	*hkl*
26.251	3.395	5.60	Q	101
27.486	3.245	3.37	SC	111
28.274	3.156	2.42	N	111
29.163	3.062	9.28	CP	110
31.912	2.804	8.21	SC	200
35.228	2.548	6.07	T	$\bar{1}11$
36.112	2.487	100.00	CP	111
37.801	2.380	45.86	Ag	111
41.940	2.154	32.52	CP	200
42.859	2.110	63.70	Cu	111
43.946	2.060	15.81	Ag	200
45.926	1.976	2.55	SC	220
49.912	1.827	33.48	Cu	200
61.064	1.518	47.64	CP	220
64.102	1.452	15.18	Ag	220

279 R				
2θ/º	d_{hkl}/Å	I_r/%	Id.	*hkl*
17.387	5.100	4.43	M	120
20.789	4.273	3.70	Q	100
23.923	3.720	5.92	M	220
26.474	3.367	13.89	Q	101
27.665	3.225	3.15	SC	111
29.385	3.040	10.44	CP	110
31.078	2.878	12.45	M	$\bar{2}01$, 140
32.140	2.785	17.82	SC/M	200/320,$\bar{2}11$
35.468	2.531	9.15	T	$\bar{1}11$
36.258	2.478	100.00	CP	111
37.996	2.368	49.00	Ag	111
42.171	2.143	31.68	CP	200
43.046	2.101	86.37	Cu	111
44.109	2.053	16.50	Ag	200
46.104	1.969	8.63	SC	220
50.131	1.820	53.81	Cu	200
52.255	1.751	1.56	CP	211
57.448	1.604	1.78	SC	222
61.191	1.515	28.32	CP	220
64.273	1.448	13.17	Ag	220

Legend: CP – cuprite (Cu_2O); T – tenorite (CuO); M – malachite ($Cu_2CO_3(OH)_2$); N – nantokite (CuCl); SC – chlorargyrite (AgCl); Q – quartz (SiO_2).

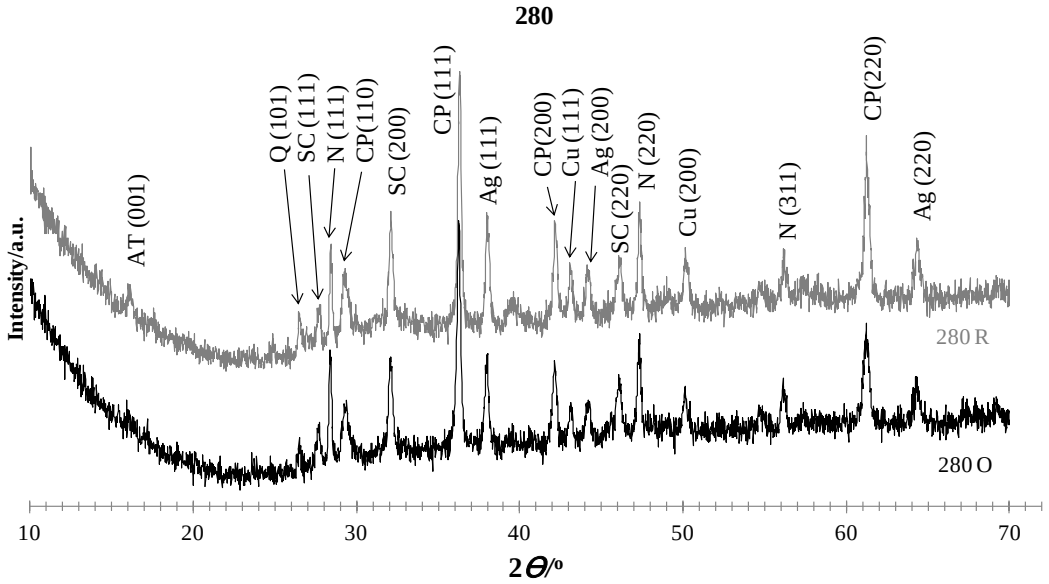

Figure A.III.8 – Stacked XRD patterns obtained for 280 coin on both obverse (280 O) and reverse (280 R) faces.

Table A.III.12 - Powder XRD patterns peak attribution for 280 coin on both obverse (O) and reverse (R) faces.

280 O				
2θ/º	d_{hkl}/Å	I_r/%	Id.	*hkl*
26.501	3.363	14.04	Q	101
27.671	3.224	19.33	SC	111
28.355	3.148	53.15	N	111
29.315	3.047	26.65	CP	110
32.058	2.792	43.99	SC	200
36.298	2.475	100.00	CP	111
38.017	2.367	42.16	Ag	111
42.143	2.144	35.71	CP	200
43.096	2.099	16.01	Cu	111
44.261	2.046	16.29	Ag	200
46.066	1.970	27.21	SC	220
47.294	1.922	40.75	N	220
50.132	1.820	19.40	Cu	200
54.786	1.676	7.67	SC	311
56.128	1.639	17.96	N	311
61.187	1.515	39.00	CP	220
64.352	1.448	17.88	Ag	220
67.577	1.385	3.04	Q/N	301/400

280 R				
2θ/º	d_{hkl}/Å	I_r/%	Id.	*hkl*
16.112	5.501	9.36	AT	001
26.481	3.366	17.10	Q	101
27.705	3.220	16.10	SC	111
28.396	3.143	39.49	N	111
29.280	3.050	28.60	CP	110
32.081	2.790	48.25	SC/AT	200/201
36.322	2.473	100.00	CP	111
37.977	2.369	45.94	Ag	111
39.482	2.282	8.40	AT	040
42.175	2.143	40.11	CP	200
43.095	2.099	21.38	Cu	111
44.185	2.050	19.00	Ag	200
46.176	1.966	22.88	SC	220
47.363	1.919	39.62	N	220
50.094	1.821	19.49	Cu	200
54.797	1.675	6.50	SC	311
56.179	1.637	16.40	N	311
57.535	1.602	5.97	SC	222
61.230	1.514	60.50	CP	220
64.359	1.446	22.76	Ag	220

Legend: CP – cuprite (Cu_2O); N – nantokite (CuCl);

AT – atacamite ($Cu_2Cl(OH)_3$); SC – chlorargyrite (AgCl); Q – quartz (SiO_2).

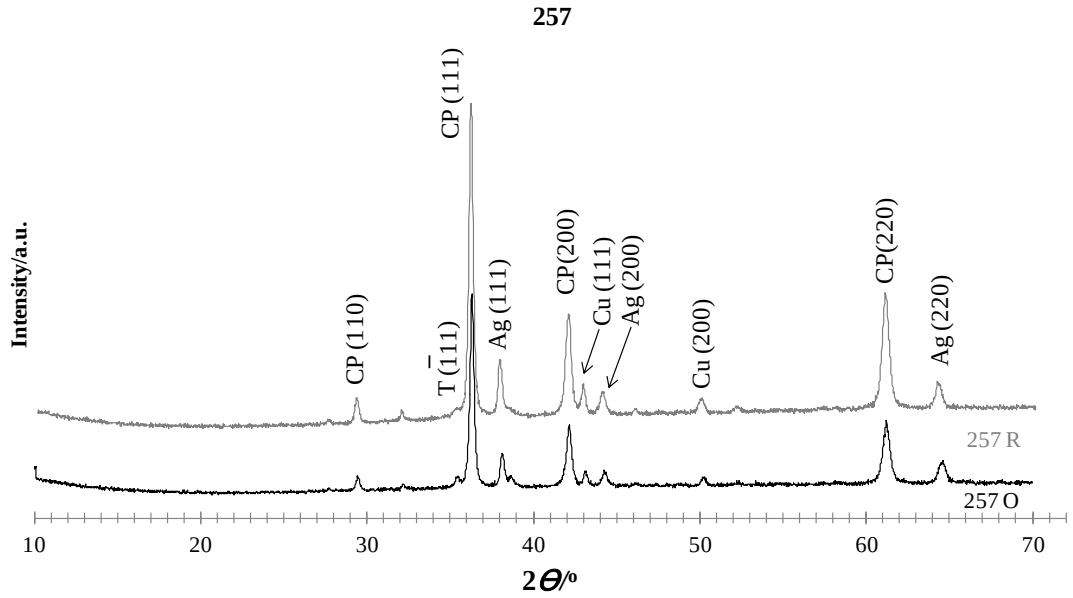

Figure A.III.9 – Stacked XRD patterns obtained for 257 coin on both obverse (257 O) and reverse (257 R) faces.

Table A.III.13 - Powder XRD patterns peak attribution for 257 coin on both obverse (O) and reverse (R) faces.

257 O					257 R				
2θ/º	d_{hkl}/Å	I_r/%	Id.	*hkl*	2θ/º	d_{hkl}/Å	I_r/%	Id.	*hkl*
27.728	3.217	1.40	SC	111	27.510	3.242	1.36	SC	111
29.431	3.035	7.59	CP	110	29.171	3.061	8.51	CP	110
32.209	2.779	3.37	SC/T	200/110	31.865	2.806	4.07	SC	200
35.480	2.530	6.49	T	$\bar{1}11$	35.165	2.552	3.77	T	$\bar{1}11$
36.312	2.474	100.00	CP	111	36.019	2.494	100.00	CP	111
38.074	2.362	16.73	Ag	111	37.728	2.382	16.50	T	111
38.694	2.327	5.80	T	111	37.835	2.378	18.59	Ag	111
42.183	2.142	31.98	CP	200	41.909	2.154	33.59	CP	200
43.108	2.098	8.17	Cu	111	42.814	2.110	10.97	Cu	111
44.252	2.047	8.17	Ag	200	43.988	2.057	7.74	Ag	200
46.242	1.963	1.37	SC	220	45.950	1.973	2.12	SC	220
50.233	1.816	4.36	Cu	200	49.958	1.824	4.64	Cu	200
52.284	1.750	0.83	CP	211	52.046	1.756	1.64	CP	211
61.234	1.512	31.73	CP	220	60.929	1.519	37.38	CP	220
64.454	1.446	9.72	Ag	220	64.096	1.452	8.19	Ag	220

Legend: CP – cuprite (Cu_2O); T – tenorite (CuO); SC – chlorargyrite (AgCl).

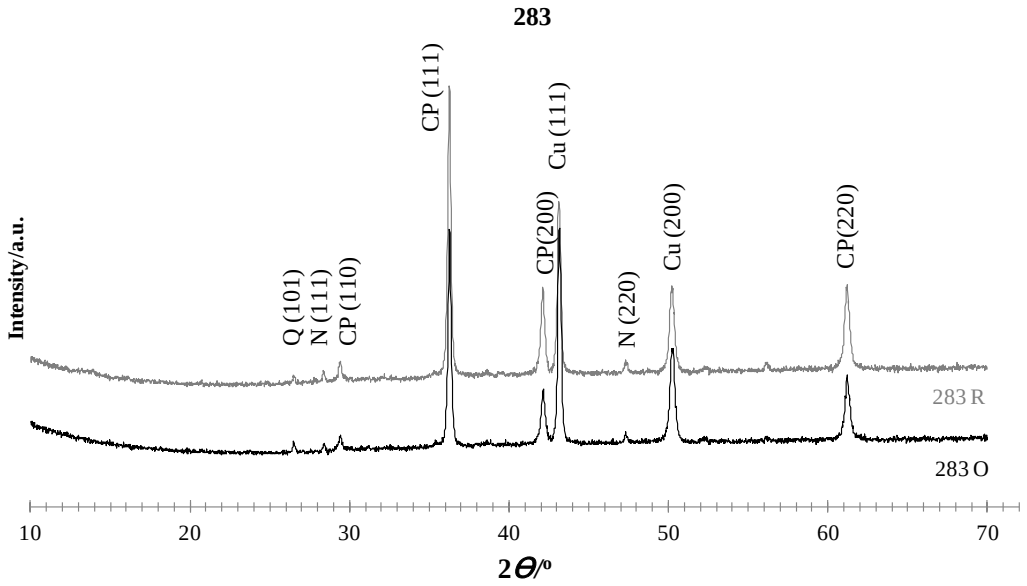

Figure A.III.10 – Stacked XRD patterns obtained for 283 coin on both obverse (283 O) and reverse (283 R) faces.

Table A.III.14 - Powder XRD patterns peak attribution for 283 coin on both obverse (O) and reverse (R) faces.

283 O				
2θ/º	d_{hkl}/Å	I_r/%	Id.	*hkl*
26.515	3.362	4.33	Q	101
28.409	3.142	3.15	N	111
29.430	3.035	6.79	CP	110
31.203	2.867	2.09	Pb	111
35.385	2.537	3.07	T	$\bar{1}11$
36.257	2.476	100.00	CP/Pb	111/200
38.667	2.327	2.38	T	111
42.142	2.143	26.28	CP	200
43.141	2.095	98.75	Cu	111
47.306	1.920	4.98	N	220
50.199	1.816	43.21	Cu	200
52.203	1.751	1.55	Pb	220
56.256	1.634	1.18	N	311
61.211	1.513	29.36	CP	220

283 R				
2θ/º	d_{hkl}/Å	I_r/%	Id.	*hkl*
26.532	3.360	2.19	Q	101
28.431	3.139	3.29	N	111
29.351	3.043	5.25	CP	110
36.254	2.478	100.00	CP	111
38.668	2.329	1.44	T	111
42.117	2.146	29.09	CP	200
43.071	2.100	51.09	Cu	111
47.288	1.922	3.92	N	220
50.186	1.818	28.58	Cu	200
52.334	1.748	1.39	CP	211
56.142	1.638	2.43	N	311
61.203	1.513	28.98	CP	220

Legend: CP – cuprite (Cu_2O); T – tenorite (CuO); N – nantokite (CuCl);

Q – quartz (SiO_2); n.i. – non-identified.

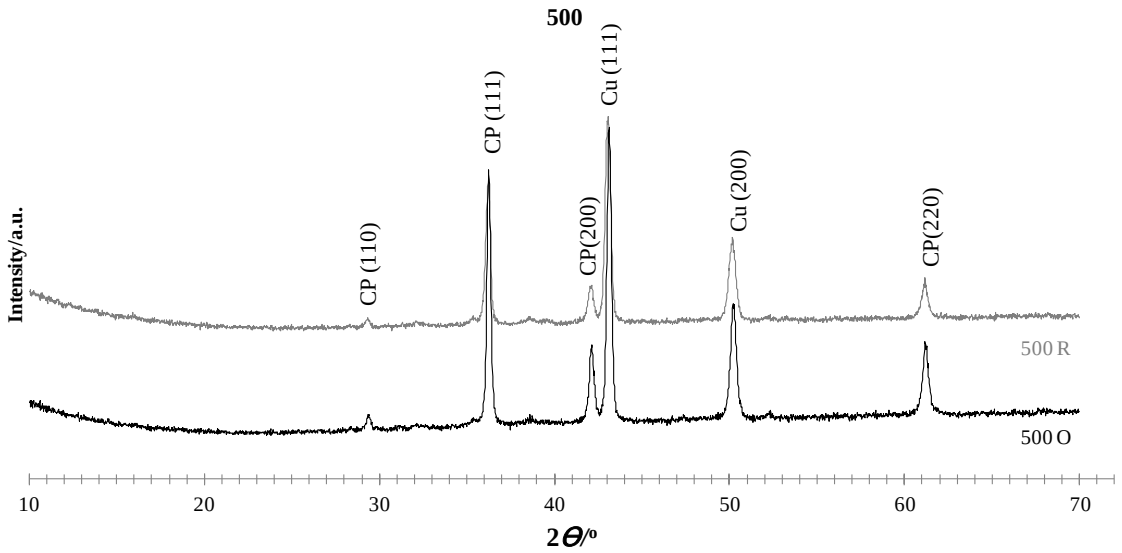

Figure A.III.11 – Stacked XRD patterns obtained for 500 coin on both obverse (500 O) and reverse (500 R) faces.

Table A.III.15 - Powder XRD patterns peak attribution for 500 coin on both obverse (O) and reverse (R) faces.

500 O				
2θ/º	d_{hkl}/Å	I_r/%	Id.	*hkl*
29.385	3.040	5.32	CP/C	110/104
32.067	2.791	1.10	T	110
35.370	2.538	2.40	T	$\bar{1}11$
36.219	2.480	88.28	CP	111
38.527	2.337	1.59	T	111
42.055	2.149	23.43	CP	200
43.091	2.099	100.00	Cu	111
50.281	1.815	40.04	Cu	200
52.246	1.751	1.63	CP	211
61.165	1.514	25.29	CP	220

500 R				
2θ/º	d_{hkl}/Å	I_r/%	Id.	*hkl*
29.326	3.046	4.92	CP/C	110/104
32.107	2.788	2.89	T	110
35.342	2.540	3.84	T	$\bar{1}11$
36.242	2.479	81.99	CP	111
38.607	2.332	2.91	T	111
39.621	2.275	1.51	C	113
42.144	2.144	19.45	CP	200
42.944	2.104	91.08	Cu	111
43.154	2.100	100.00	Cu/C	111/202
50.166	1.817	45.57	Cu	200
52.245	1.750	1.46	CP	211
61.175	1.514	19.83	CP	220

Legend: CP – cuprite (Cu_2O); T – tenorite (CuO); C – calcite ($CaCO_3$).

A.III.3 Scanning Electron Microscopy / Energy Dispersive X-ray Spectroscopy

The following figures (**A.III.12** to **A.III.24**) present the spot quantification by means of SEM/EDS for each identified morphology.

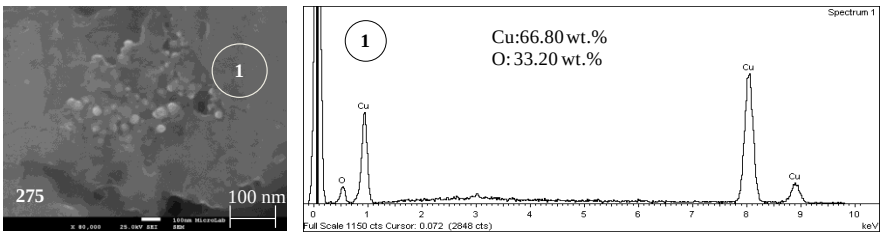

Figure A.III.12 – SEM/EDS copper phase obtained on 275 coin.

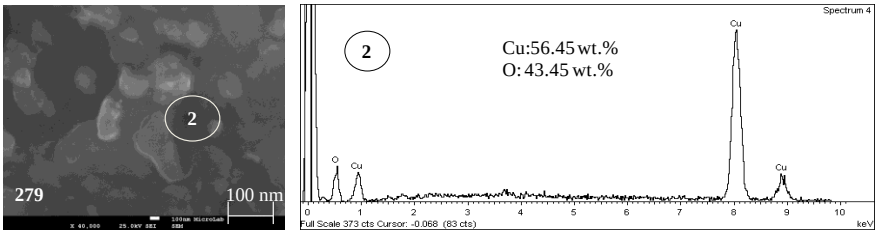

Figure A.III.13– SEM/EDS copper phase obtained on 279 coin.

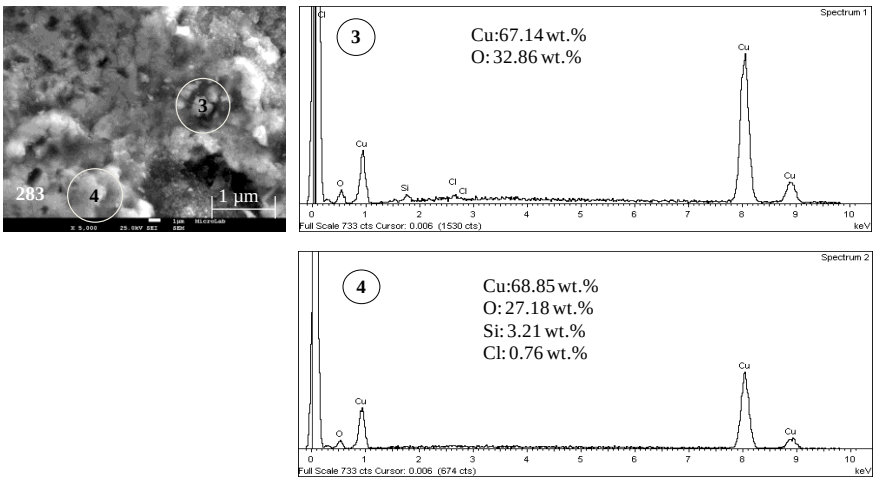

Figure A.III.14 – SEM/EDS copper phase obtained on 283 coin.

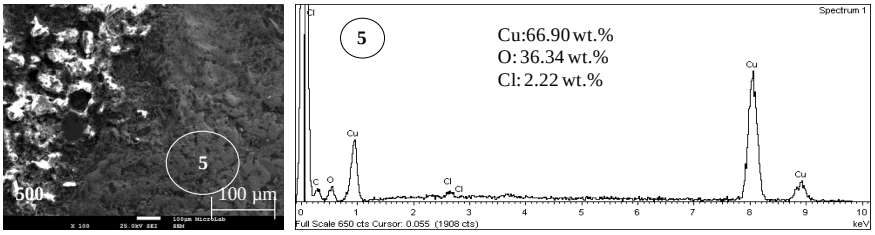

Figure A.III.15 – SEM/EDS copper phase obtained on 500 coin.

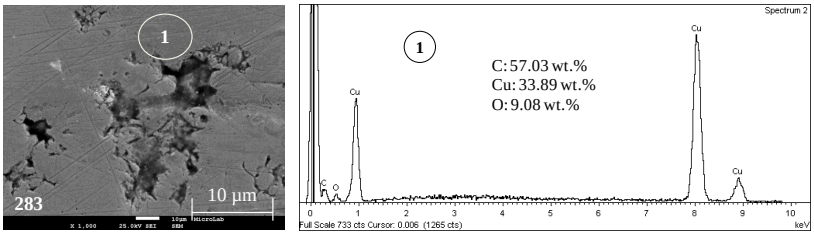

Figure A.III.16 – SEM/EDS copper phase obtained on 283 coin.

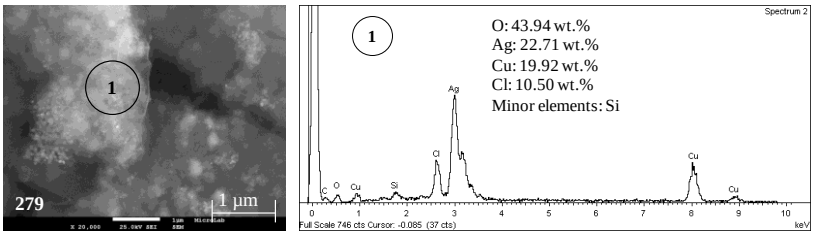

Figure A.III.17 – SEM/EDS silver phase obtained on 279 coin.

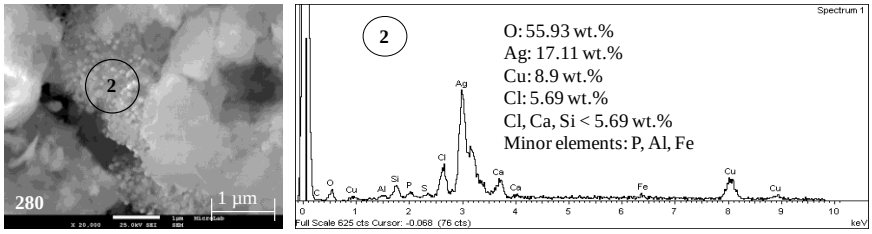

Figure A.III.18 – SEM/EDS silver phase obtained on 280 coin.

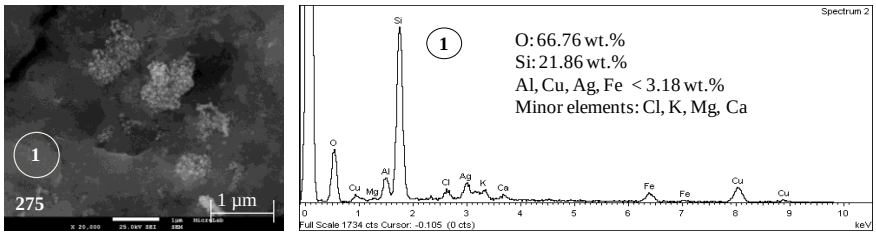

Figure A.III.19 – SEM/EDS silicon phase obtained on 275 coin.

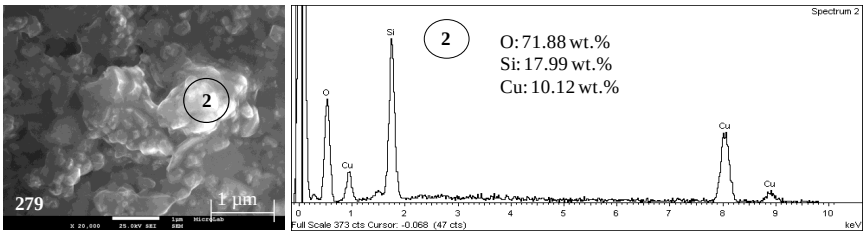

Figure A.III.20 – SEM/EDS silicon phase obtained on 279 coin.

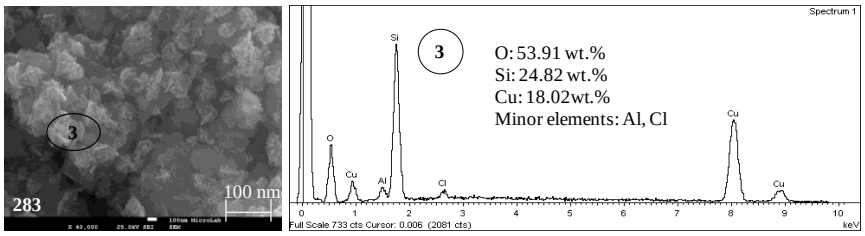

Figure A.III.21 – SEM/EDS silicon phase obtained on 283 coin.

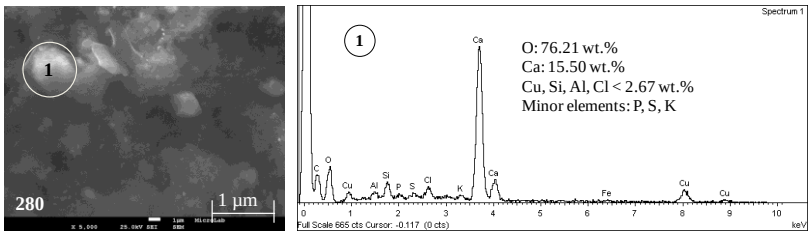

Figure A.III.22 – SEM/EDS calcium phase obtained on 280 coin.

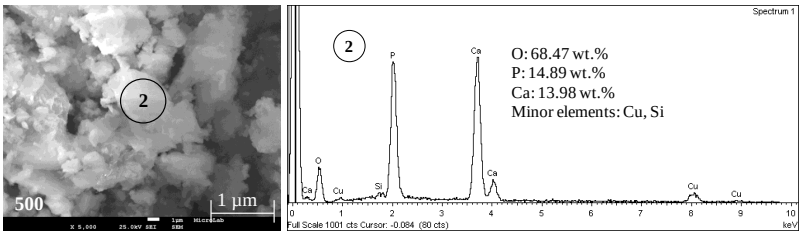

Figure A.III.23 – SEM/EDS calcium phase obtained on 500 coin.

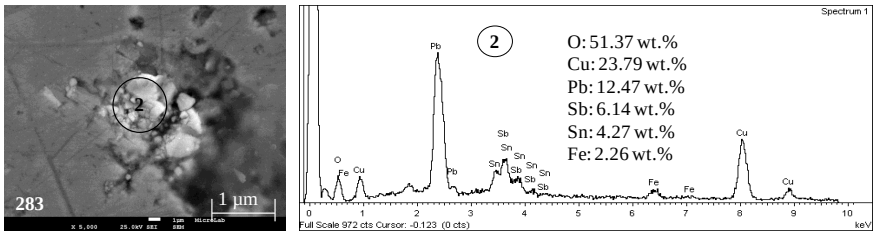

Figure A.III.24 – SEM/EDS lead phase obtained on 283 coin.

Figures A.III.25 to **A.III.27** present the spot quantification by means of SEM/EDS for the coins scraped, or not, edges.

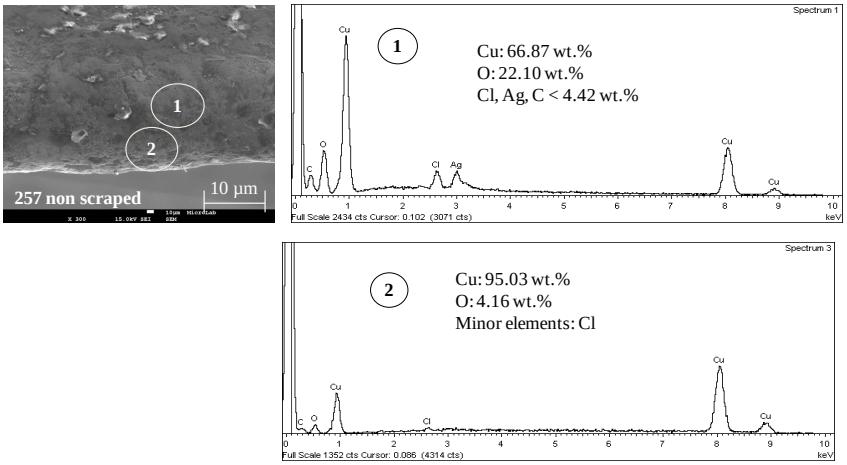

Figure A.III.25 – SEM/EDS of non-scraped edge obtained for 257 coin.

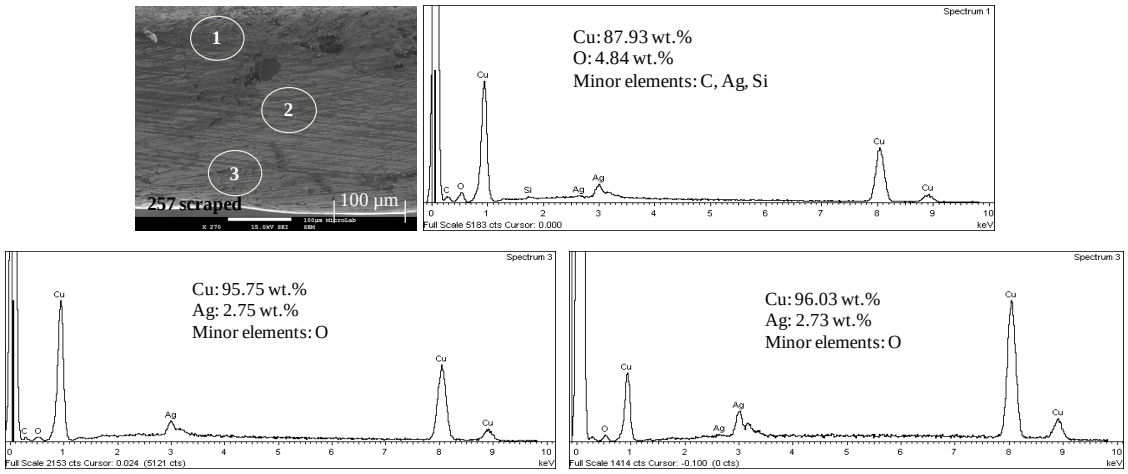

Figure A.III.26 – SEM/EDS of manual scraped edge obtained for 257 coin.

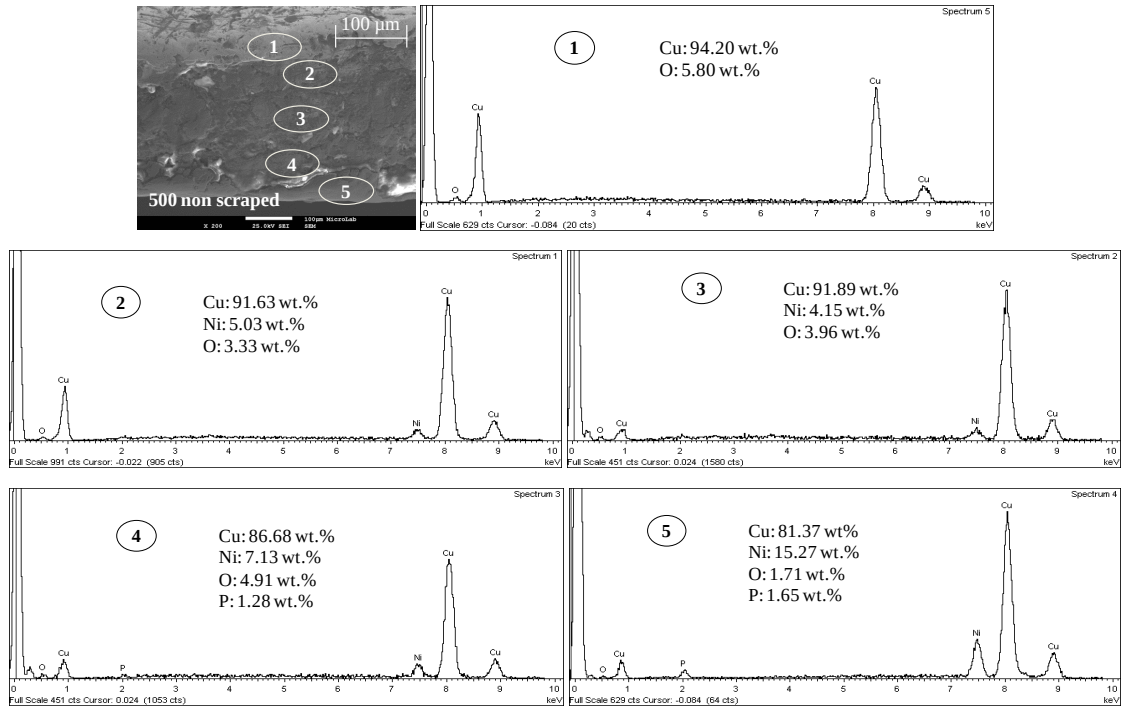

Figure A.III.27 – SEM/EDS of non-scraped edge obtained for 500 coin.

Annexe IV

EXPERIMENTAL PART

DEVELOPMENT OF NANOMATERIALS FOR CULTURAL HERITAGE CONSERVATION

The criterion used for the suspensions choice was the contact angle´ tests (**Figure A.IV.1**) made by Chen *et al.* [68].

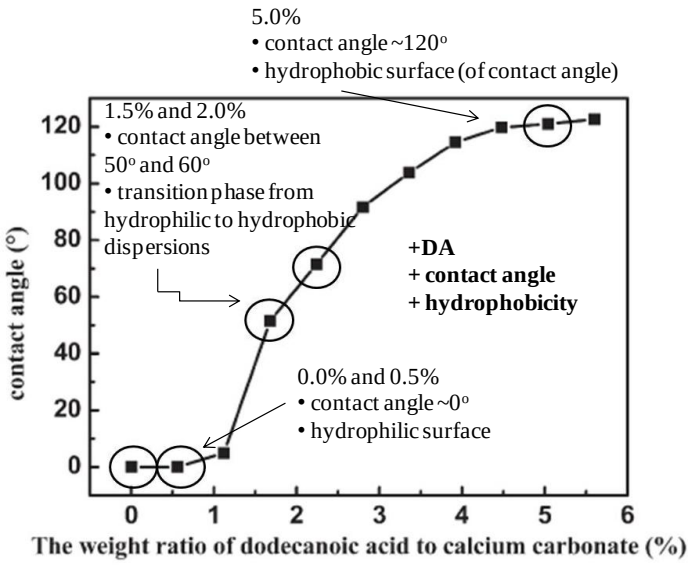

Figure A.IV.1 – Effects of the weight ratio of DA on the $CaCO_3$ particles´ contact angle, obtained at 20° C with a $Ca(OH)_2$ concentration of 5 wt.% [68].

DA is used as a surface modifier and it changes the $CaCO_3$ nanoparticles from hydrophilic to hydrophobic. Thus the image makes clear the choice of 0.0%, 0.5%, 1.5%, 2.0% and 5.0% (w/w) functionalizations in order to evaluate the effect of this acid on the powders as well as in dispersions.

A.IV.1 Nanoparticles syntheses

Table A.IV.1 presents the mass of CaO (g) for each synthesis and the ethanol:DA volume (dm^3) added to each one of them.

Table A.IV.1 – CaO mass (g) and ethanol:DA volume (dm^3) measured for each reaction.

% w/w	m(CaO)/g	V(ethanol:DA)/dm^3
0.0	2.378	0.00
0.5	2.332	2.00
1.5	2.363	6.40
2.0	2.347	8.35
5.0	2.360	21.00

A.IV.2 Nanoparticles dispersions

In order to analyze the nanoparticles´ stability in cyclohexane several dispersions were made. The $CaCO_3$ and $Ca(OH)_2$ masses used can be seen on **Table A.IV.2**.

Table A.IV.2 – Masses of $CaCO_3$ and $Ca(OH)_2$ used in the cyclohexane dispersions.

% (w/w)	m($CaCO_3$)/g	m($Ca(OH)_2$)/g
0.0	0.0272	0.0201
0.5	0.0273	0.0208
1.5	0.0272	0.0203
2.0	0.0270	0.0200
5.0	0.0272	0.0200

Table A.IV.3 indicates the 5.0% DA $CaCO_3$ and $Ca(OH)_2$ amounts used to prepare remaining dispersions.

Table A.IV.3 – Masses of 5.0% DA $CaCO_3$ and $Ca(OH)_2$ used in nonane, nonane+1-butanol and cyclohexane+1-butanol dispersions.

Nonane		
	m/g	Ultrasound cycles (10 minutes each)
$CaCO_3$	0.046	9 cycles
$Ca(OH)_2$	0.034	3 cycles
Nonane + 1-butanol		
	m/g	Ultrasound cycles (10 minutes each)
$CaCO_3$	0.046	9 cycles
$Ca(OH)_2$	0.035	3 cycles
Cyclohexane + 1-butanol		
	m/g	Ultrasound cycles (10 minutes each)
$CaCO_3$	0.046	9 cycles
$Ca(OH)_2$	-	-

Annexe V

DETAILED RESULTS PRESENTATION

DEVELOPMENT OF NANOMATERIALS FOR CULTURAL HERITAGE CONSERVATION

A.V.1 Turbidimetry

Figures A.V.1 to **A.V.5** represent the turbidimetry results for the $CaCO_3$ with 0.0, 0.5, 1.5, 2.0 and 5.0% DA nanoparticles´ functionalization dispersions in cyclohexane, respectively.

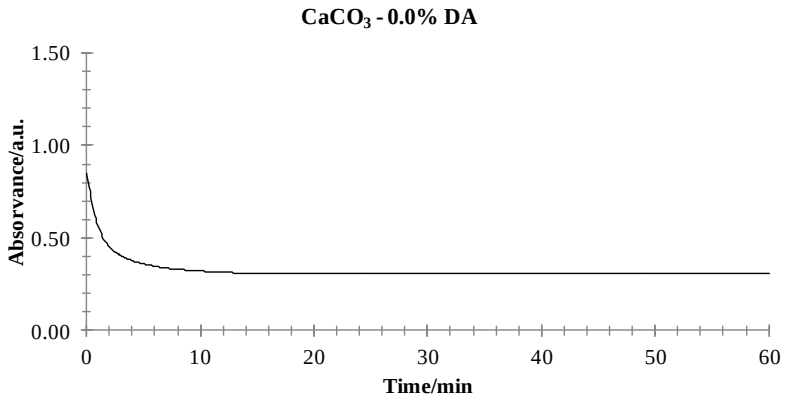

Figure A.V.1 – Turbidimetry results for the $CaCO_3$ with 0.0% DA dispersion in cyclohexane.

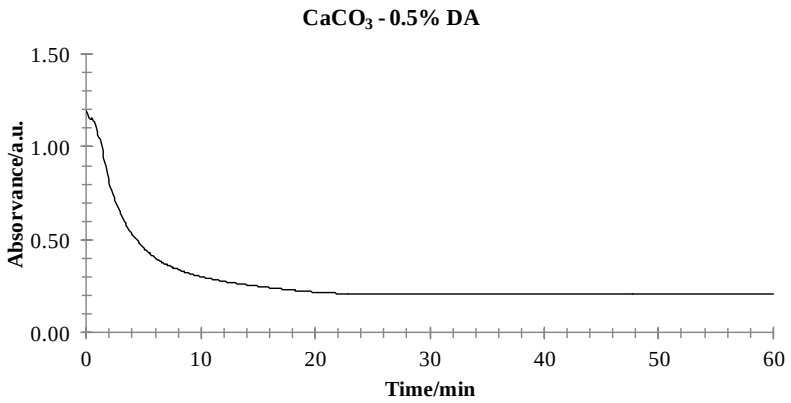

Figure A.V.2 – Turbidimetry results for the $CaCO_3$ with 0.5% DA dispersion in cyclohexane.

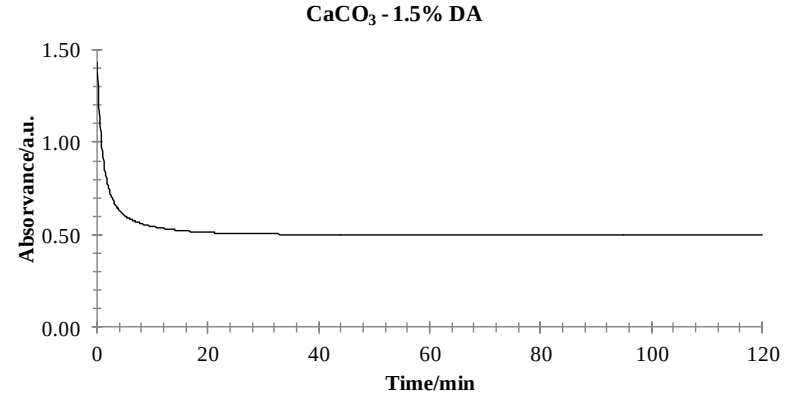

Figure A.V.3 – Turbidimetry results for the $CaCO_3$ with 1.5% DA dispersion in cyclohexane.

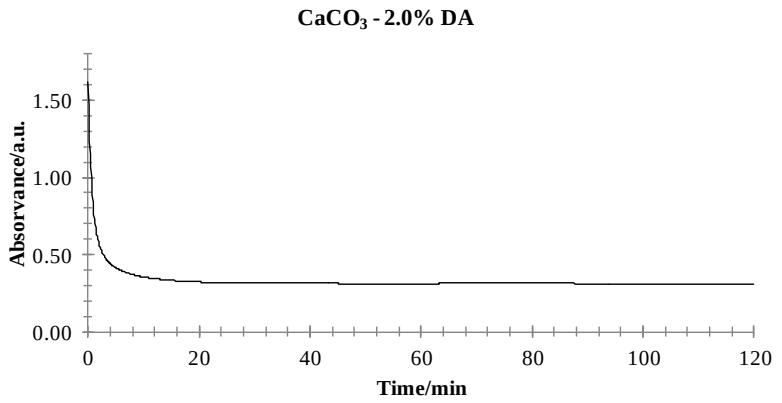

Figure A.V.4 – Turbidimetry results for the $CaCO_3$ with 2.0% DA dispersion in cyclohexane.

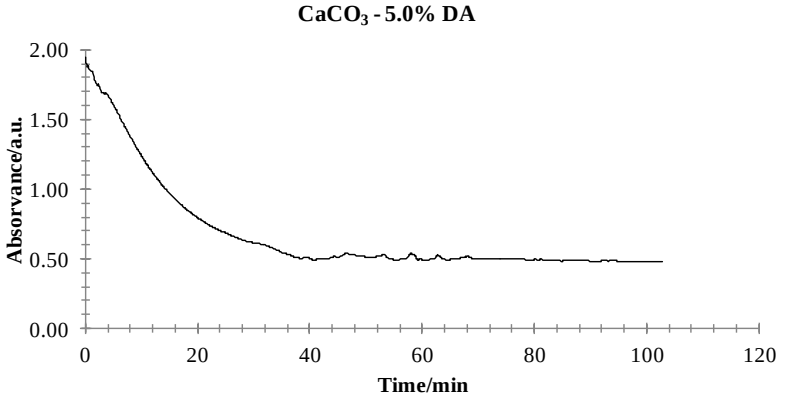

Figure A.V.5 – Turbidimetry results for the $CaCO_3$ with 5.0% DA dispersion in cyclohexane.

Figures A.V.6 to **A.V.10** represent the turbidimetry results for the $Ca(OH)_2$ with 0.0, 0.5, 1.5, 2.0 and 5.0% DA nanoparticles´ functionalization dispersions in cyclohexane, respectively.

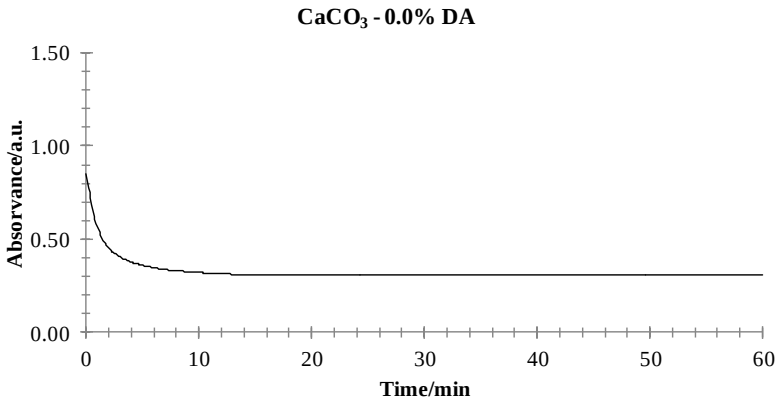

Figure A.V.6 – Turbidimetry results for the $Ca(OH)_2$ with 0.0% DA dispersion in cyclohexane.

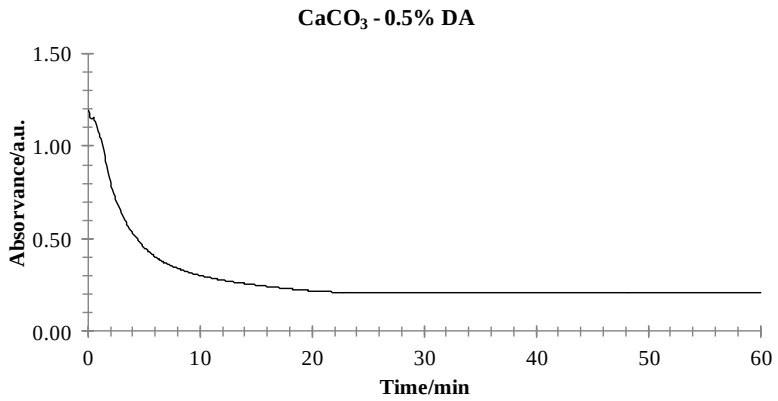

Figure A.V.7 – Turbidimetry results for the $Ca(OH)_2$ with 0.5% DA dispersion in cyclohexane.

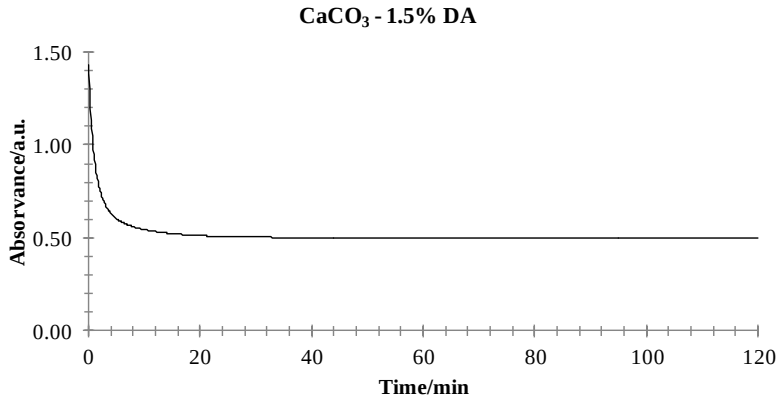

Figure A.V.8 – Turbidimetry results for the $Ca(OH)_2$ with 1.5% DA dispersion in cyclohexane.

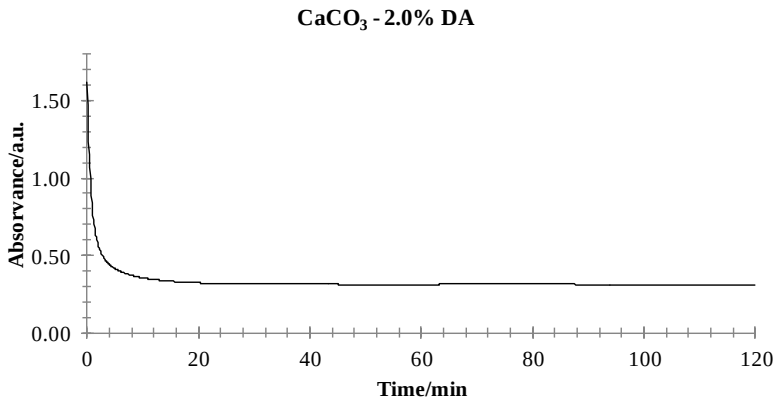

Figure A.V.9 – Turbidimetry results for the $Ca(OH)_2$ with 2.0% DA dispersion in cyclohexane.

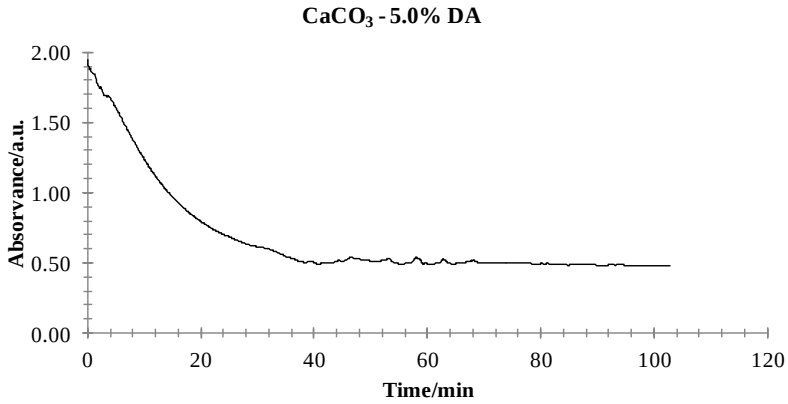

Figure A.V.10 – Turbidimetry results for the $Ca(OH)_2$ with 5.0% DA dispersion in cyclohexane.

A.V.2 X-ray Diffraction

The detailed and individual X-ray diffraction patterns peak attribution is presented on **Tables A.V.1** and **A.V.2** for the calcium carbonate powders functionalized with 0.0% and 5.0% of dodecanoic acid, respectively.

Table A.V.1 – Powder XRD patterns peak attribution for $CaCO_3$ 0.0% DA powder.

$CaCO_3$ 0.0% DA		
$2\theta/^o$	**d_{hkl}/Å**	**Id.**
23.040	3.857	C
26.483	3.363	A
29.402	3.035	C
31.465	2.841	A
35.935	2.497	C
39.379	2.286	C
43.118	2.096	C
47.138	1.926	C
47.531	1.911	C
48.493	1.876	C
56.503	1.627	C
57.321	1.606	A
60.610	1.527	C
61.319	1.511	C
62.957	1.475	C
62.993	1.474	C
64.565	1.442	C
65.661	1.421	C

Table A.V.2 – Powder XRD patterns peak attribution for $CaCO_3$ 5.0% DA powder.

$CaCO_3$ 5.0% DA		
$2\theta/^o$	**d_{hkl}/Å**	**Id.**
7.423	11.892	CL
9.962	8.872	CL
12.501	7.075	n.i.
21.342	4.160	V
22.920	3.887	C
24.789	3.589	V
26.379	3.376	A
26.961	3.304	V
29.290	3.047	C
31.364	2.850	A
32.685	2.738	V
35.811	2.505	C
39.257	2.293	C
42.994	2.102	V
43.648	2.072	C
47.003	1.932	C
47.425	1.915	C
48.381	1.880	C
49.095	1.824	V
56.375	1.631	V
57.198	1.609	A
60.516	1.529	C
62.828	1.478	C
62.871	1.477	C
64.390	1.446	C
64.347	1.447	C
64.570	1.442	C
65.575	1.422	C

Legend: C - calcite; A - aragonite; V - vaterite; CL - calcium laurate; n.i. – non-identified.